Powder Metallurgical Processing of Titanium Alloys and Aluminides

by

Hung-Wei Liu

Submitted in partial fulfilment of the requirements
for the degree of Doctor of Philosophy

at

Dalhousie University
Halifax, Nova Scotia
August 2016

Table of Contents

List of Tables

List of Figures

Abstract

In this thesis, the economical powder metallurgical approach was investigated to produce two Ti binary alloys (i.e. Ti-Ni and Ti-Sn) and a Ti-48Al based intermetallic alloy. In the first part of the work, Ni and Sn (up to 10 wt-%) were alloyed to Ti to facilitate the diffusion process via liquid phase sintering mechanisms. For Ti-Ni alloys, the persistent liquid clearly improved densification, and density close to 99% was achieved. Conversely, for the Ti-Sn alloys, the transient liquid was not as effective, despite some density gain. Transitions in the size and the size distribution of pores in the Ti binary alloys were also studied and the Ostwald ripening phenomenon was revealed.

In the case of manufacturing Ti-48Al, the press-and-sinter PM approach was initially investigated. The Ti-Al elemental compact experienced significant volume expansion after being sintered, and the sintered product was a porous structure. To control the volume expansion due to $TiAl_3$ formation, the effects of sintering temperature, low temperature annealing and powder size were examined. A pre-alloyed Ti-48Al powder was further produced to avoid the swelling problem. Combined with higher sintering temperature (1350°C) or longer duration of isothermal hold (4h), density close to 90% was achieved.

The novel spark plasma sintering process was also applied to produce TiAl alloys. This process demonstrated great efficiency, and close to fully dense material was produced with merely 3 minutes of isothermal hold time. The influences of sintering temperature, hold time and particle size were all examined. A reaction model was proposed to explain the layered structure of the 'in-house' produced powder, and its formation sequences of the targeted phases Ti_3Al, TiAl, and the intermediate phases $TiAl_2$ and $TiAl_3$. Fine and coarse lamellar structures developed within or around the Ti_3Al grains were observed. With increased sintering temperature, the Ti:Al ratio gradually approached 60:40 in the lamellar regions, suggesting a 3TiAl:1Ti_3Al phase combination. Ostwald ripening and migration of the porosity were also observed. The TiAl alloy was further reinforced with B_4C particulates. Promising preliminary results in terms of sintered density and hardness are reported and the compositions in the phases were analysed.

List of Abbreviations and Symbols Used

ASTM	American Society for Testing and Materials
AT	Attrition
BCC	Body-centred cubic
BDTT	Brittle-to-ductile transition temperature
CIP	Cold isostatic press
CLV	Counter-gravity low-pressure casting of vacuum-melted alloys process
CP	Commercially pure
DIC	Differential interference contrast imaging
DSC	Differential scanning calorimetry
E	Elastic modulus
EDS	Energy-dispersive X-ray spectroscopy
EPMA	Electron probe micro-analysis system
HCP	Hexagonal closed-packed
HDH	Hydride-dehydride
HG	Hand ground
HIP	Hot isostatic press
HRA	Rockwell hardness A scale
LC	Licowax®

LPS	Liquid phase sintering
MPIF	Metal Powder Industries Federation
PM	Powder metallurgy
SB	Shatterbox
SBL	Shatterbox (large bowl)
SEM	Scanning electron microscopy
TMC	Titanium matrix composite
UTS	Ultimate tensile strength
VAR	Vacuum arc remelt furnace
WDS	Wavelength-dispersive X-ray spectroscopy
XRD	X-ray diffraction
α	Hexagonal closed-packed phase titanium
α_2	Ordered hexagonal phase (Ti_3Al)
β	Body-centred cubic phase titanium
γ	Tetragonal phase (TiAl)

Acknowledgements

I would like to thank my supervisor Dr. Kevin Plucknett for his guidance and support throughout the whole research, and my committee members, Dr. Paul Bishop and Dr. Stephen Corbin, for their insightful comments and suggestions. It has been a great pleasure working with you all. Thanks are also due to Ms. Patricia Scallion for the SEM assistance and Mr. Dean Grijm for support with sample machining. Randy Cook, Greg Sweet, Chenxin Jin and Stephen Buchholz are also appreciated for their help in the lab and friendship for all these days. Also much appreciated is the financial support from the Automotive Partnerships Canada (APC) program, funded by the Natural Science and Engineering Research Council of Canada (NSERC), this work would not be possible without the support.

Lastly, I would like to express my sincerest gratitude to my parents and my brothers for their support all these years. This is a long journey, without their accompanying, I would not have the opportunity to be here typing this page and I cannot image how I could have achieved and completed this thesis.

Chapter 1. Introduction

Titanium alloys have attracted considerable attention due to their very competitive strength-to-weight ratio and corrosion properties, when compared to aluminium alloys or stainless steels. When Ti is heavily alloyed with Al, an even lighter, harder and more corrosion and oxidation resistant material category forms; known as the titanium aluminides or TiAl-based alloys, this material class has shown great potential for high temperature applications. However, the production costs for Ti- or TiAl-based alloys remain high, and as a consequence, those alloys have not yet widely reached the consumer markets. To tackle this problem, much effort has been dedicated to applying cost-effective, near-net-shape fabrication techniques to produce Ti- and TiAl-based alloys. Among many manufacturing processes, powder metallurgy (PM) has shown great advantages over the more conventional casting or thermomechanical processing routes. PM technology not only is a near-net-shape process, but also allows the production of hard-to-melt materials and particulate-reinforced composites. Moreover, the PM process alleviates the segregations issues which are commonly seen in cast products. Nevertheless, residual porosity remains a critical problem, particularly in the economical 'press-and-sinter' PM process.

In the present thesis, two Ti binary alloys (i.e. Ti-Ni and Ti-Sn), and a two-phase titanium aluminide (i.e. Ti-48Al) have been produced and studied. The first part of the thesis focuses on enhancing densification with the economical 'press-and-sinter' PM technique. Mechanisms based on liquid phase sintering of the Ti alloys have been investigated in Chapter 3 (in the form of a journal article, published in *Materials Science and Engineering: A*, September 2015). Ni and Sn are selected as the liquid forming additive materials for Ti sintering. For the Ti and Ni powder blend, the liquid phase is anticipated to form from the eutectic reaction, creating a persistent liquid at the sintering temperature. Conversely, for the Ti and Sn mixture, the liquid phase will be generated when the Sn powder begins to melt, and is likely to rapidly alloy with the Ti. Consequently, a comparison between the persistent and transient liquid phase sintering has been made in terms of the resultant sintered properties.

In the second part of the thesis, titanium aluminide is studied fundamentally, as PM-based studies on this material are still limited, particularly in terms of the microstructural evolution. In Chapter 4 (published in *COM 2015 Conference of Metallurgists*, August 2015), Ti-48Al has been produced using economical elemental Ti and Al powders and the press-and-sinter process. Some fundamental PM processing parameters such as sintering temperature and time, and the particle size are investigated to mitigate any swelling phenomenon. To further avoid the volume expansion completely, a pre-alloyed Ti-48Al powder is synthesised and sintered. A more extensive study on producing the pre-alloyed Ti-48Al powder is given in Chapter 5 (submitted to *Advanced Powder Technology*, June 2016). In this paper, wet and dry grinding methods are evaluated to reduce the particle size. Microstructural and phase evolution of the α_2-Ti_3Al and γ-TiAl are investigated from sintering studies using a coarse powder. A transformation model is proposed in the paper to explain the reactions between elemental Ti and Al powder.

In Chapter 6 (submitted to *Materials Science and Engineering: A*, June 2016), spark plasma sintering (SPS) technology is explored to sinter the 'in-house' produced Ti-48Al powder. The SPS process, which is relatively novel, provides rapid heating and cooling rates and many unique advantages over the traditional (press-and-sinter) sintering practice. Excellent densification results are reported in this paper, and a model on the microstructural evolution and transformation of the (fine and coarse) lamellar structure and grains is proposed. Furthermore, the temporal pore quantity and locations (i.e. highlighting migration) are also analysed.

For the four published and submitted papers (Chapter 3 to 6), the author was involved in planning and conducting all of the experimental works, and prepared the primary drafts of the papers; Dr. Plucknett provided general guidance to the research and edited the papers. In terms of the paper relating to Chapter 6, Dr. Bishop provided advice for the SPS experiments, and help in refining the final version of the paper.

From the literature, many studies have been conducted to produce TiB_x (x=1 or 2) or B_4C reinforced Ti composites with improved hardness, wear and creep resistance. Those properties are important for high temperature applications, which is one targeted use of TiAl-based alloys. Moreover, those composites are very suitable to be produced using the

PM route. Therefore, based on the successful experiences generated in TiAl sintering using the SPS process, B_4C ceramic powder was incorporated into TiAl to form an intermetallic composite, which can further improve the wear and creep properties of the TiAl alloy. Some preliminary results are reported in Chapter 7. Finally, the overall conclusions are outlined in Chapter 8, providing some suggestions and recommendations for future work.

Chapter 2. Background

2.1 Titanium and Its Alloys

2.1.1 Properties and Applications

Titanium and its alloys are lightweight materials (density ~4.5 g/cm^3) with good strength, ranging from ~470MPa up to ~1,800MPa (maintained up to 500°C) [1]. Compared with steel, aluminium or magnesium alloys, Ti alloys exhibit excellent specific yield tensile strengths (Figure 2-1). This excellent strength-to-weight ratio makes Ti alloys very appealing as structural materials, particularly in weight conscious applications (e.g. transportation). Accordingly, more than 50% of titanium material is used as engine or structural components in the aerospace industry. In a modern aircraft, titanium alloys can comprise up to one third of the weight, and it is the second most used metal following nickel alloys [2]. Not only are the titanium alloys lightweight, but they also retain adequate strength at high temperature, up to 500°C. As a consequence, one of the main applications of the Ti alloys is for engine components, such as valves and connecting rods, for example in the Corvette Z06 V8 engine [3].

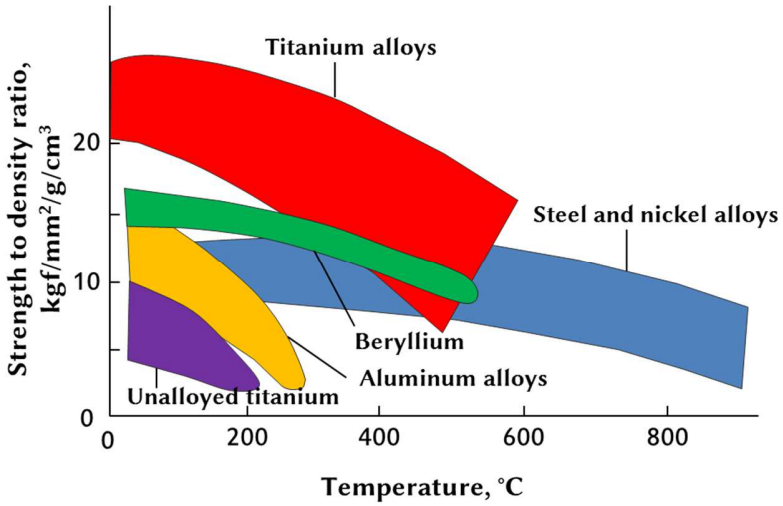

Figure 2-1. Comparison of specific yield strength between Ti alloys with other common materials (figure redrawn from [4]).

Titanium alloys also possess remarkable corrosion resistance. Similar to the protection mechanism for Al alloys, an impermeable TiO_2 film forms immediately on a fresh surface when the material is exposed to an oxygen containing atmosphere. Such Ti oxide film is immune (passive) against acids such as HCl, H_2SO_4 or chlorides. The protective oxide film can regenerate itself with the presence of oxygen or moisture [1].

Pure titanium possesses a hexagonal-close packed (HCP) structure at low temperatures, but undergoes an allotropic phase transformation to a body-centered cubic (BCC) structure at the α/β transus temperature (around 882°C). The phase transformation can be strongly influenced by the alloying additions, which can be categorised as α or β stabilisers or neutral elements, based on their tendency of forming a certain phase when added to Ti. Accordingly, titanium alloys can include α, near α (with a little β), α/β (two-phased) and β phase constituents. Because of the HCP/BCC phase transformation and the ability to manipulate the phase constituents by adding alloying additions, Ti alloys cannot only be strengthened by solid-solution strengthening but also through processing or post-processing heat treatments. As a consequence, various phase configurations are responsible for a wide range of mechanical properties.

2.1.2 Effects of Alloying Elements

As briefly mentioned earlier, the alloying elements influence the Ti phase constituents. Elements can affect the α/β transus temperature and thus promote or retain α or β phase, accordingly. In principle, the effects of alloying on the alloys are listed as follows [5]:

(1) Relax the crystal structure and thus the restriction on slip modes.

(2) Alter the kinetics of ordering or change the long-range order degree.

(3) Change the alloy constitution (i.e. acquiring useful (ductile) phases).

(4) Enable microstructural control (e.g. grain refinement).

Among these effects, (1) and (2) are to change the intrinsic crystal plasticity of the alloy, whereas (3) and (4) are to achieve microstructural alteration, which is generally the predominant effect with respect to improving mechanical properties. The alloying elements can be classified as α or β phase stabilizer or neutral, as discussed earlier, and highlighted in Table 2-1.

Table 2-1. Classification of solutes for titanium alloys [6].

Type	α stabilizer	β stabilizer	Neutral
Element	Al, O, N, C, Ga	Mo, W, V, Ta, Cu, Mn, Cr, Fe, Ni, Co, H	Zr, Sn, Si

These elements exhibit different tendencies towards forming the HCP or BCC structure in titanium and can alter the retained phase. In comparison, some elements are neutral or have a very weak influence on the phase stability, but they may provide other functions. For example, although Zr and Sn do not strongly promote neither phase, they retard the phase transformation. Moreover, Zr and Sn have extensive solid solubility in both α and β phases and can strength the alloy [7]. Figure 2-2 illustrates the α/β transformation temperature change when an α or β stabiliser is added to Ti. With more α stabiliser, the α/β transus temperature increases and the α phase region is thus ‘expanded’. Conversely, with more β stabiliser, the transus temperature decreases and the β phase can be retained at lower temperatures.

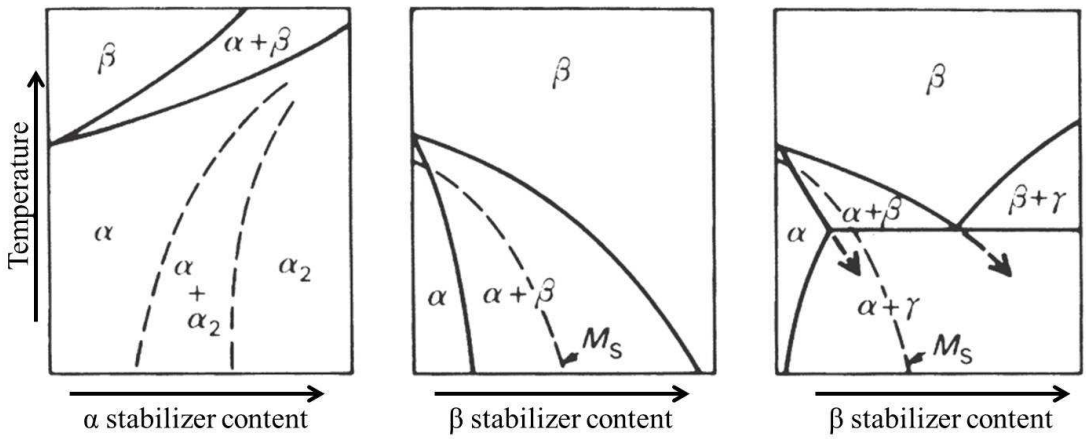

Figure 2-2. Effects of α and β stabiliser in changing the α/β transus temperature [6].

It should be noted that in Chapter 3, Ni and Sn are added to Ti because of their respective liquid phase forming mechanisms. In Chapter 4, 5 and 6, Al is alloyed with Ti to form the titanium aluminide intermetallics. The phase stabilising ability of those added elements are not the main considerations. The effectiveness and proper concentration ranges of alloying elements are based on empirical knowledge. For the α stabilisers, Eq. 1 and 2 express the relative effectiveness of some elements in terms of the oxygen and aluminium equivalents (wt.%), the two most potent α stabilisers [6]:

$$\mathbf{Eq(Al) = W_{Al} + 1/3W_{Sn} + 1/6W_{Zr} + 10W_O} \qquad \textbf{Eq. 2-1}$$

$$\mathbf{Eq(O) = W_O + W_{Mo} + (1.2\ to\ 2.0)W_N + 0.67W_C} \qquad \textbf{Eq. 2-2}$$

In terms of the β stabilisers, their effectiveness can be expressed in the following equivalence equation [6]:

$$\mathbf{Eq(Mo) = W_{Mo} + 1/5W_{Ta} + 1/3.6W_N + 1/2.5W_W + 1/1.5W_V + 1.25W_{Cr} + 1.25W_{Ni} + 1.7W_{Mn} + 2.5W_{Fe}} \qquad \textbf{Eq. 2-3}$$

Those equations are useful when modifying an alloy or designing a new composition. Among those typical alloying elements, the interstitial C, O, N elements (all α stabilisers) generate strong influences not only to the phase transformation behaviour but also to the mechanical properties. Figure 2-3 demonstrates that the tensile and yield strength, and hardness are all increased with higher addition contents. However, these benefits come at the expense of the tensile elongation. This effect is particularly pronounced with oxygen and nitrogen additions. Those interstitial elements are usually impurities from the extraction stage or the processing environment. In fact, the ASTM standard classifies commercially pure (99 to 99.5% purity) Ti as grade 1 to 4 according to their oxygen (and Fe) contents. In comparison, H (β stabiliser) in solution (up to 8 at.%, or ~0.15 wt%) has little effect on the mechanical properties, but can severely deteriorate the ductility (known as embrittlement) when hydrides form. In practice, it is found that no hydrogen embrittlement occurs when the H content is lower than 20 ppm (~0.1 at.%) [7].

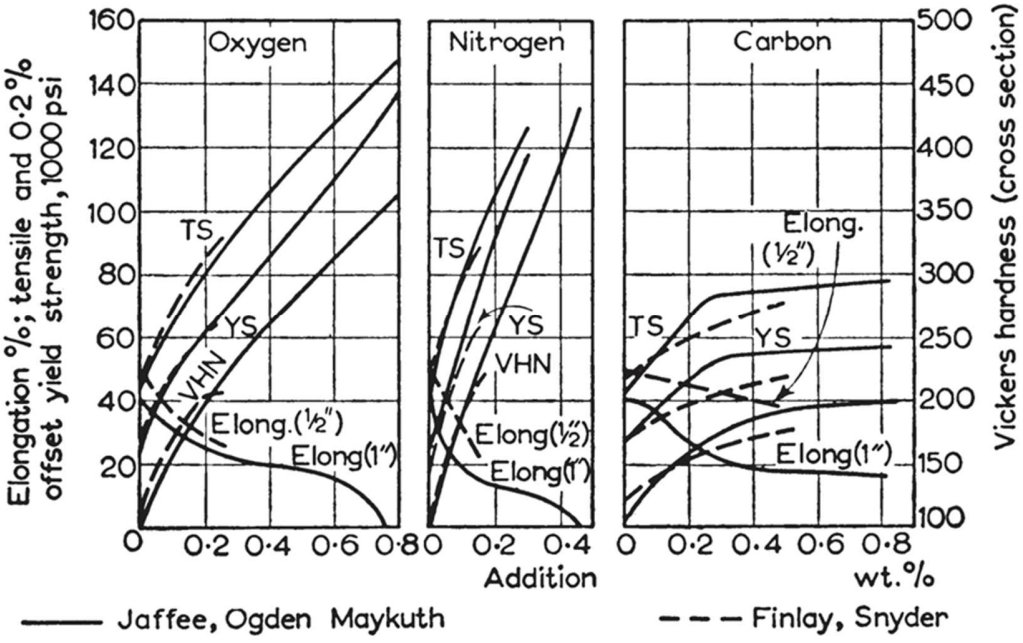

Figure 2-3. Interstitial element (O, N, C) alloying effects on the mechanical properties [7].

2.1.3 Microstructures

The alloying addition typically promotes or retains α or β phases, and accordingly affects the phase constituents. With different combinations of stabilising elements, the microstructure can be modified according to the application requirements. Ti alloys are generally categorised into four groups, according to their microstructure — α, near α (very little retained β), α/β (two-phased) and metastable β. To understand the phase formation mechanisms, the most popular Ti alloy Ti-6Al-4V can be assessed, which is an α/β two-phased alloy. Figure 2-4 presents the pseudo-binary phase diagram for Ti-6Al-4V, and also the formation sequences of its typical dual phase microstructure. When the alloy is annealed above the α/β transus temperature, the material exhibits entirely β grains. As the material is cooled down to the two-phased (α and β) region, the α phase begins to precipitate from the atomically densest directional planes (i.e. {110}) of the β phase (BCC structure). The newly nucleated α continues to grow until it encounters other grains. With the presence of β stabiliser, some β phase is consequently retained in between the long, acicular or rod-like α grains. Such a microstructure is typically described as the Widmanstätten pattern [7].

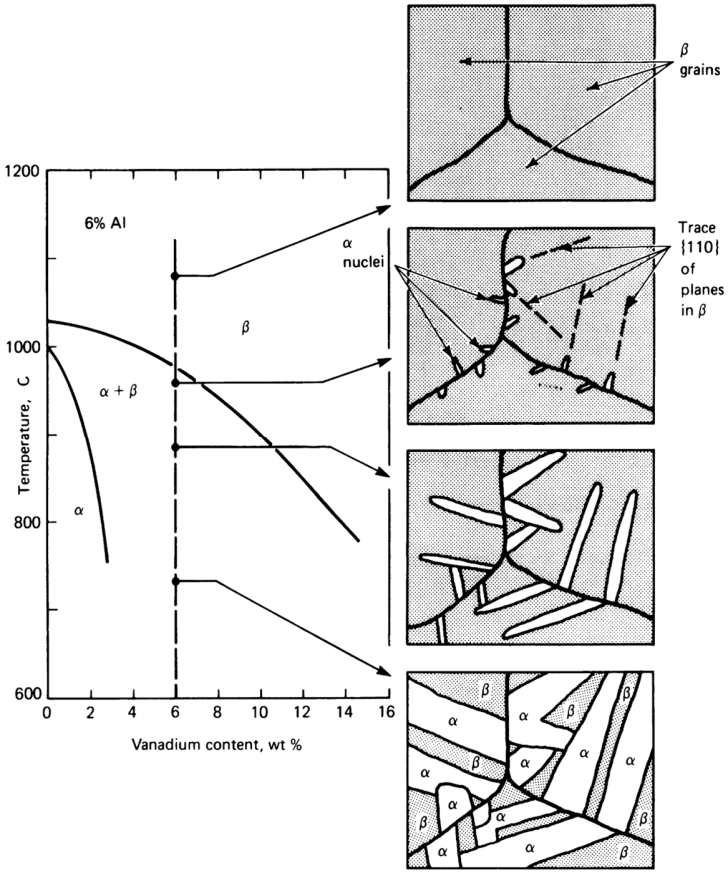

Figure 2-4. Microstrucutre formation mechanisms of the Ti-6Al-4V (α/β) alloy [7].

Microstructure is also a function of prior cold work, temperature from which the sample is cooled and the cooling rate. Therefore, various microstructures can be achieved. If the same Ti-6Al-4V alloy is cooled down from the β region at a relatively rapid rate (i.e. water cooling), only very fine, martensitic-like acicular α precipitates form within the 'frozen' β phase (Figure 2-5). In comparison, when the material is cooled down from the α/β region, a seemingly equiaxed grain structure forms. The microstructure consists of a certain α to β ratio, according to the temperature that it is cooled from, with no signs of the large primary β grains.

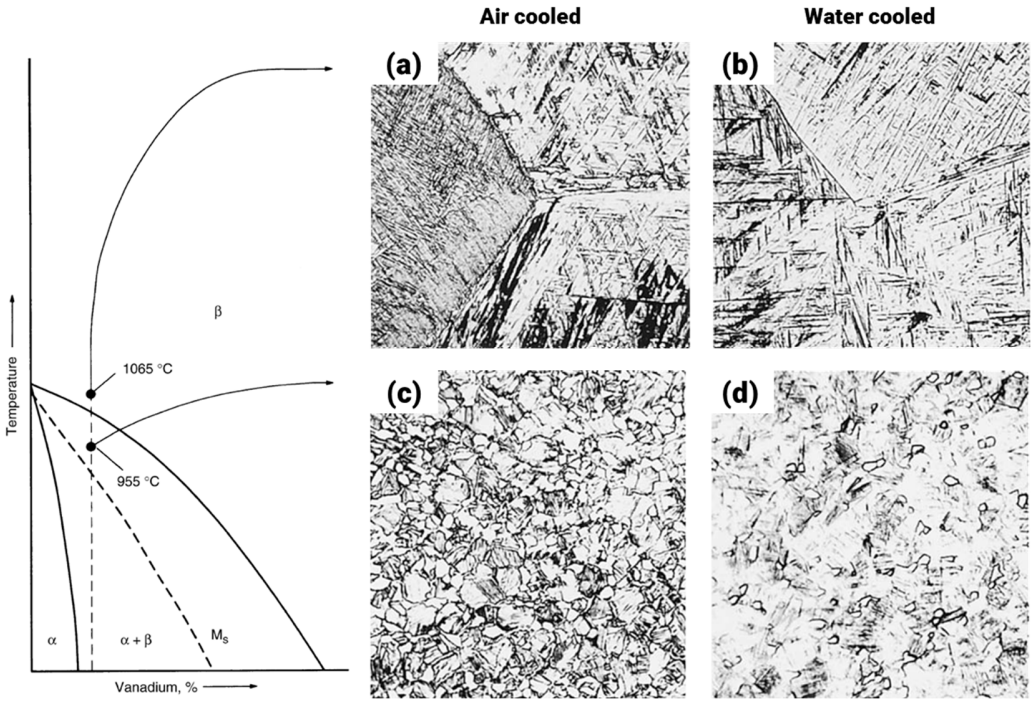

Figure 2-5. Microstructures of an annealed α/β Ti-6Al-4V alloy after cooling from the β region with two cooling rates: (a) air cooled, and (b) water cooled; (c) and (d) are microstructures annealed in the α/β region, and air cooled and water cooled, respectively [7].

In the case of a highly pure Ti (>99.55% purity) material, regardless of the cooling rate or initial annealed temperature (in either α or β region), the microstructure does not exhibit the long α rods, but instead an equiaxed single-α phase. Without the β stabiliser, even rapid cooling does not supress the β to α transformation and consequently no β phase can be retained. However, Ti can be easily contaminated from C, O, and/or N during processing, particular in powder metallurgy. Therefore, commercially pure Ti sometimes consists of the long α rod structure.

2.2 Ti-Al Intermetallic Alloys

2.2.1 Properties and Structure

Titanium and its alloys have shown excellent properties, as discussed previously. However, their inadequate strength and severe oxidation above 500°C limits the use of this lightweight material. Although some conventional wrought and cast titanium alloys still provide adequate strength at above 595°C, long-term stability is often the main concern [7]. As a result, applications such as engine components, which can have service temperatures above 500°C, are still dominated by the heavy iron or nickel-based superalloys.

In comparison to Ti alloys, titanium aluminide intermetallic compounds have received considerable attention due to their unique thermal-mechanical properties since the 1950's. They have shown promising properties for high temperature applications. Even better than Ti alloys, titanium aluminides exhibit lower densities (~3.9-4.1 g/cm^3), high specific moduli, and good tensile strengths and creep properties at elevated temperatures up to ~700°C. In the Ti-Al binary system, shown in Figure 2-6, there are three intermetallic phases: α_2, γ and $TiAl_3$. Among them, only the α_2 and γ phase alloys have received significant interest and have consequently been intensively researched; these intermetallics will be discussed in some detail in this thesis (Chapter 4-7). The crystal structure of these two phases are presented in Figure 2-7. The α_2 phase is a hexagonal $D0_{19}$ structure, based on the composition of Ti_3Al, while the γ phase is the tetragonal $L1_0$ structure, based on the TiAl composition.

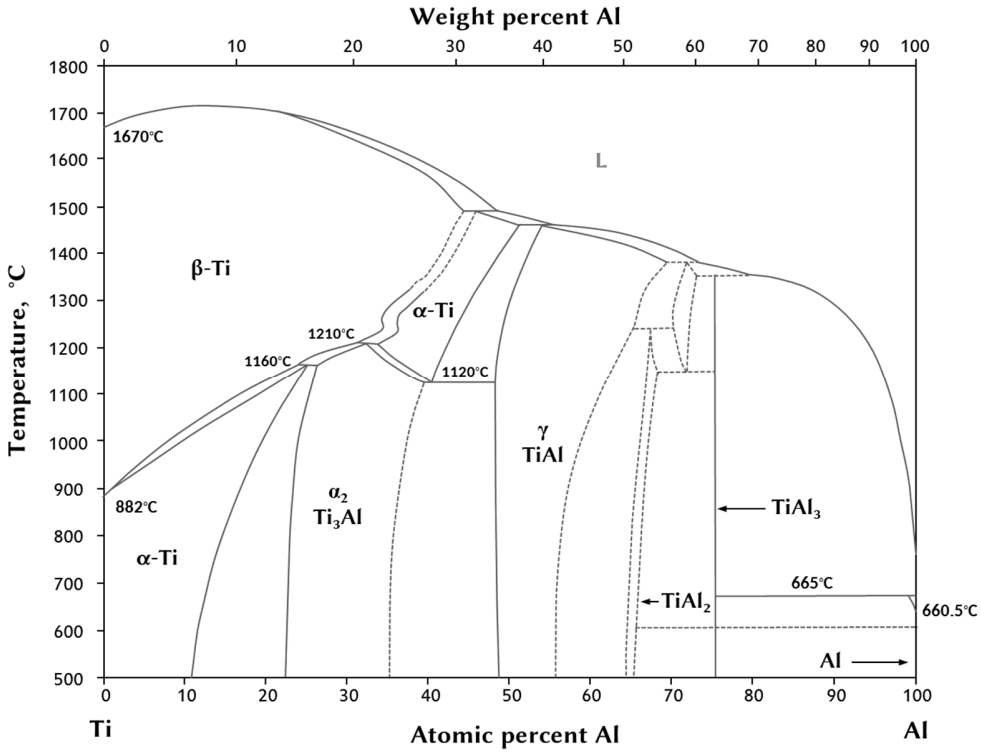

Figure 2-6. Titanium-aluminum binary phase diagram (redrawn from [8]).

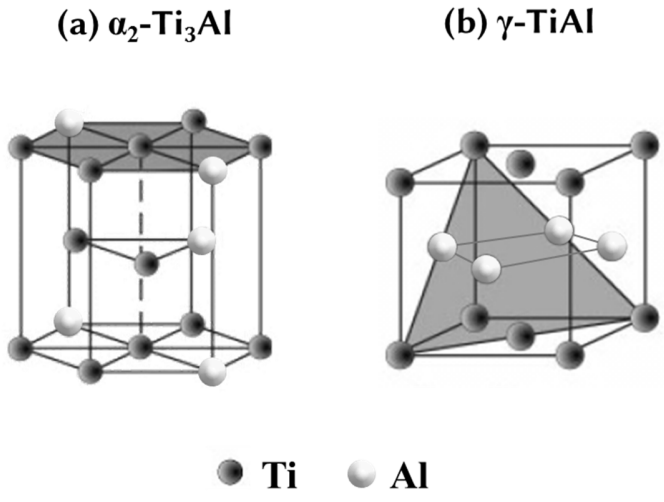

Figure 2-7. Crystal structure of titanium aluminide intermetallics: (a) α_2-Ti_3Al and (b) γ-TiAl (modified from [2]).

Various intermetallic or high temperature metastable phases can exist, depending on the alloying and heat treatment conditions. The alloys or phases are sometimes referred to by their structure designation in the literature. A summary of the designations is provided in Table 2-2.

Table 2-2. Phase and crystal structure designation of titanium-aluminium alloys.

Phase	Structure designation (Strukturbericht)	Based composition	Lattice structure
α	A3	Ti solid solution	hcp
α_2	$D0_{19}$	Ti_3Al	ordered, hexagonal
β	A2	Ti solid solution	bcc
β_0/β_2*	B2	Ti solid solution	ordered bcc
O	A_2BC	Ti_2AlNb	orthorhombic (Pearson index)
γ	$L1_0$	TiAl	tetragonal

**The designation is not consistent and both can be seen in literatures.*

Despite the aforementioned advantages of titanium aluminides, they generally suffer from low ductility at ambient temperature, and consequently low fracture toughness, predominantly due to their crystalline nature. As aluminium is added to titanium, to form the α_2 phase, Al atoms occupy the titanium lattice. The hexagonal (α-Ti) structure is distorted and some slip modes are thus hindered, such as the cross (prism) slip ($\vec{c} + \vec{a}$), causing a tendency of planar slip in the alloys, as shown in Figure 2-8. Substantial planar dislocations accumulate at the grain boundaries and consequently create stress concentration which leads to transgranular fracture (Figure 2-9).

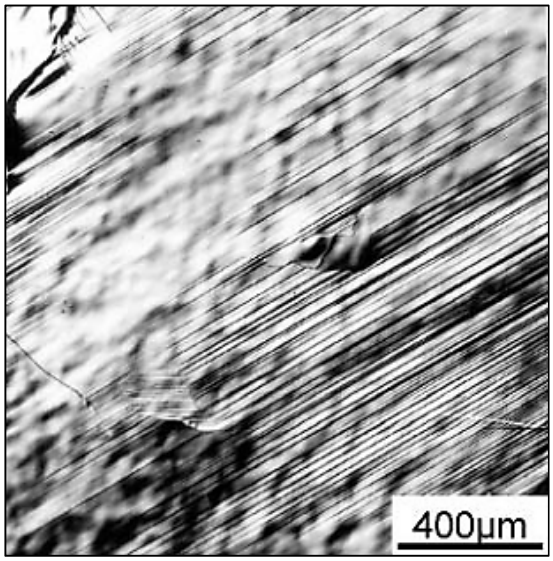

Figure 2-8. Optical micrograph of planar slip lines on the polished α_2 (Ti_3Al) surface [5].

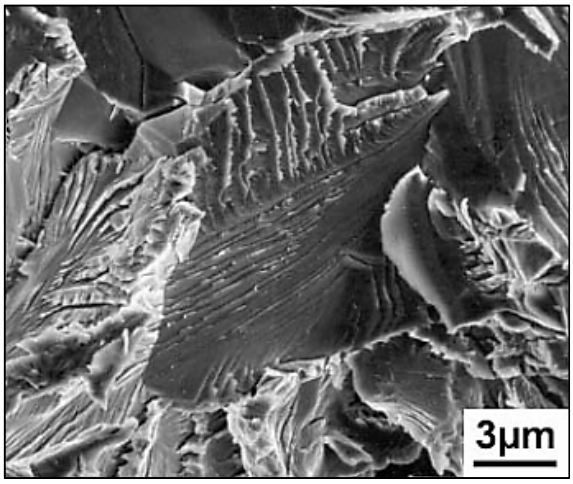

Figure 2-9. SEM micrograph of the α_2 (Ti_3Al) fracture surface, showing cleavage cracks [5].

In addition, the long-range ordered structure exhibits anti-phase boundaries (APB), which can hinder the dislocation movement by breaking up the ordered atomic arrangement. Consequently, the low ductility is in part because there are fewer active slip systems, as well as twining occurring, and the dislocation movement is harder in such structures. Therefore, the ordered α_2-Ti_3Al phase generally exhibts lower ductility than the disordered

α-Ti phase. In fact, the unalloyed α_2 phase has essentially 0% ductility at room temperature. On the other hand, γ phase alloys exhibit moderately higher ductility (~2% elongation) compared to the α_2 alloys, due to their tetragonal structure which provides easier slip modes [5].

With regards to the microstructures of titanium aluminides, there are three typical types: full lamellar, bi-modal (also known as duplex or fine-grained lamellar [9]) and equiaxed structures. Those microstructures are predominately controlled by heat treatment and, to some extent, by alloying effects, which will be discussed later. Figure 2-10 illustrates the microstructures obtained by quenching from various temperatures (in the 45-48 at.% Al compositional range). While the fully lamellar structure is beneficial to creep strength, especially for high temperature applications, the consequent low ductility and fracture toughness would make machining difficult, increasing the cost of manufacturing. In comparison, the equiaxed grains contribute to better ductility, which is critical for processing. However, this structure might suffer from insufficient creep strength. Therefore, a balanced combination of microstructures should be considered in terms of their applications.

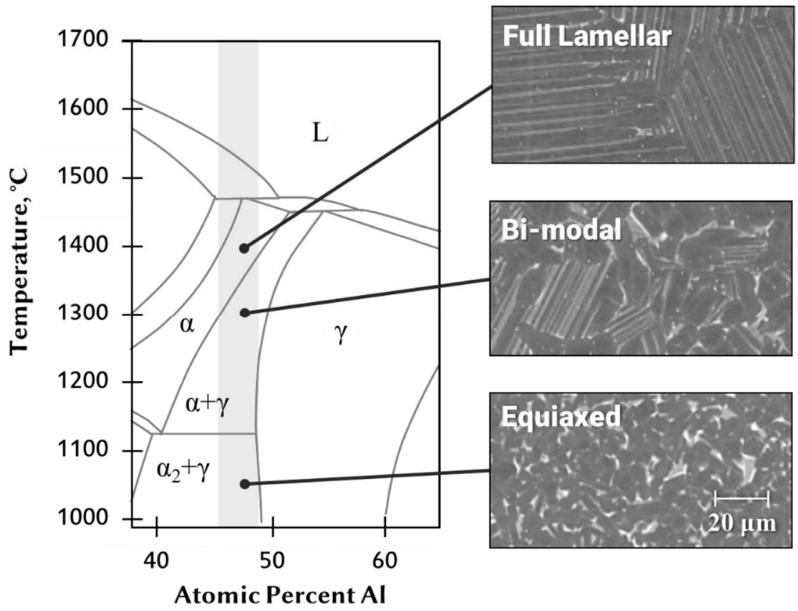

Figure 2-10. Microstructure of titanium aluminides (45-48 at.% Al) annealed and subsequently cooled at moderate rates from α, α+γ and α_2 + γ phase. (figure modified from [2]).

2.2.2 Effects of Alloying Additions

The effects of alloying additions to the Ti-Al intermetallic are similar to that for the Ti alloys; that is, elements can affect the α/β transus temperature. However, the effects are more complicated in the case of the Ti-(40-50 at.%)Al intermetallic system. Figure 2-11 presents an example of the phase boundary transition when adding 8 at.% Nb. The β stabiliser promotes the β phase by lowering the α to β transus temperature, and the α phase (not α_2) region is greatly compressed in the phase diagram.

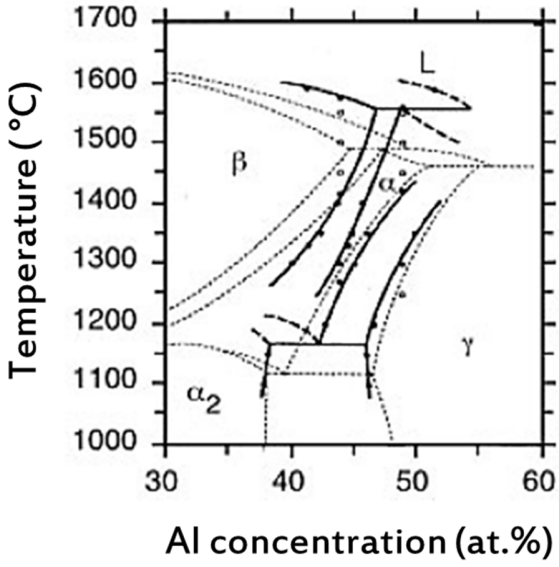

Figure 2-11. Ti-Al phase transition affected by Nb addition (8 at.%) [2].

In addition to the phase stabilising ability, several elements have been found to serve unique functions, which are summarised in Table 2-3. Among them, Nb is receiving significant interest for the titanium aluminide system, because it not only improves properties, but also introduces a different phase (orthorhombic Ti_2AlNb) when adding a relatively large amount. However, this orthorhombic phase is beyond the focus of the current study. It should be noted that each alloying element may have different functions and effectiveness on the α_2-Ti_3Al and γ-TiAl based alloys. Furthermore, in a multi-element

system, when there is chemistry inhomogenity, the material's properties will be affected by the complex local alloying, and the effects of alloying elements will be difficult to accurately predict. For instance, an element may cause solid solution hardening in one phase, but change to precipitate hardening, due to the local phase alteration, under the influence of a phase stabiliser.

Table 2-3. Functions of alloying elements (summarised from [2]).

Element	Function
Cr, Mn, V	Lowering the stacking fault energy, mechanical twinning, increasing the ductility
Ta, W, Mo, Si, C	Improving high temperature properties: oxidation resistance, creep strength
B	Forming TiB_2 boride (providing nucleation sites for α, β), refining grains (reducing the lamellae spacing)
Nb	Increasing yield strength, creep (slow diffuser in γ, reducing the diffusion rates) and oxidation resistance (1-2 at.%)

Other than the elements listed in the table, the largest quantity addition in the alloy is, in fact, aluminium. The extensive amount of aluminium not only reduces the density, but also enhances the oxidation resistance of the alloys. The aluminium can form a more protective Al_2O_3 layer on the alloy surface, despite the fact that TiO_2 provides remarkable protection in corrosive and atmosphere environments at low temperature. At temperatures above 550°C, oxygen can diffuse deeper and generate more titanium oxide, given that titanium has high affinity with oxygen, and oxygen has high solubility in titanium [5]. Figure 2-12 illustrates the oxide layers in different alloys and the relative depth of oxygen diffusion. If oxygen forms a layer of α phase (known as α case) under the surface, it can cause embrittlement in the alloys. In fact, the development of α_2 and the later orthorhombic alloys was discontinued because of the rigorous environmental embrittlement occurring for high temperature applications, whereas γ-TiAl alloys (with more Al) provide better oxidation resistance [7].

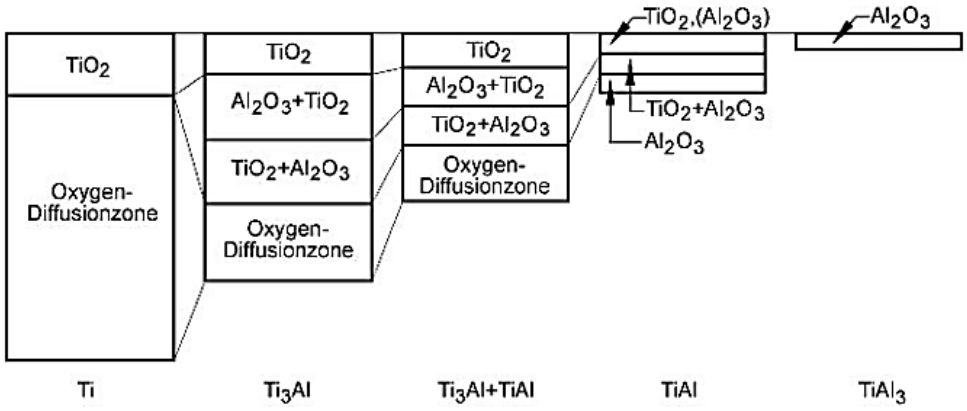

Figure 2-12. Surface oxide layers and the penetration of oxygen in titanium, Ti_3Al, TiAl and $TiAl_3$ intermetallics [5].

2.2.3 γ-based Intermetallic Alloy Development

The development of titanium aluminides began with the simple Ti-Al binary compositions, with the goal of improving the low ductility and fracture toughness at room temperature, as well as the oxidation resistance above 700°C. Considerable efforts have subsequently been dedicated to enhancing the aforementioned disadvantages, through alloying and/or thermal treatment.

The initial research had found that the two-phase Ti-(45-48 at.%)Al alloy, consisting of γ (TiAl) and α_2 (Ti_3Al) phases, can reach the "maximum" ductility for this γ based intermetallic alloy, even though Ti_3Al is more brittle than TiAl. This is because the α_2 phase has higher impurity solubility, and can therefore accommodate most of the impurities. The existance of the α_2 phase thus eases the embrittlement in the γ phase. As a consequence, subsequent development of the γ-based alloys were based on this composition of 45 to 48 at.% Al. In comparison with the α_2-based alloys, the γ-based alloys generally have lower tensile strength, from 375 to 650 MPa, but a higher ductility, typically from 0.5-3% [7]. Nevertheless, the two-phase alloys still could not provide sufficient ductility at room temperature for metal working and meet the stringent creep strength and

oxidation resistance requirements of, for example, the critical turbines in jet engines, operating at extremely high temperature.

In order to improve these inadequate properties, research on the second generation of γ-based alloys has focused on the alloying effects. The alloying additions can be summarised using the formula:

Ti-(45~48)Al-(1~3)X-(2~5)Y-(<1)Z **Eq. 2-4**

where X=Cr, Mn, V; Y=Nb, Ta, W, Mo and Z=Si, B, C. These alloying elements, as in the X and Y categories, are the metallic additions, while the Z group represents the non-metallic additions. The alloying effects for the second generation alloys are generally clear: the metallic additions dissolve in the γ phase as a solid solution and alter the phase's intrinsic properties, for instance, the X additions (Cr, Mn or V) enhance ductility through lowering the stacking fault energy of the γ phase. On the other hand, the non-metallic additions form a third phase and influence the microstructure. The Z additions (Si, B, or C) form (silicide, boride, or carbide) phases which refine the grain size, restricting coarsening. The effects of alloying elements have been presented earlier in Table 2-3. It should be noted that there is generally only as much as 2 at.% solubility in the γ phase for most metals. The excessive content will precipitate out as a third phase (β_2). However, for Zr, Nb, Ta, they have higher solubility; and particularly in the case of Nb, it can significantly dissolve up to 9 at.% in the γ phase.

The current development of γ-TiAl based alloys (i.e. third generation materials) focuses on the Nb concentration. Unlike the high Nb concentration in the α_2 and O phase alloys, the γ phase alloys only contain 5-10 at.% Nb. Researches have shown that alloying 5-10 at.% Nb considerably strengthens the TiAl alloys, exceeding the yield strength of 800 MPa [2]. However, in contrast to the α_2 and O phase alloys, the strengthening mechanism in the γ phase alloys is still not clearly understood. Nevertheless, there is controversy about whether the strengthening is caused by solid solution or the phase structure changing. Table 2-4 summarises the effects of Nb addition in the alloys.

Table 2-4. Effects of Nb in titanium aluminide alloys.

In α_2 phase alloys (10-20 at.%)	In O phase alloys (21-27 at.%)	In γ phase alloys (5-10 at.%)
• producing fine α_2 laths (main strengthening mechanism) • forming β_2 phase (ductile than α_2 and stress concentration relaxation) • increasing oxidation resistance	• precipitation hardening • forming orthorhombic structure (ductile) • increasing oxidation resistance	• Strengthening (mechanisim not clear) • increasing oxidation resistance

Other than Nb, it is found the carbon addition in the range of 0.2 to 0.4 at.% precipitates the Ti_3AlC phase (perovskite type structure) in the alloy and improves the strength and creep properties. The effects on precipitation hardening caused by silicide, $Ti(Cu,Al)_2$ Laves phase or other third phase precipitate, have also been investigated in the third generation γ based alloys [10].

2.2.4 Aviation and Automobile Applications

As described in the earlier sections, TiAl-based alloys possess unique characteristics, particularly light weight and high strength at high temperatures. Consequently, TiAl alloys are potentially an ideal material for engine components which are constantly under high temperatures. However, due to the high production cost, there are few commercial applications. Aircraft manufacturers are among the earliest participants in the development of the TiAl alloys. Many titanium aluminide projects (e.g. High Speed Civil Transport, HSCT) have been carried out successfully in the last century and some first-generation TiAl alloys have been developed and utilised in several commercial aircraft [11]. The European Space Agency has also carried out the Intermetallic Materials Processing in Relation to Earth and Space Solidification (IMPRESS) project to validate some specific TiAl alloys for engine applications [12]. In recent years, more attention is focusing on automobile applications for these alloys. Several German automobile companies and research institutes have been working together on prototyping of TiAl

engine parts since the late 1990s [13]. The following section briefly touches on some commercial applications in the aviation and automobile industries.

Aviation

For the aviation industry, the drive to cut fuel consumption has significantly increased due to the fluctuating fuel price and associated environmental concerns. In order to achieve such goals, lighter materials are required to reduce the total weight and thus the fuel consumption. Alternatively, better fuel efficiency can be achieved by increasing the engine operating temperature.

In commercial engine applications, titanium aluminide alloys have been adopted for aircraft use in areas such as the low pressure turbine (LPT) jet engine blades. Two main γ-TiAl based alloys have been developed and tested successfully at 560-750°C for such applications since the 1990's. These two alloys are the Ti-48Al-2Nb-2Cr, developed by the General Electric Company, and the Ti-45Al-2Nb-2Mn + 0.8 vol.% TiB_2 (XD) alloy produced by Howmet Corporation [11].

Figure 2-13 shows the implementation of Ti-48Al-2Nb-2Cr blades in the CF6-80C2 engine. The decrease in turbine blade weight eases the centrifugal force on the rotor disk. As a consequence, a smaller rotor can be implemented, further decreasing the weight of the rotor set. Conversely, the weight saving from using TiAl can be used to increase the size of the blades or other components to further improve performance. This material (Ti-48Al-2Nb-2Cr) has also been tested for other applications, such as the transition duct-beam (Figure 2-14) for the GE90 engine [14].

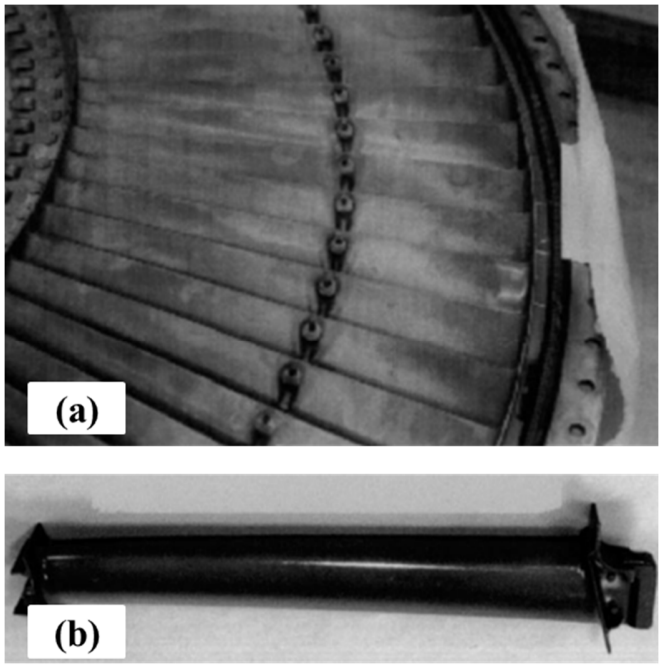

Figure 2-13. (a) Complete stage 5 rotor set with TiAl cast blades. (b) Individual turbine blade [14].

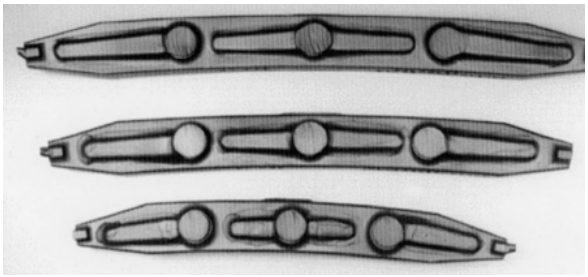

Figure 2-14. TiAl transition duct-beam, cast for the GE90 engine [14].

In terms of cost, TiAl alloys are very expensive to manufacture, even starting with the economical casting process. The benefit of casting is outweighed by the subsequent hot isostatic pressing, chem-milling and machining. However, for the aviation industries, high performance and reliability are the most important considerations. In order to adopt TiAl intermetallics in the aircraft design, the material must demonstrate its long-term properties can match, for instance, the requirements of a low-pressure turbine, as listed in Table 2-5.

On the other hand, there are applications of TiAl aimed at low risk or non-critical components, such as the divergent flaps (Figure 2-15), nacelle structures, and acoustic honeycombs for noise cancellation [14].

Table 2-5. Mechanical properties for a low pressure turbine [2].

Mechanical properties	Requirement
High cycle fatigue strength (10^7 cycles)	≥ 350MPa at RT and 700°C
Low cycle fatigue strength (10^4 cycles)	≥ 350MPa at 700°C
Time to 1% creep	≥1000 h at 150 MPa and 700°C
Room temperature ductility	≥1%
Sufficient oxidation and corrosion resistance at 700°C	

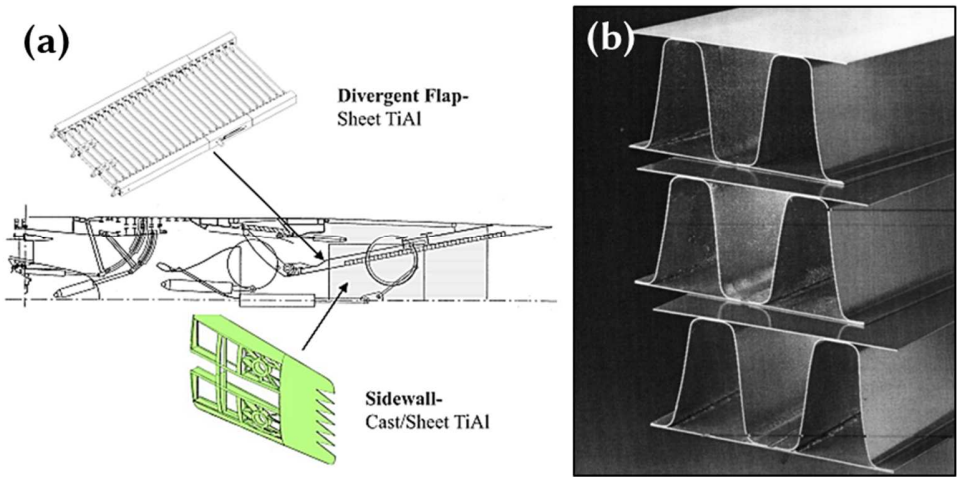

Figure 2-15. TiAl alloy applications (a) divergent flag and sidewall of the nozzle [11]. (b) Sub-element of the divergent flag [14].

Automobiles

For automobile applications, the component requirements are not as stringent as for the aviation standards. For example, the property demands of an exhaust valve are listed in Table 2-6, highlighting that the requirements are not as focused on the reliability (i.e. fatigue and creep property), in comparison to the low pressure turbine application (Table 2-5). However, the automobile industry is very cost sensitive. Currently, titanium aluminide material really can only be seen, for example, in Formula One racing cars or some high-end vehicles. Two of the most suited applications are for exhaust valves (Figure 2-16) and turbocharger rotors (Figure 2-18), in engine applications [13,15].

Table 2-6. Property requirements on an automobile valve [13].

Mechanical properties	Requirement
Tensile strength (MPa)	≥500
Yield strength at 0.2% strain	≥350
Elongation (%)	≥1
High temperature strength at 800°C (MPa)	≥165
Stressability boundary at 107 cycles (MPa)	≥250
Creep strength 1000 h at 800°C	≥50
Thermal expansion coefficient (10^{-6} K^{-1})	≥25

The use of TiAl alloy as an exhaust valve is aiming to replace the most common heat-resistant steel, grade 21-4N, or the wrought IN75 for high performance valves [16]. The benefit of applying TiAl material not only results from the total weight reduction, but also the fewer occurrences of "valve jump", which is the condition when the valve is not in contact with the camshaft lobe (Figure 2-17). In a high temperature environment, the exhaust valve is subjected to a great deal of wear and erosion from the combustion engine movement. Consequently, anti-erosion surface treatments such as plasma carburization and nitriding are recommended to ensure sufficient endurance [15].

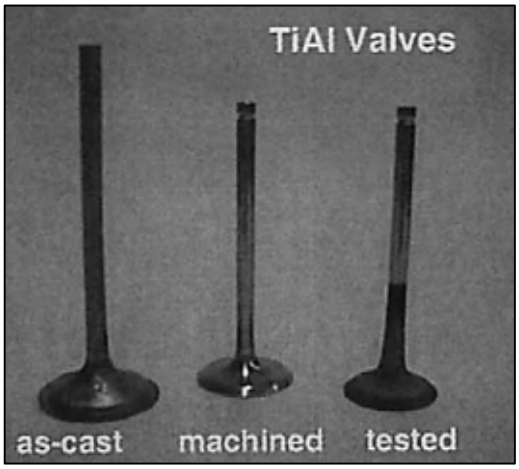

Figure 2-16. The appearance of titanium aluminide exhaust valves at different conditions [13].

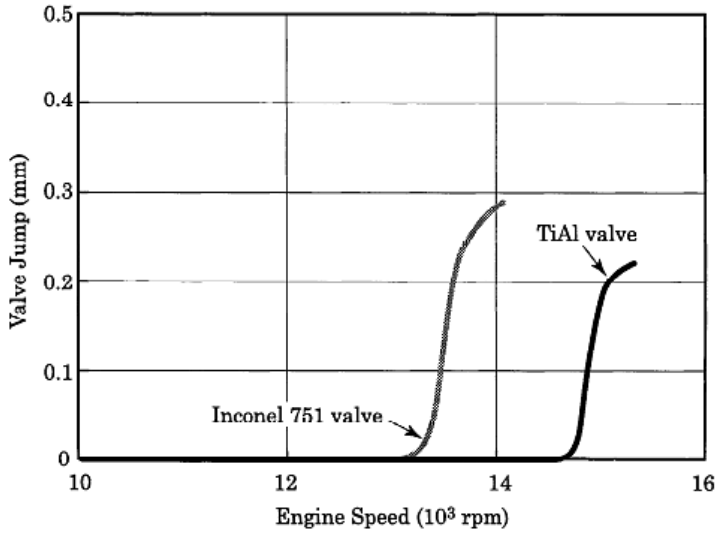

Figure 2-17. Valve jump comparison of TiAl valve and conventional IN751 valve at different engine speed [15].

In terms of the TiAl turbocharger, it was firstly adopted by Mitsubishi Ltd in the Lancer VI 2.5 litre engine, in 1999 [2]. The Mitsubishi TiAl turbocharger, which contains 7 at.% Nb, is shown in Figure 2-18 [17]. Other TiAl alloys were also developed for turbocharger rotors, such as the Asea Brown Boveri ABB-2 alloy. The turbocharger rotor

then is joined to a steel shaft, using IN909 brazing alloy and electron beam welding [14]. The TiAl alloy turbocharger is targeted at replacement of the heavy cast IN713C material. Again, adopting the TiAl alloy not only reduces the total weight, but also increases the engine performance from a more responsive turbocharger (i.e. reduced turbocharger 'lag'). The engine is swifter to respond to throttle input and therefore there is lessened delay using TiAl compared to IN713C, as demonstrated in Figure 2-19 [17].

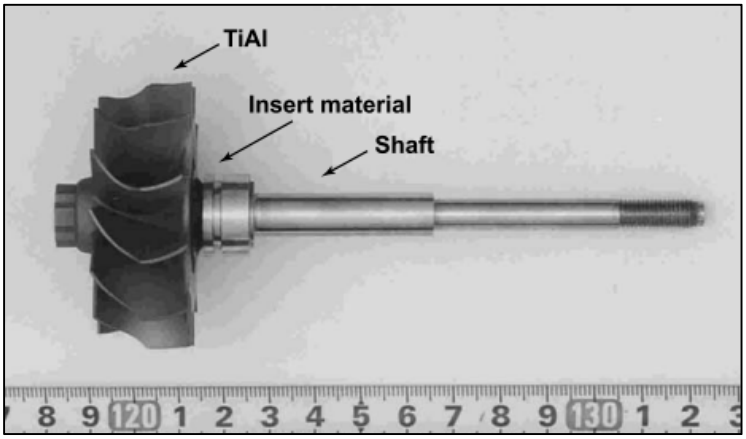

Figure 2-18. TiAl turbocharger developed by Mitsubishi Heavy Industries Ltd. [17].

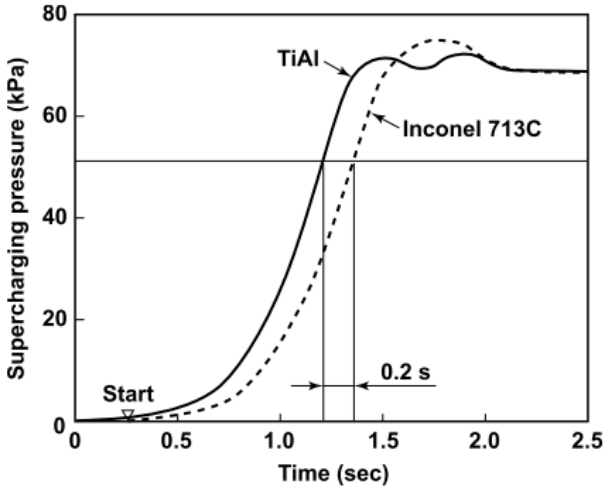

Figure 2-19. Response time of a TiAl and a Inconel 713C turbocharger [17].

While exhaust valves suffer from wear damage, turbochargers are exposed to a higher temperature environment (850°C) from the exhaust gas, compared to 750°C for the exhaust valve [15]. Therefore, oxidation resistance is a critical consideration for a turbocharger material. To improve the oxidation resistance, practical approaches include alloy development to modify the properties intrinsically and/or anti-oxidation coatings. However, it has also been reported that the oxidation was not as severe as expected in an actual engine endurance test [17]. The cross-sectional SEM of the TiAl surface, as shown in Figure 2-20, indicates the oxide layer is relatively insignificant, while a layer of adhesive material, with Ca, Zn, P and Fe components (likely from the gasoline and tubing) is present. The exact reason for the formation of this layer is not clear, but the adhesive film might function to stabilize a dense Al_2O_3 protective scale.

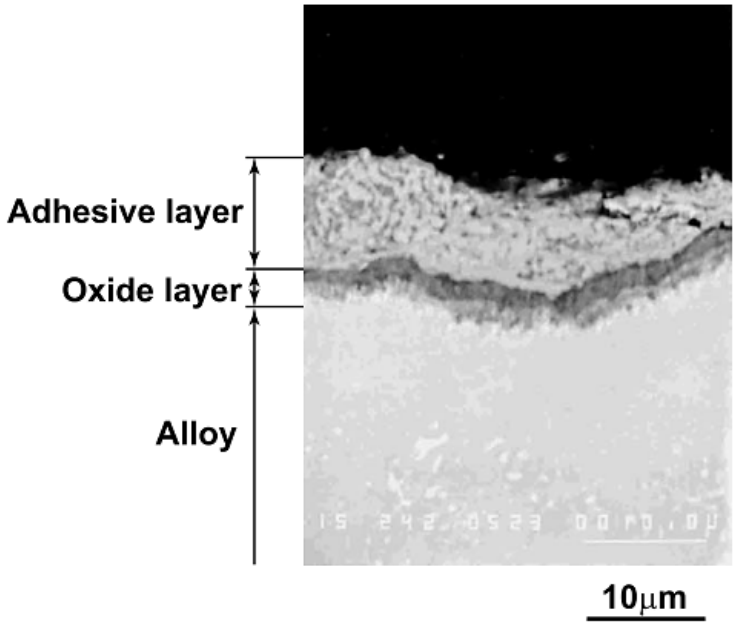

Figure 2-20. Backscattered electron SEM micrograph of the surface of a TiAl turbine wheel after an engine endurance test [17].

2.3 Conventional Fabrication Methods for TiAl

This section introduces some TiAl manufacturing processes, focusing on the exhaust valve and turbocharger production, starting from the forming of ingots (cast), and then subsequently thermomechanical processing steps, including forging and extrusion. Conventionally, the steel or superalloy exhaust valve and turbocharger rotor are manufactured by hot forging and precision casting, respectively [16]. So far, titanium aluminides are manufactured predominately by casting, and some reactive sintering, because of the relatively low associated production costs and fairly simple processes.

2.3.1 Ingot Production and Casting

To produce the desired γ-TiAl based ingots, the process starts from pressing the metallic titanium and aluminium, with some optional alloying elements, to form the electrodes for the subsequent melting process, such as the vacuum arc remelting (VAR) process, as illustrated in Figure 2-21[2]. The electrode composition is compensated for the loss of aluminium from evaporation during the melting process. Due to the high reactivity of titanium and aluminum with oxygen, the melting process is carried out under vacuum to prevent oxidation and other contaminations.

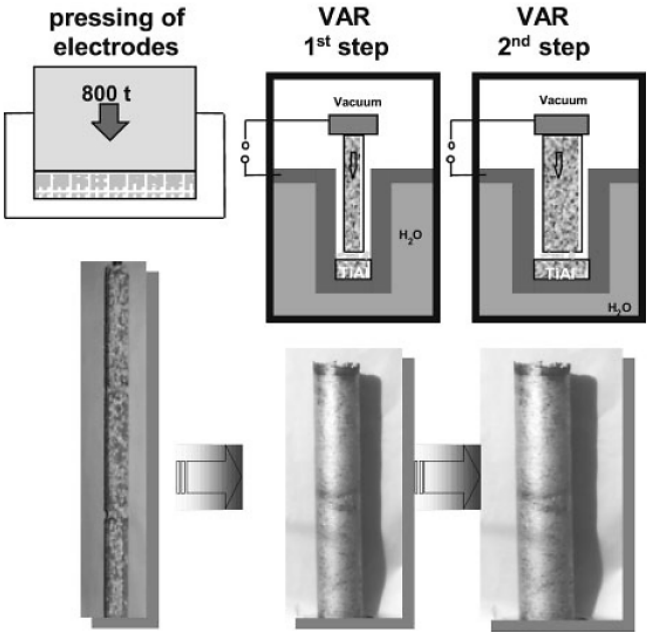

Figure 2-21. Vacuum arc remelting (VAR) process steps, and the corresponding ingot appearances [2].

In the VAR process, the electrode is melted at the bottom by an electric arc which is generated through high voltage application. The melt drips down into a water-cooled copper crucible, and the crude ingot is therefore formed. However, the large difference in melting temperatures and densities of various elements, as well as the occurrence of peritectic solidification, can cause macroscopic segregation within the ingot [2]. Hence the ingot usually undergoes re-melting or even triple melting to improve the chemical homogeneity and purity.

Nevertheless, the aluminium content in the ingot can still vary by more than ±2 at.% at different locations [2]. Furthermore, there is microscopic scale segregation in the lamellae structure. Some unwanted inclusions, such as refractory (high melting) alloying elements (e.g. Ta), may not fully dissolve in the matrix [2]. The fluctuation in composition distribution affects the mechanical properties, making the subsequent thermomechanical process (e.g. forging and extrusion) difficult to control. As a result, heat treatment steps such as annealing or hot isostatic pressing (HIP) are necessary to ensure chemical

homogeneity and to remove residual porosity [18,19]. The use of master alloys for production can also minimize the inhomogeneity.

The casting process is a similar concept to ingot production in terms of the material melting procedures, except for the fact that the mould is designed in the shape of the final (or intermediate) product. The heating source may vary, for example using an induction coil. The melt material is the feedstock for the casting process. Other than the conventional melt pouring process, two casting processes that are developed for TiAl manufacturing (i.e. LEVICAST and centrifugal casting) are introduced here.

LEVICAST

Conventionally, Ni-based superalloy turbine wheels are manufactured by the counter-gravity low-pressure casting of vacuum-melted alloys (CLV) process. This method applies a low pressure, maintained outside of a permeable ceramic shell mould, to suck up the melt into the mould cavity. This process has a great advantage in terms of filling the mould cavity and reducing pinhole casting defects, and thus produces components with fine and complex details.

In the case of TiAl manufacturing, the high reactivity of titanium and aluminium with oxygen as well as the ceramic mould at high temperature pose a high risk for contamination. The LEVICAST process, developed by Daido Steel, is designed primarily for TiAl casting. The process, as illustrated in Figure 2-22 [16], prevents oxidation by using a protective Ar atmosphere in the melting chamber, as well as an induction heated and water-cooled crucible for the TiAl melt, in order to avoid reactions with a ceramic mould (e.g. a CaO crucible). Therefore, the level of oxygen and other contaminants in the TiAl casting produced by this process are significantly minimised [16].

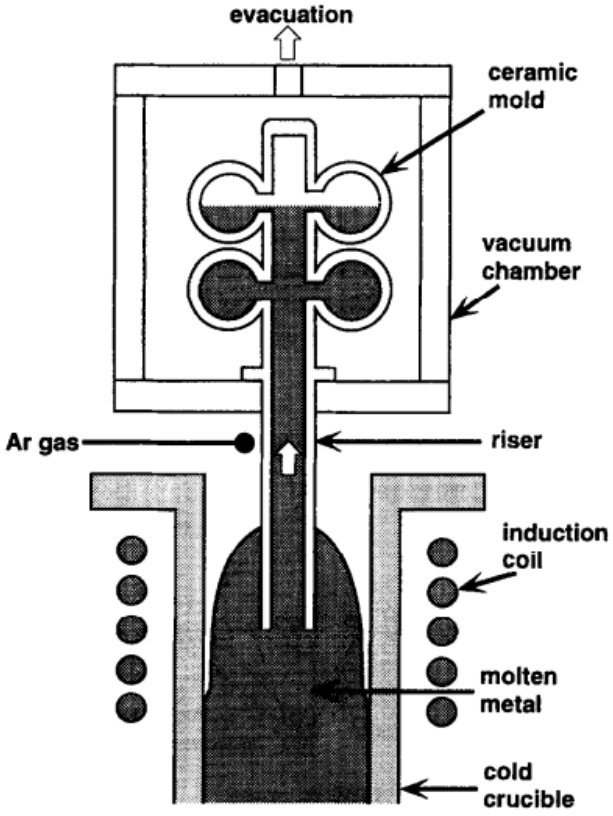

Figure 2-22. A schematic representation of the LEVICAST process [16].

Due to the complex geometry of the turbine wheel, the only method to produce the turbocharger is investment casting, also known as the ‘lost wax’ process [15]. In contrast to the use of a permanent mould, investment casting employs a one-time use ceramic mould, for example as seen in Figure 2-23. The turbocharger wheel is used ‘as cast’ and no further machining is applied.

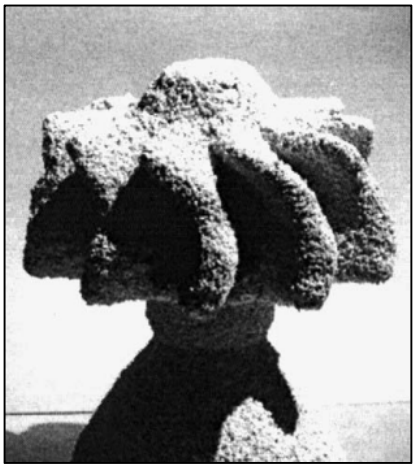

Figure 2-23. Investment casting mould for TiAl turbine wheel [20].

Centrifugal casting

Centrifugal casting was developed by ALD Vacuum Technologies AG, to minimise conventional casting defects, such as porosity. Similar to the LEVICAST process, this approach also uses a induction heated cold crucible to melt the material under vacuum. But the molten TiAl is poured into a permanent mould of several individual valve components (Figure 2-24) [13]. The permanent mould is heated in a gradual manner and is spinning on a turntable when the melt is poured into the mould. Utilising the centrifugal force, the melt is forced to fill the cavity of the mould, decreasing the porosity defects after casting. The centrifugal casting procedure is shown schematically in Figure 2-25 [13].

No macroscopic segregation in chemical compositions is found in the as-cast product. Any micro segreation observed is also very insignificant. However, there are some shrinkage cavities that can be observed at the centre line of the valve stem [13]. This process is fairly fast, giving a production rate of approximately 50 valves in 30 minutes, making the process more economical. Under the MaTech programme, initiated by ALD Vacuum Technologies AG, a prototype plant with a production capacity of 6,000,000 valves per year was built in 2001 [13].

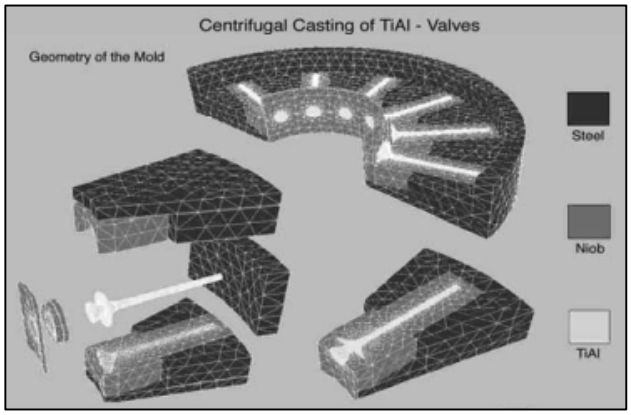

Figure 2-24. Centrifugal casting mold design [13].

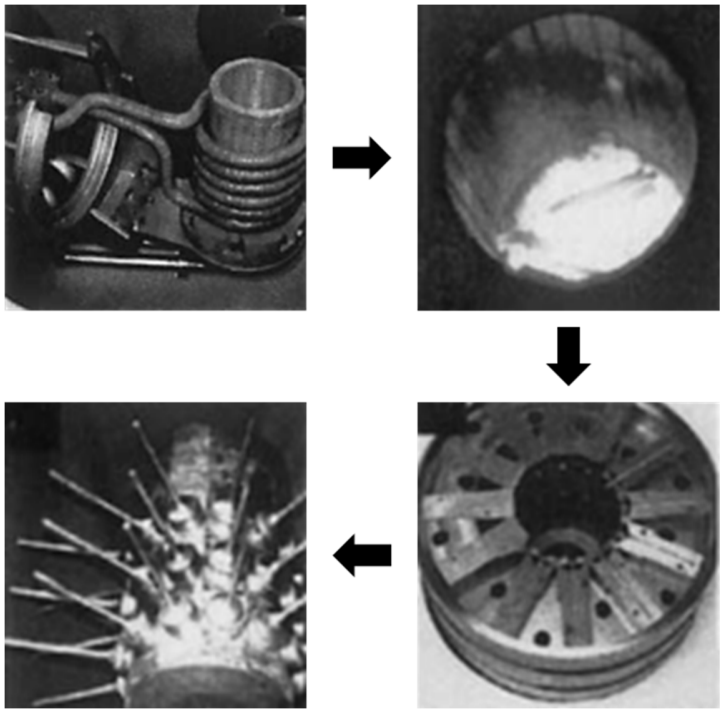

Figure 2-25. Centrifugal casting procedures, staring with melting of the material in an induction heated cold crucible. The melt is poured in the spinning permanent mold. Figure is modified from [13].

2.3.2 Thermomechanical Processing

When an ingot is formed, it can subsequently undergo thermomechanical processing for property modification and geometry shaping. As the starting feedstock for thermomechanical processes, the ingot is required to be homogeneous in chemistry, with a fine scale microstructure for ease of processing. Non-uniform properties may well lead to cracking during hot working.

Thermomechanical processes are carried out at temperatures above the brittle-to-ductile transition temperature (BDTT) to ensure adequate workability. For TiAl alloys, the working temperature must be above 700°C [2]. Thermomechanical processes can be characterised as primary and secondary steps. The primary step is to break down the coarse-grained microstructure into a fine-grained microstructure, and to be ready for the secondary hot working steps. Titanium aluminides possess a strong dependence of flow stress on strain-rate and temperature [2]. Therefore, the processing window in terms of strain rate, strain and temperature is narrow, particularly for thin section components as the heat loss is faster during hot working, and it is thus harder to maintain adequate workability.

The ingot feedstock can undergo several thermomechanical processing procedures. A good example is the production of TiAl exhaust valves, as shown in Figure 2-26 [10]. After an ingot is prepared from the VAR process, it is extruded to shrink the diameter into a thin TiAl bar. Prior to extrusion, the TiAl ingot is canned using mild steel, with a diffusion barrier between the can and TiAl. The extruded bar also has great potential for being applied as connecting rod and piston pins. It should be noted hot isostatic pressing is applied to the ingot prior to extrusion to reduce/eliminate any casting porosity and homogenise the chemistry [10].

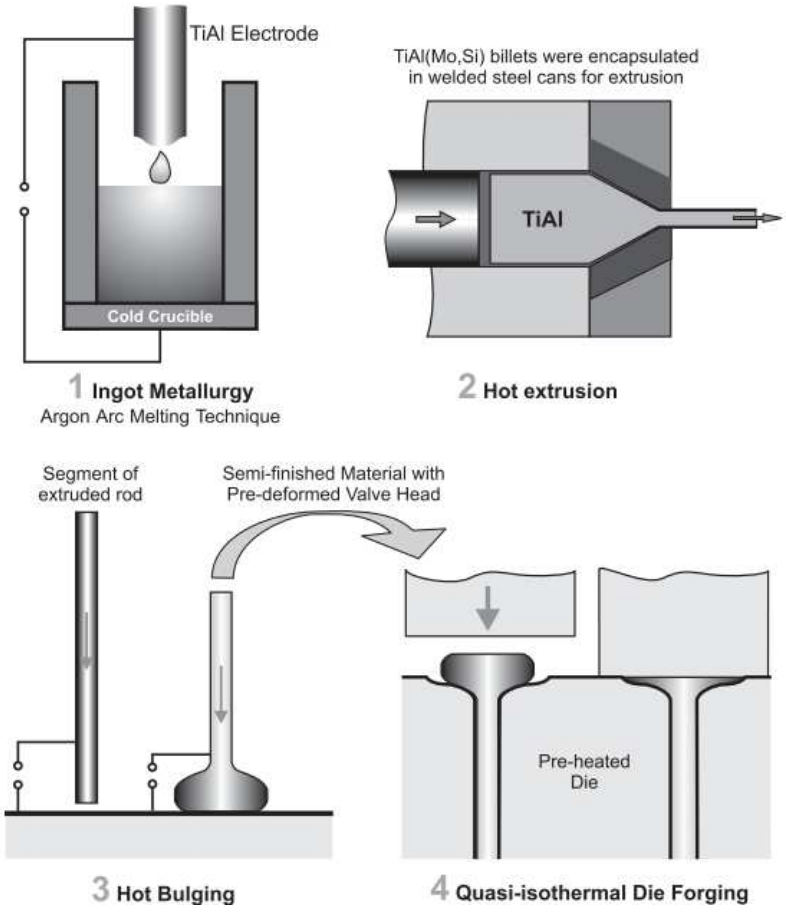

Figure 2-26. Production procedures of TiAl exhaust valve [10].

The extruded bar is then hot bulged and die forged (quasi-isothermally), to generate the final product dimensions. As mentioned earlier, the narrow window of TiAl thermomechanical processing increases the difficulty for TiAl hot working. Conventional forging, which employs relatively cold tools and high strain rates, is not suitable for the processing of TiAl alloys. Therefore, a modified strain rate and isothermal heated tooling are necessary for the majority of TiAl alloy forging processes.

2.4 Powder Metallurgy

2.4.1 Solid-state Sintering

Powder metallurgy is a process of forming components by heating (sintering) compacted powders. Various types of powder, such as ceramics and metals, in pre-alloyed or elemental forms, can be used, depending on the applications. Sintering is an atomic diffusion process occurring between powder particles. During heating, individual particles fuse together and the compact gradually acquires its strength and properties. A sintering practice is normally conducted at 75% (or higher) of the melting point of the material [21]. When the atoms receive adequate activation energy (usually thermal), mass transport events occur to reduce the system energy. From the atomic perspective, the surface curvature is associated with stress. A flat surface is assumed to be stress-free. Conversely, a convex surface is under tension, while a concave surface is under compression. Therefore, mass transport is caused by the stress exerted on the atoms at the surface until the difference among particles is balanced out (an 'ideal' flat surface) [22]. In the early sintering stage, neck formation is driven to eliminate the curvature gradients (surface energy). As the neck grows, the surface energy is gradually reduced until (about half of the initial surface area is lost) the driving force of mass flow shifts to elimination of the interfacial energy (i.e. grain and pore boundary) [22].

The atomic diffusion paths are described by surface or bulk mass transport mechanisms, depending on the source of the diffusing atoms (Figure 2-27). For atoms on the powder surface, they can diffuse through evaporation-condensation or via the surface or the bulk (volume) of the powder. While atoms in the bulk of the particle diffuse via grain boundaries, dislocation movement or the bulk of the powder. Surface transport contributes to neck growth but no shrinkage or densification as the atoms were already on the surface on the powder particles. In contrast, bulk transport leads to shrinkage and is the dominating mechanism at higher temperatures.

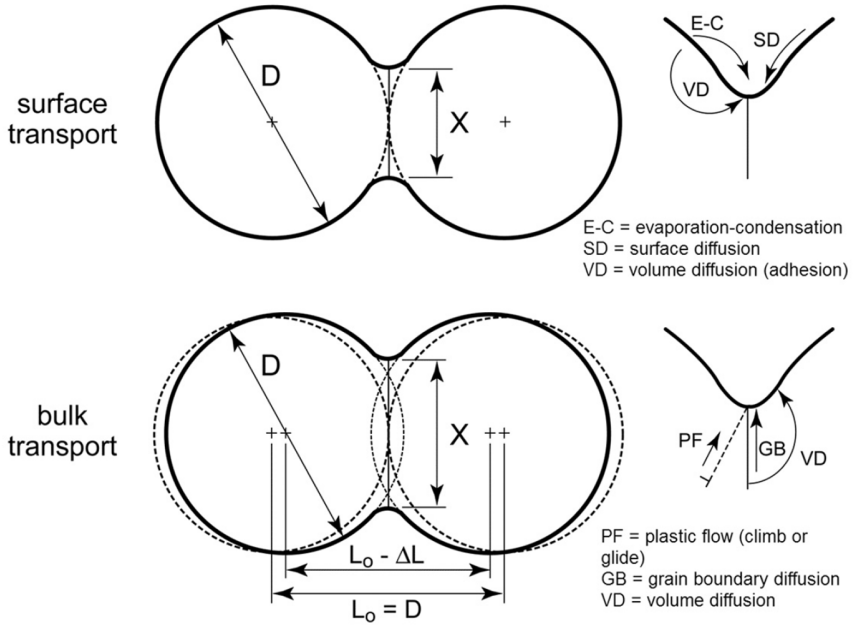

Figure 2-27. Mass tranpsort mechamisms, illustrating the diffusion routes of surface transport (evaporation-condensation, surface diffusion and volume diffusion) and bulk transport (plastic flow, grain boundary diffusion and volume diffusion) [22].

Figure 2-28 illustrates the four stages which the compacted powder undergoes through the sintering process. For the initial stage, the powder is 'loose', and the curvature gradients between particles are large. The main sintering driving force is surface area reduction, and neck formation is the results of this. The pores (empty space void) are irregular and angular in shape, and many of them are connected and open to the exterior of the compact (termed 'open porosity'). As the neck grows and develops in the intermediate stage (up to ~92% of theoretical density), the pores gradually close and become more rounded in shape [23]. At this stage, the powder particles have merged extensively, and the grains in the powder consequently grow as there are less diffusional obstacles from the pores.

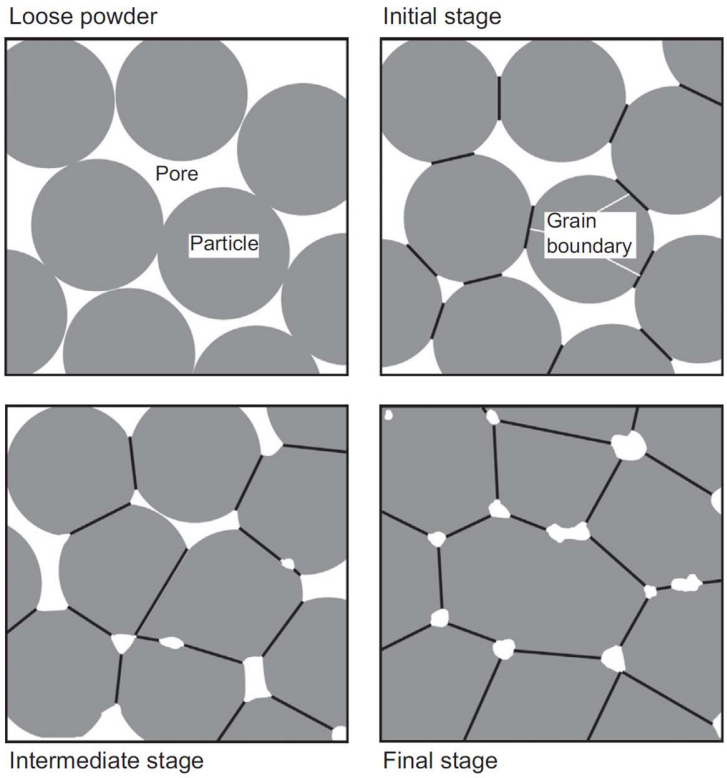

Figure 2-28. A conceptual schematic diagram illustrating the sintered geometry obtained at different sintering stages [22].

As the sintering process progresses into the final stage, the microstructural changes occur mostly in terms of the grain and pore structures (i.e. size and shape), and their locations. The grain growth is more significant and the shape gradually become polygonal (faceting), reflecting the compact grain coordination (a tetrakaidecahedron geometry if the 'ideal' scenario could arise) [22]. The pores are closed and nominally spherical, and they are mostly located at the grain boundaries. If there is gas trapped in the pores, pressure begins to build up and counteracts any further shrinkage as heating continues. In this case, prolonging sintering time will not improve densification but may cause sample expansion (over-sintering). Pores are not only closed and rounded, but they are also isolated or located on grain boundaries. In the final stage of sintering, the grains (or pores) progressively coarsen at the expanse of the smaller ones, resulting an increase in sizes but a reduction in quantity. Such phenomenon (phase coarsening) are described as 'Ostwald ripening' [24].

2.4.2 Transient and Persistent Liquid Phase Sintering

Liquid phase sintering (LPS) involves forming a liquid during the sintering cycle. Compared to a solid-state sintering event, the diffusional processes are facilitated when a liquid is presented in a LPS scenario. The LPS mechanism has been utilised in many material systems to improve sintering or even achieve full density, for example: TiC-Ni, Cu-Sn, Fe-Ti and Ni-Ti systems [25–28]. Figure 2-29 illustrates the densification mechanisms arising during LPS. An additive phase (liquid phase forming material) is mixed with the primary powder to generate the LPS processing at elevated temperature. When the liquid phase forms, the powders are wetted and rearranged, for a better packing density (rapid densification). Ideally, the liquid has a low solubility in the powder, but the powder has moderately high solubility in the liquid. Thus the powders partially dissolve into the liquid and the atoms can be transported around. The solubility of the solid grain depends on the grain size. Small grains have higher solubility, and thus particles dissolve in the liquid and precipitate onto the larger ones (solution/re-precipitation stage). In the case of transient LPS, the liquid phase gradually decreases as it was absorbed (reacted) by the solid powder until no liquid is left. The sintering then follows the solid-stage sintering mechanisms.

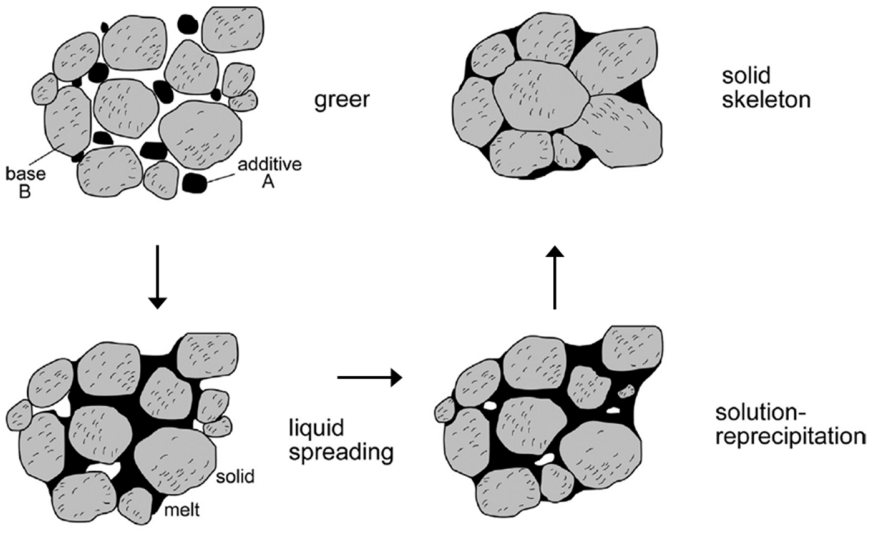

Figure 2-29. Liquid phase sintering stage, showing the microstructure change and densification mechanism (figure modified from [22]).

2.5 Spark Plasma Sintering

2.5.1 Introduction

The concept of using a current to assist a sintering process was introduced in the 1910s, and later several patents described methods of applying an electric discharge in sintering powders or sinter-joining materials [29,30]. However, the technique did not show much progress until the 1990s, after the technique was commercialised by Sumitomo Coal Mining Co, Ltd [31] as 'spark plasma sintering' (SPS). Since then, there has been a considerable growth in terms of research. The SPS technique offers unique advantages over other, more conventional, PM processes — pressure assisted sintering, fast heating and cooling rates, and field effects (discussed later). The process has been extensively applied to sinter various types of materials, particular difficult-to-sinter ceramics and composites, such as Al_2O_3 [32], WC [33] and SiC powders [34,35].

A typical SPS system consists of a power unit, hydraulic press, sintering chamber, vacuum and gas control systems, temperature monitoring device(s) (i.e. pyrometer and/or thermocouple), water cooling, and a computer control system. Figure 2-30 shows an SPS chamber and power supply unit, which is the basic model (Series 20, GA-Technologies) used in the present research (Chapter 6).

Figure 2-30. A typical SPS chamber and power unit (Series 20, GA-Technologies).

Graphite dies and punches are normally used to conduct current during sintering. To protect the die and punch surface, graphite foil is invariably used to cover the interior of the die to prevent direct contact with the powders. After the powder is loaded into the die, the assembly is moved to the chamber for sintering (Figure 2-31). The sintering process can be conducted under either vacuum or atmospheric conditions (e.g. Ar or N_2 gas). In the case of vacuum sintering, the chamber is filled with argon and then evacuated (ideally to a pressure less than 10^{-2} torr). This procedure is repeated if necessary to ensure no residual air in the chamber. The voltage and current are controlled by the computer to closely follow the desired heating and cooling rates. The temperature is monitored using a pyrometer or thermocouple. A pressure is simultaneously applied to the sample though the sintering process.

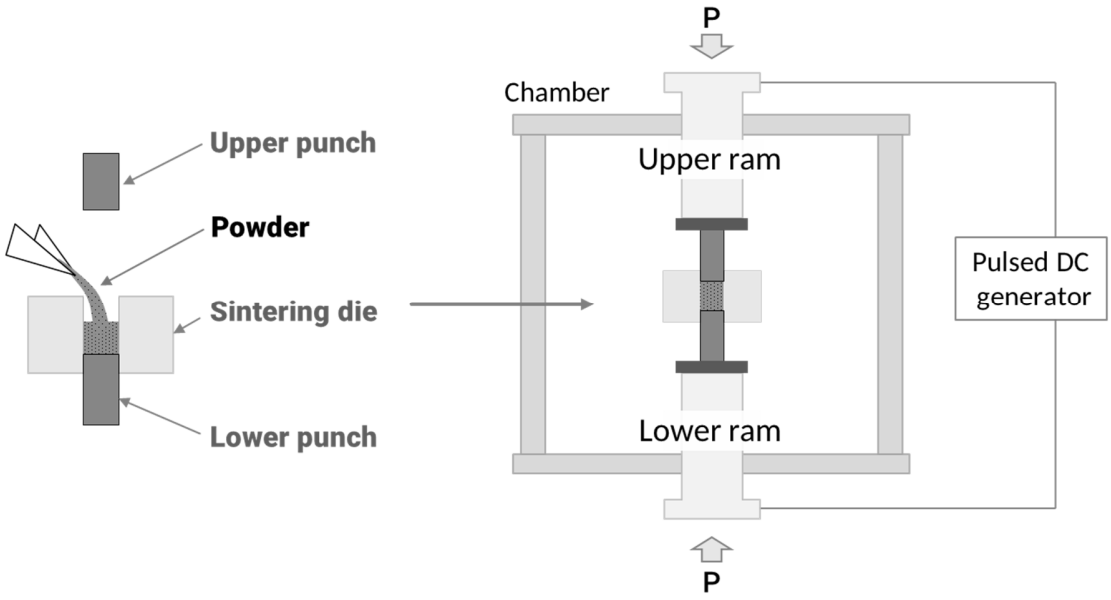

Figure 2-31. Schmatic diagrams of the die set and SPS chamber, illustrating the equipment setup.

2.5.2 Sintering Mechanisms

The SPS process is similar to hot pressing in many aspects. They both sinter powders with an assisted pressure and usually in a graphite die arrangement. However, the main difference is the heating source used. The hot pressing process utilises an external

resistance heater, which enclosures the chamber and radiates heat to sinter the materials. In addition, the heat can be transferred through convection if gas is present in the chamber. Consequently, the heating process is slow and some of the heat is lost in heating the environment.

In comparison, the SPS technique sinters powders using an electric current. For non-conductive materials (e.g. ceramics), when the current is applied, most of it will pass through the graphite die and Joule heating is generated. The powder is sintered by the heat generated within the die. For metallic or conductive powders, when the current passes through the powder, Joule heating is generated at the particle-particle contact regions, where the electrical resistance is the greatest (Figure 2-32). With adequate heat, localised melting or even vaporisation, which promotes diffusion considerably, may occur on the powder surface. When a spark discharge appears in the gap between particles, a plasma field (ionization of gas) is proposed to be created, momentarily, and further mass transport is facilitated as a result of 'spark impact pressure' [36].

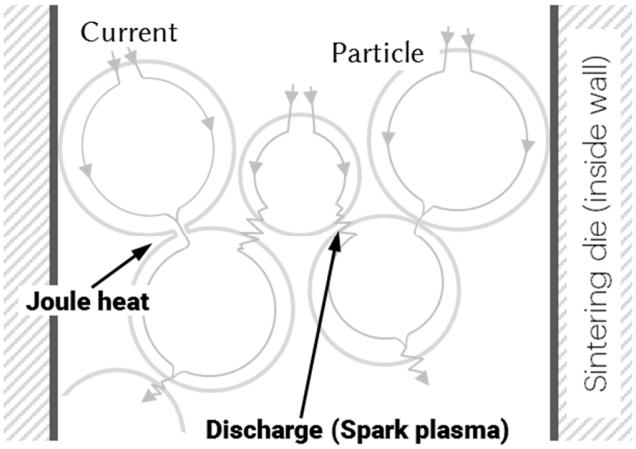

Figure 2-32 The Joule heating effect that occurs when the current passes through a conductive powder compact (figure adapted from [37]).

Moreover, the on-off pulsed current is speculated to 'clean' the powder, as the oxide layer(s), impurities or absorbed gases on the powder surfaces are melted and evaporated during current discharging [38,39]. Mizuguchi et al. has reported the cleaning effect when sintering ZrB_2 ceramic powders. Oxygen was not detected and other impurities (Cr, Fe and Hf) were lower at the grain-boundaries in the samples when compared to hot pressed counterparts [40].

However, there has been no clear direct evidence of the existence of either a spark or a plasma during the current discharge stage. Hulbert and colleagues used atomic emission spectroscopy (AES) and an ultrafast voltage monitor to observe sintering processes *in-situ* for several different powders, including conductive and non-conductive materials (Al, Al_2O_3, Mg and Zn), but no spark, arc or plasma was detected in the processes [41]. The reported cleaning effect has also been controversial. Besides the work from Hulbert *et al*., Collet and colleagues have reported that the cleaning effect was not observed, and the oxide on the atomised Cu powder surface was not reduced [42]. Because of the lack of evidence for spark plasma phenomenon, more recent studies have referred this technique by other names, such as field activated sintering technique (FAST) or pulse electric current sintering (PECS) [34,38,43]. Nevertheless, the designation 'spark plasma' has been widely used among researchers and for the commercial equipment units.

The high power pulsed current allows rapid heating rates, as high as 1000°C/min, depending on the electrical resistance of the material [38]. Consequently, the heating duration can be reduced considerably compared to other conventional heating approaches. The volumetric heat generation rate $\dot{q}$ is given by:

$$\dot{q} = JE \qquad \text{Eq. 2-5}$$

where J is the current density and E is the electric field [44]. The fast heating rate not only shortens the sintering time, but it can also alter the densification mechanism as the powder coarsening mechanisms (e.g. surface diffusion) at low temperatures are minimised, and the high-temperature densification mechanisms (i.e. grain and volume diffusion) are more favored [45]. Zhou et al. has reported a considerable improvement in density when sintering (1150°C) Al_2O_3 powder at a higher sintering rate (300°C/min vs. 50°C/min);

nevertheless, such effects are not always obvious at higher sintering temperatures [46]. Once the current is turned off, the cooling rate is also rapid and generally in the range of 150°C/min. With an active cooling system, the cooling rate can even be as fast as 400°C/min [38]. As a result, phenomena such as gain growth can potentially be suppressed in the SPS process, and fine microstructures can be retained in the material, particularly when sintering with a fine starting powder. For example, dense CeO_2 ceramic, with a fine grain size of 10-15 nm, can be produced when using a nanoscale starting powder (6-7 nm) [31].

Despite the efficient sintering possible with the SPS process, the temperature gradient can be significant. Olevsky et al. demonstrated large local temperature gradients can promote diffusion between powder contacts, and this has an influence on shrinkage and deformation during sintering [47]. Nevertheless, these gradients raise concerns regarding inhomogeneous properties in the final sintered material. In the case of a non-conductive powder, heat is mostly generated and conducted from the graphite die, and consequently the core of the sintered material may be less consolidated due to the possibility of a lower sintering temperature. The temperature difference between the powder and die surface increases with temperature. Moreover, sharp thermal gradients during cooling can cause localised high stresses and induce dislocations [40]. In both experimental and simulation results, the punches experience the highest temperatures, while the minimum is on the die outer surface [34].

The assisted pressure during the process also has significant influence in sintering. The pressure not only promotes a better contact between particles and enhances the existing densification mechanisms (i.e. grain boundary diffusion, lattice diffusion and viscous flow), but also introduces other densification mechanisms, such as particle sliding and rearrangement [44]. Xie et al. have observed that the pressure (plastic deformation) helps to break down the oxide film on Al particle surfaces and improves densification [48]. For nano-sized particles, which tend to agglomerate and lead to large sintered grains, high pressure (i.e. hundreds of MPa) can break down such undesired powder agglomeration during sintering [38]. However, the applied pressure will be limited by the high-temperature fracture strength of the pressing tool (e.g. for graphite, 100-150 MPa) [38].

In addition to the unique thermal effects, the electric current induces a concurrent electromagnetic field to the material. According to the electromigration theory, the effect of a field on mass transport can be expressed as:

$$J_i = -\frac{D_i C_i}{RT}\left[\frac{RT\partial lnC_i}{\partial x} + Fz^*E\right] \qquad \text{Eq. 2-6}$$

where J_i is the flux of the diffusing ith species, D_i is the diffusivity of the species, C is the concentration of the species, F is the Faraday's constant, z^* is the effective charge on the diffusing species, E is the field, R is the gas constant, and T is temperature [49]. With the presence of an electric field, changes in sintered properties have been reported in many different aspects. These include variations in the phase transformation response in alloys, plastic deformation in metals and ceramics, hardenability changes in steels, and microstructural developments (phase nucleation and growth) [43]. However, the voltages applied in SPS are generally low, and the effects of an electrical field can be difficult to observe [38]. In terms of the current effect mechanisms, it is generally believed that the electric field promotes mass transport during sintering. Kumar and colleagues have observed that an applied current could increase the concentration of vacancies in a Cu-Al alloy [50]. Munir and colleagues have reported that a higher current density increased the growth rate and shortened the incubation time for the nucleation of the Al-Au intermetallic layer in a metallic Al and Au bi-layer SPS experiment, regardless of the DC direction. Without an applied current, the layer was not measureable until after annealing for 20 hours [43]. On the other hand, it has also been shown that the imposition of a DC current increased the annealing rate of point defects, which was attributed to a decrease in the activation energy for mobility in a quenched Ni_3Ti alloy [51].

2.6 Summary

This chapter has provided the necessary background knowledge for the studies presented in the present thesis. To begin with, the fundamental properties of both materials were introduced, including their crystalline structures and physical properties. Ti- and TiAl-based alloys have shown their unique advantages, such as low densities and adequate strengths at high temperatures, combined with excellent corrosion and oxidation resistance. These characteristics are particularly important for the aerospace and automobile industries. Additional information on the TiAl alloy development, conventional fabrication methods, and their implementation in some specific aerospace and automobile applications provides the context of the current state for this intermetallic material. With this information, the research goals and difficulties in development of those alloys can be better perceived.

One essential property of Ti, including its alloys and related aluminides, is that they can be influenced by the elemental alloying additions and this results in significant transformations in microstructure and properties. The discussion of the alloying additions here is helpful in explaining the effects of these constituents on the sintered products in the subsequent chapters, although alloy development was not a specific focus in this thesis. The introduction to microstructural development at different processing temperatures (i.e. fully lamellar, duplex, dual-phased structure) offers basic knowledge when developing the reaction and transformation models in the later chapters. The sintering approaches used in the thesis, namely the pressureless 'press-and-sinter' and spark plasma sintering approaches, have also been presented in the literature review. Understanding the sintering mechanisms (i.e. solid-state sintering, liquid phase sintering and/or electric current sintering) allows us to better interpret and compare the acquired densification results.

Chapter 3. A Comparison of Ti-Ni and Ti-Sn Binary Alloys Processed Using Powder Metallurgy

(published in Materials Science and Engineering: A, September 2015)

Hung-Wei Liu, D. Paul Bishop and Kevin P. Plucknett*

Materials Engineering, Department of Process Engineering and Applied Science, Dalhousie University, 1360 Barrington St., Halifax, Nova Scotia, Canada

Abstract

The simple press-and-sinter powder metallurgical technique has provided an economical route for the manufacture of components from lightweight alloys, including titanium. However, the issue of residual porosity is limiting Ti alloy use in demanding applications. The presence of a liquid phase during sintering can potentially facilitate diffusion, leading to improved densification. In the present work a comparison of liquid phase sintering mechanisms is undertaken, with either persistent or transient liquid formation, for Ti-Ni and Ti-Sn alloys, respectively. Samples are produced using blended elemental powders, with up to 10 wt-% alloying addition, with compacts uniaxially pressed and sintered at 1200 to 1400 °C. The benefit of Ni addition is significant in terms of sintering, with close to full density (~99.5 % of theoretical) achieved for optimised conditions. Sn additions also exhibit a beneficial sintering response, particularly at lower temperatures (< 1250 °C) and for lower concentrations (i.e. 2.5 wt.%), with densities exceeding 98.5% of theoretical achieved under optimal conditions. The hardening effect is clear for both alloy groups compared to commercially pure-Ti, whereas there was generally an adverse effect on the tensile properties.

Keywords

Powder metallurgy, liquid phase sintering, Ostwald ripening, optical microscopy, scanning electron microscopy, titanium alloys.

*Contact: kevin.plucknett@dal.ca

3.1 Introduction

Commercially pure titanium (CP-Ti) exhibits excellent corrosion resistance properties and is widely applied in marine or chlorine containing environments, such as in reaction vessels and heat exchangers [1,52,53]. Compared to stainless steels or other corrosion resistant metals and alloys, CP-Ti also provides a high strength-to-weight ratio, and is consequently favourable for application as a structural material in environments with mass constraints.

Despite these outstanding characteristics, titanium and its alloys are considered to be expensive, due to the complicated metal extraction and manufacturing processes that are required. In addition to the raw materials expense, the manufacturing steps used generally account for up to 60% of the total component costs [54]. The conventional ingot metallurgical processing method includes melting-and-casting, forging or other thermal-mechanical process steps, and potentially a considerable amount of final machining, adding further fabrication expense [4].

Conversely, the powder metallurgical (PM) processing approach, which has gained considerable acceptance in the high volume processing of other light metals, such as aluminium [55], holds the potential to providing an economical processing route for CP-Ti and related alloys [56]. The near-net-shape PM approach maximises the material utilisation and reduces the need for using complex fabrication processes (e.g. vacuum-arc remelting and various hot working procedures) [4]. However, in order to achieve full densification, hot isostatic pressing (HIP) is generally necessary for titanium, which adds further expense. Typical press-and-sinter PM generally only achieves near fully dense components, even with optimised sintering treatments. Previous work has demonstrated densities of ~98 % of theoretical for CP-Ti, via a conventional press-and-sinter PM approach [57]. Residual porosity remains to be overcome to attain improved mechanical performance. In particular, the ductility suffers considerably from the presence of porosity.

To boost the sintering densification, alloy additions are sometimes introduced to generate a secondary liquid phase; for example adding Cu or Fe to Ti [58–61]. The presence of the liquid phase during sintering provides an effective diffusion route for mass transport.

Therefore, voids are ideally eliminated, with a reduced sintering time or lower temperature potentially offering equivalent densification levels. Depending on the alloying additions, a liquid phase may exist at the sintering temperature (i.e. persistent) or might only occur during the early diffusion stage at lower temperatures (i.e. transient).

For the Ti-Ni system, a persistent liquid phase is expected at some target sintering temperatures, based on the phase diagram (β+L) [62], and for blended elemental mixtures the heating process encounters several intermediate eutectic temperatures in the binary system (the lowest of these occurs at 942°C for Ti with 28 wt-% Ni (denoted as Ti-28Ni hereafter, unless otherwise specified). As can be anticipated, the liquid phase volume will therefore vary with both the Ni content and sintering temperature. Besides introducing liquid phase, Ni has been found to reduce the diffusion activation energy [63], and therefore has a high diffusivity in Ti-Ni alloys [61], which promotes greater inter-diffusion. Significant densification improvements have been confirmed in Ti-2Ni and Ti-5Ni (in at.%) alloys [63].

Conversely, there is no eutectic reaction in the Ti-Sn system. A transient liquid phase can be initially expected to be created from the low melting temperature Sn, which will then form a binary Ti-based solid solution, resulting in solid-state sintering at elevated temperature. Early research using sponge Ti powder has shown remarkable results arising from Sn additions. It was demonstrated that Sn (varied from 2.5 to 15 wt-%) improved both the compaction behaviour and the sintered density (which increased from 95.6 % up to 97.9%), with a concurrent small reduction in tensile elongation (decreasing from 20% to 14%) [64]. However, Hsu et al. have reported that Sn (<5 wt-%) in an as-cast Ti-Sn alloy noticeably improved both bending strength and modulus [65]. While PM studies of Sn additions in Ti have been relatively limited, generally demonstrating minimal benefits, Sn additions have been investigated for biomedical applications [66–68]. This is due to good biocompatibility as well as the ability to modify the modulus of cast titanium alloys (e.g. Ti-(Ta-Nb-Zr) [66,67] or Ti-Cu [68]), in order to avoid the ‘stress shielding’ caused by a high modulus difference between the popular Ti-6Al-4V implant material and human bone [69].

In the present work, the Ti-Ni and Ti-Sn titanium binary systems (both with up to 10 wt-% alloying addition) are evaluated and compared in terms of their benefits on the sintering response and the consequent mechanical properties, when following a conventional PM-based press-and-sinter processing route. Relatively fine Ti and alloying addition powders have been specifically chosen for this study, with the sizes selected to optimise particle packing during compaction (the sintering addition powders are approximately one third the diameter of the Ti powder).

3.2 Experimental Methods

The Ti used in the present research was a CP-grade HDH powder (-325 mesh, 99.5% purity), obtained from Alfa Aesar. The alloying Ni powder (type 123, 100% grade) was obtained from Vale Inco. The Sn powder (-325 mesh, 99.8% purity grade) was also obtained from Alfa Aesar. The individual particle size distributions of the as-received powders were determined using Malvern Master Particle Sizer 20600.

The binary Ti compositions were prepared by adding Ni or Sn powder, in various weight percentages, from 2.5 to 10 wt-%, to the HDH-Ti (balanced). In addition, a further 1.5 wt-% Licowax LC lubricant was also incorporated to ease the friction between die walls and particles during the compaction process. The powders were then blended using Turbula T2F for 30 minutes to provide a homogeneous mixture. The blended powders were uniaxially pressed into two sample geometries: (i) cylindrical discs of 15 mm diameter x ~7 mm thickness (~4 grams of powder) for sintering density measurements and microstructural evaluation, and (ii) rectangular bars of dimensions 12.8 x 12.8 x 76.5 mm (~41 grams of powder) for tensile test samples. Samples were uniaxially pressed in a floating tungsten carbide die at 300 MPa, using Instron hydraulic compaction press (Satec 5594-200HVL). In order to evaporate out the lubricant, the pressed compacts were initially heated in a tube furnace to 400°C, at a rate of 10 °C/min, and held at temperature for 30 min under constant nitrogen flow. After cooling, they were sintered in a high vacuum (10^{-5} torr) furnace (Materials Research Furnaces J-8x10-WM-1650-VG), with a hold time of 2 hours, at various temperatures ranging from 1100 to 1400°C. The nominal heating and cooling rates were both programmed at 10 °C/min, although a natural furnace cool occurred below ~400°C. A minimum of two samples were prepared for each geometry-composition-

temperature combination. The liquid phase quantity of the Ti-Ni binary system, for the sintering temperature range that was examined, was estimated through use of the commercial thermodynamics software package FactSage^{TM} 6.4.

Sample green densities were calculated geometrically from the compact dimensions and mass. The sintered densities were determined in accordance with the MPIF Standard 42 (ASTM Standard B328). Selected samples were subsequently sectioned and cold mounted in resin. The surface was initially ground using 500 grit SiC paper, followed by polishing with 9 and 3μm diamond particle suspensions, and then finally with a colloidal silica suspension (0.05 μm). The polished samples were subsequently etched using a modified Kroll's solution. Microstructures were characterised with Olympus BX-51 optical microscope (OM) and Hitachi S-4700 scanning electron microscope (SEM). The SEM was equipped with Oxford Instruments energy dispersive X-ray spectroscopy detector (EDS) to identify sample chemistry. The sample pore size distributions were determined by image analysis (Media Cybernetics Image-Pro 6.3) of the OM micrographs. Individual pore size was determined from the Feret diameter measurement. The size data compiled for statistics consisted of between 1000 and 5000 individual pore measurements for each individual sample. Crystalline phase compositions were identified using Bruker D8 Advance X-ray diffraction.

Cylindrical 'button end' tensile samples were machined from the rectangular bars after sintering. Tensile property evaluation was performed using Instron hydraulic test system (Satec 5594-200HVL) equipped with a 50kN load cell. Strain was measured with a clip-on extensometer (Epsilon 3542) that remained attached to the sample through the point of fracture. As such, the reported strains to failure represent the sum of the elastic and plastic components. A minimum of two samples were tested for each composition-temperature combination. The hardness of sintered samples was evaluated using Rockwell indentation testing (Leco R-660), with measurements made within the Rockwell 'A' scale. Each hardness value is the average of four indentation tests.

3.3 Results and Discussion

3.3.1 Liquid Phase Volume Prediction

One fundamental difference between the Ti-Ni and Ti-Sn systems relates to their liquid phase forming mechanisms during sintering. As highlighted in Figure 3-1, the Ti-Ni system experiences the presence of a *persistent* liquid phase in the two-phase region (β + L), and potentially transient liquids will also form at some eutectic temperatures (i.e. Ni_3Ti (1304°C), TiNi (1118°C), and Ti_2Ni (942°C)) during the initial reaction stages of the blended elemental powders. The composition-temperature grid in Figure 3-1(a) indicates the projected sintering conditions for samples in the present work. In comparison, for the Ti-Sn system, the only (transient) liquid phase expected is as a result of the Sn melting when the temperature exceeds 232°C. The transient liquid will not exist long as the melt will be absorbed into a Ti-based solid solution (Figure 3-1(b)).

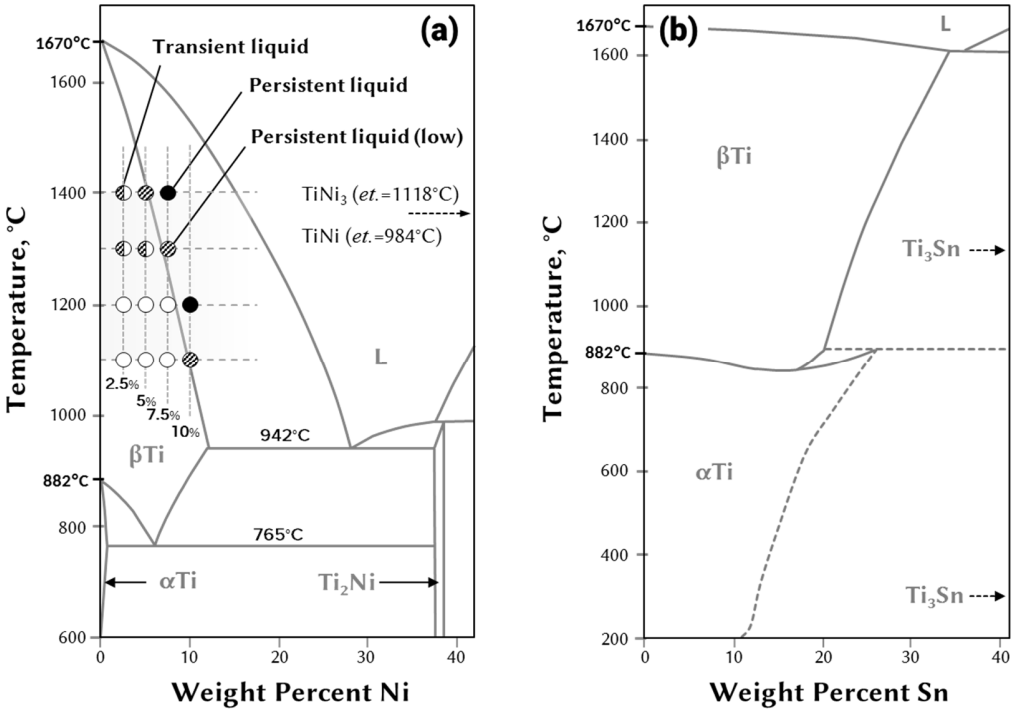

Figure 3-1. (a) Prediction of the Ti-Ni liquid phase type and amount, based on the Ti-Ni binary phase diagram (Ti-rich portion). (b) The Ti-Sn binary phase diagram (Ti-rich portion). The diagrams are adapted from ASM handbook.

Using the FactSage™ thermodynamics software, the anticipated Ti-Ni liquid phase content was calculated (under vacuum), as shown in Figure 3-2. Please note that the calculation was also performed for Ti-Sn alloys, but no liquid was expected. The estimation of the onset temperature and quantity of the liquid formation for each Ni-Ti composition generally matches the phase diagram shown in Figure 3-1(a). A significant liquid volume can be generated in the 7.5 wt-% Ni alloy at the higher temperatures, and this liquid phase would therefore be expected to benefit the densification stages. On the other hand, no liquid phase was predicted throughout the examined sintering temperature range for Ti-2.5Ni. However the simulation was based on equilibrium conditions and the localised *in-situ* liquid amount during the early stages of sintering was not determined; in this instance liquid arises from the likely transient presence of Ti-Ni intermetallic phases, as noted earlier. The intermediate stages of reactions between elemental Ti and Ni have been thoroughly assessed for a nominally 50:50 at.% mixture [70]. Complex, Ti core regions develop, with successive concentric rings of intermetallics decreasing in Ti content (i.e. in the order of: Ti_2Ni, TiNi, and Ni_3Ti). Clearly the Ni content in the present materials is significantly lower, however the same sequence of intermediate phases (thus liquid formation of each stage) can be anticipated when transitioning from elemental Ti and Ni through to the equilibrium final phase assembly.

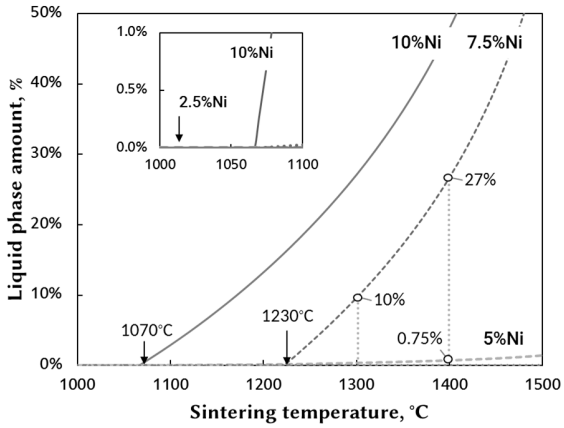

Figure 3-2. Projected liquid phase content of the Ti-Ni alloys at various sintering temperatures, predicted using the FactSage™ software.

3.3.2 Powder Compaction Behaviour

The initial particle size distributions for the Ti, Ni and Sn starting powders are shown in Figure 3-3. The size difference between the base Ti ($D_{50} \approx 25\mu m$) and the two alloying elements (both with a $D_{50} \approx 10\mu m$) was initially expected to contribute to slightly better packing than mono-sized powders (i.e. a higher green density), and hence improved particle-particle contact for better sintering. Moreover, the Ni and Sn powders are very close in terms of their respective particle size distributions, and consequently any size factor differences are minimised when comparing the two binary systems. Figure 3-4 shows the compaction response of each blend composition in terms of the measured green density. These values are broadly similar to prior work on Ti-Ni and Ti-Ni-Sn PM systems [28,61,71–73], although a slightly higher compaction pressure of 400 MPa was used in those studies, along with more coarse initial elemental powder sizes. The addition of Sn improves the green density when higher contents are used (i.e. 5 wt-% and above), likely as a result of its ductile nature. Conversely, the harder Ni additions impose certain constraint to the degree of compaction that can be achieved, and the green densities are consistently lower than the CP-Ti baseline; this can be viewed as being somewhat unfavourable in terms of a PM-based process. In addition, as shown in Figure 3-5, the significantly rougher surfaces of the Ni particles, compared to the smooth Sn particles, may further reduce the packing efficiency and thus lower the green density.

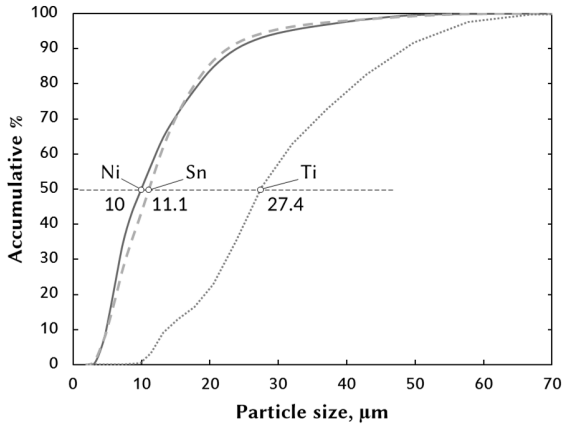

Figure 3-3. Particle size distributions for the initial Ti, Ni and Sn elemental powders.

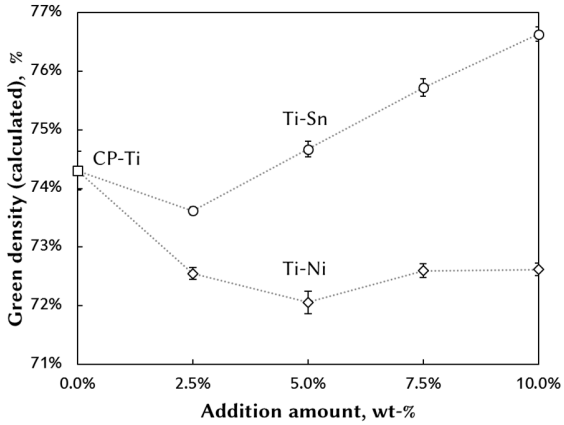

Figure 3-4. The measured green densities (from dimensional calculations) of unalloyed CP-Ti, and the Ti-Sn and Ti-Ni binary compacts.

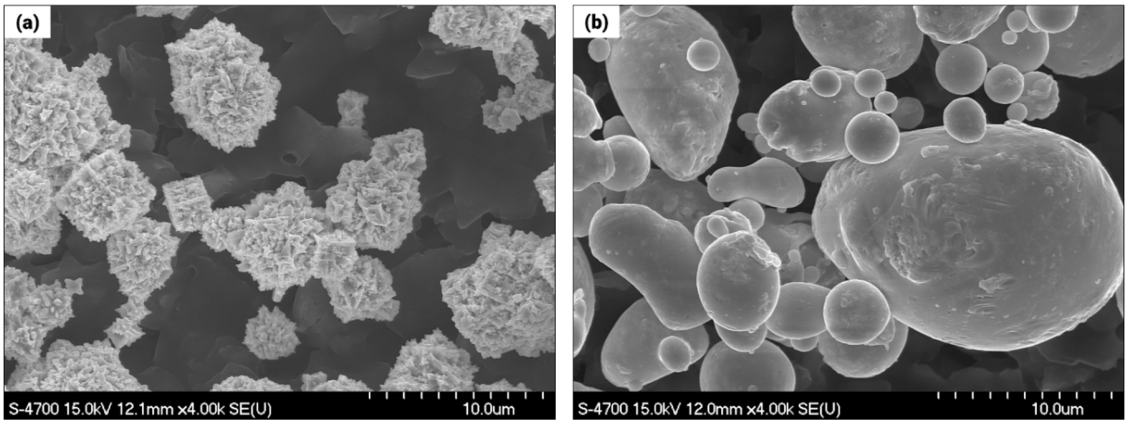

Figure 3-5. Representative SEM images of the morphology of the additive powders: (a) Ni and (b) Sn.

3.3.3 Densification and Microstructure

3.3.3.1 Ni addition

Sintering temperature and composition

The influence of sintering temperature on the final density of the Ti-Ni alloys is shown in Figure 3-6. The benefit of Ni alloying upon the densification response is clearly evident when compared to the non-alloyed CP-Ti, for all sintering temperatures examined.

For the 5 and 7.5 wt-% Ni samples, the densities peak at 1300°C, and then decrease slightly at 1400°C, indicating a degree of 'over-sintering' at this temperature. Under this condition (1300°C) each of the samples exceeds 98% of the theoretical density; the 7.5 wt-% Ni sample actually attains ~99.5% of theoretical. Conversely, the 2.5 wt-% Ni samples continue to exhibit densification up to 1400°C. Subsequent pore size distribution analysis (discussed in Section 3.4), which indicates the sintering level, reveals that any residual pores continued to shrink with increasing temperature in the 2.5 and 5 wt-% Ni samples, while in the Ti-7.5Ni samples the pores had reached the final-stage of sintering at 1400°C, as pore Ostwald ripening had begun to occur. Swelling can happen in the final-stages if gas was entrapped in the closed pores (gas expansion with increasing temperature), and this potentially generates the observed small decrease in density for the 7.5 wt-% Ni samples.

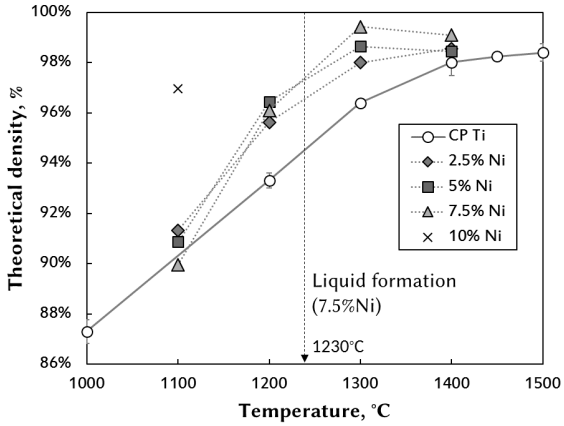

Figure 3-6. Sintered density of Ti-Ni samples sintered from 1100°C to 1400°C, with CP-Ti data as baseline values.

Before the predicted persistent liquid formation at 1230°C, utilising a higher Ni (except for 10 wt-% Ni) content does not present any clear advantage. Although the Ti-10Ni samples sintered at 1200°C have achieved high density, the high liquid volume present also results in shape distortion of the samples and adhesion to the support crucible (although swelling was not observed). Consequently, Ti-Ni samples with such a high Ni content were not evaluated further in the present study. Some benefits may potentially be

seen with these higher Ni contents for sintering temperatures below 1100°C, although these experiments were beyond the scope of the current work.

Powder size

In contrast to the present observations, Robertson and Schaffer reported a pronounced swelling phenomenon for Ti-Ni PM samples when sintering at temperatures above the β-Ti solidus [28,72,73]. In this case, swelling was suspected to be the result of rigorous gas release, either residual hydrogen or chlorine (chloride contaminants) from the HDH-Ti powders used [28,72]. Although the formation of liquid boosted the densification as anticipated, the rapid densification also eliminated the open porosity. Without the open porosity, which served as an outlet for gas releasing, the gas was trapped in the voids where liquid had flowed away. As sintering temperature increased, the gas pressure built up and offset the shrinkage resulted from LPS. High compaction pressure was also able to close the open porosity (when green density is > 90% of theoretical) and consequently similar swelling responses were reported as well [72]. Corbin and colleagues also highlighted a somewhat different swelling phenomenon when processing NiTi (with a nominally 50:50 at-% ratio) through a PM-based approach, which was largely attributed to a combustion reaction [74,75]. It was shown through detailed DSC and microstructural studies that reducing the Ni particle size, from 90 μm down to 1.2 μm, significantly reduced the amount of β-Ti formed during sintering, which dramatically lowered both the extent of the combustion reaction and also the degree of swelling.

The current study uses a broadly similar HDH Ti powder type to the prior work of Robertson and Schaffer [28,72,73], and might also suffer from gas release. However, if it occurs at all with the present raw materials, it is to a dramatically lesser degree than in the previous studies, potentially only occurring to a minor extent for some Ti-Ni samples sintered at 1400°C. One essential difference in the present study is the finer powder size used, with a diameter approximately one third of those used in the previous studies [28,72,73]. Larger powder size of both Ti and the alloying Ni appeared to form considerable amount of liquid and resulted in prompt shrinkage (observed from dilatometry)

[72]. Such rapid shrinkage, as pointed out earlier, may block the open porosity before the gas had released completely. In contrast, fine powders will not likely generate a sudden amount of liquid and cause the same response. Nevertheless a detailed dilatometry analysis is required to confirm the sintering response of the fine powders. Panagrahi used similar sized powders as the present work and was able to sinter Ti-2Ni and Ti-5Ni (in at.%) compositions without swelling, even under conditions of persistent liquid being present [63].

Localised liquid

As demonstrated in Figure 3-2, under *equilibrium* conditions there is no liquid phase predicted to form before 1230°C, except for compositions with the highest Ni contents (i.e. 10 wt-% Ni). Nonetheless, the clear increases in density at 1200°C, and to a lesser extent at 1100°C, may be contributed from the presence of intermediate phases and related localised liquid formation. However, it is also important to remember that sintering occurs between a binary blend of elemental Ti and Ni, and localised liquid formation can occur at 942°C, as confirmed in prior DSC studies of Ti-Ni mixtures [70,74,75]. Potential liquid formation at such temperatures in a comparatively dilute Ti-Ni elemental system will, of course, be more localised. It can also be expected that the use of fine Ni will also minimise the potential for liquid generation at such temperatures, following prior studies [74,75].

Microstructure

The sintering temperature also significantly affects the microstructure of the Ti-Ni alloys. Figure 3-7 illustrates the microstructural evolution observed for each of the examined compositions and sintering temperatures (excluding Ti-10Ni). The high densities that can be achieved using Ni additions are also confirmed in these images. The most distinct phase present in these microstructures is the light contrast region (identified as primary α-Ti), which exhibits an equiaxed or acicular morphology. In between the primary α phase areas, there are eutectic regions (dark contrast), consisting of alternating α-Ti and

Ti_2Ni phases. Samples sintered at higher temperatures generate larger (i.e. longer) α-Ti phase particles, as shown in Figure 3-7. This growth arises because as the temperature cools down to the α/β transition (< 882°C), the α-Ti (primary) nucleates initially at the prior β grain boundaries, and grows preferably on the {110} planes until it reaches another α-phase particle, which then presents growth constraint. Therefore, the size of the β-Ti particles formed during sintering confines the available space for the α-Ti to grow. If no obstacle is blocking expansion, the α phase will continue to grow in the same direction into longer needles or plates from the β grain boundaries.

The amount of α phase present will, in part, be controlled by the Ni concentration, based on the Ti-Ni phase diagram (Figure 3-1(a)). With more Ni addition there is less α-Ti phase present and instead there is an increase in the Ti_2Ni phase content. Measurement of the α-Ti phase area ratio (Figure 3-8), through image analysis of the optical micrographs, clearly indicates that the amount of α-Ti (primary) phase depends on the Ni content, and is generally unaffected by the temperature.

The microstructure of a representative Ti-Ni sample is highlighted in the SEM micrograph shown in Figure 3-9(a), together with the associated EDS map for this region (Figure 3-9(b)). From this information, individual phases are determined: (i) area #1 is the α-Ti phase, (ii) area #2 is the Ti_2Ni phase, and (iii) area #3 is the characteristic eutectic mixture (α-Ti + Ti_2Ni). While area #4 is also determined to be essentially pure Ti, it is believed to be the cubic β-Ti phase, based on the volume content; this is supported by the fact that some peaks of retained β phase were detected via XRD analysis (not shown).

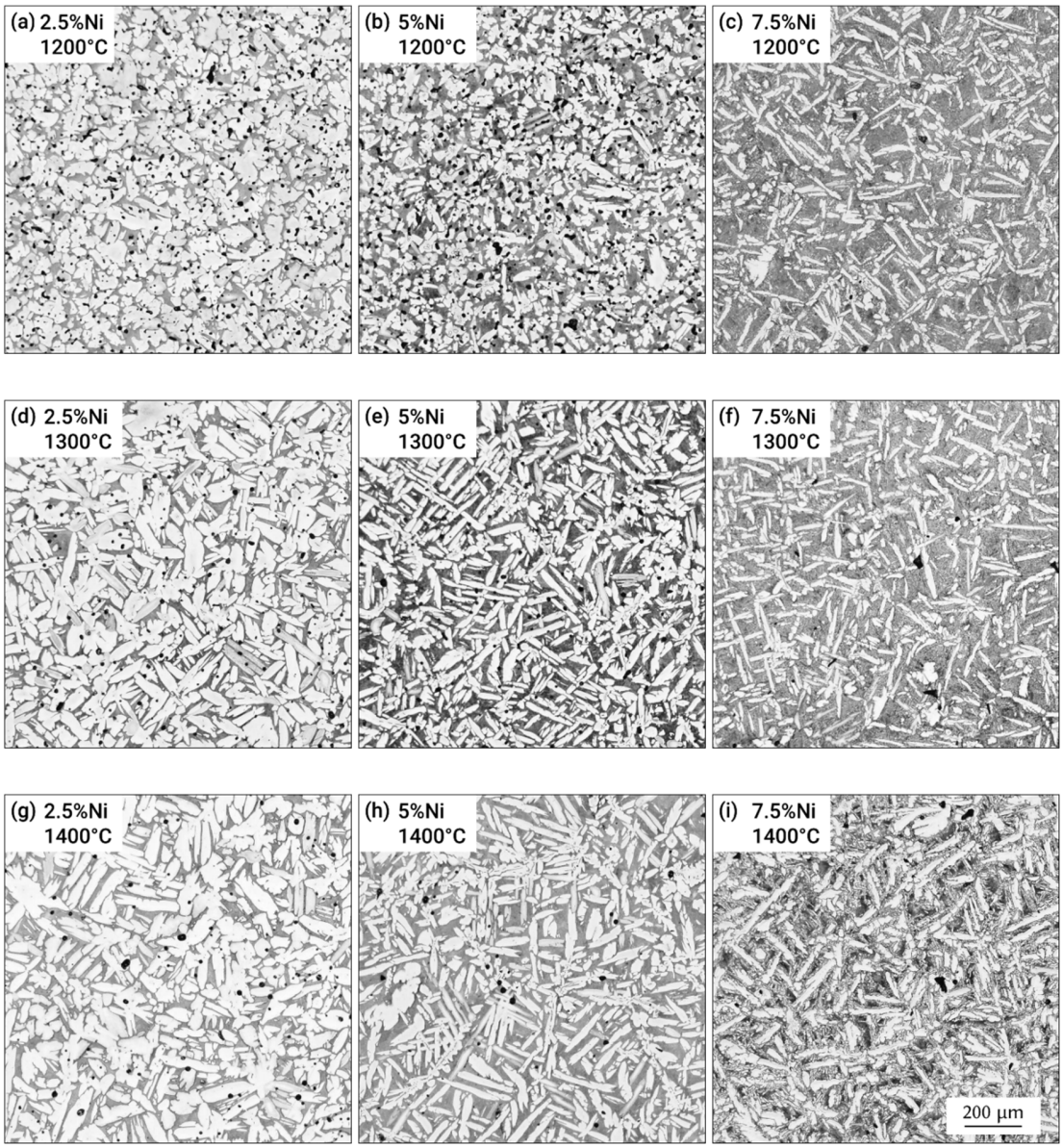

Figure 3-7. Optical micrographs of Ti-Ni samples with 2.5 to 7.5wt-% Ni, sintered at temperatures from 1200°C to 1400°C. All images are recorded at the same magnification.

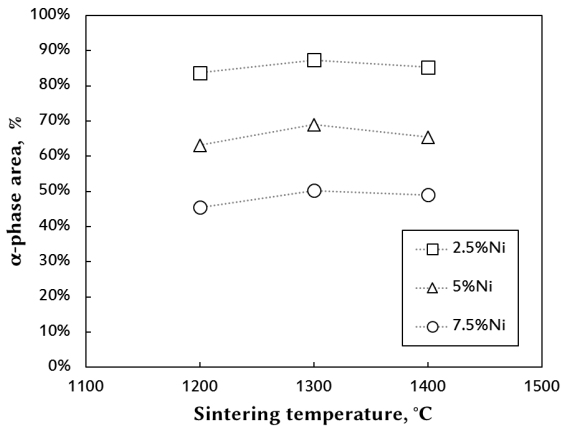

Figure 3-8. Primary α-phase area percentage in the Ti-Ni samples, as a function of Ni content and sintering temperature.

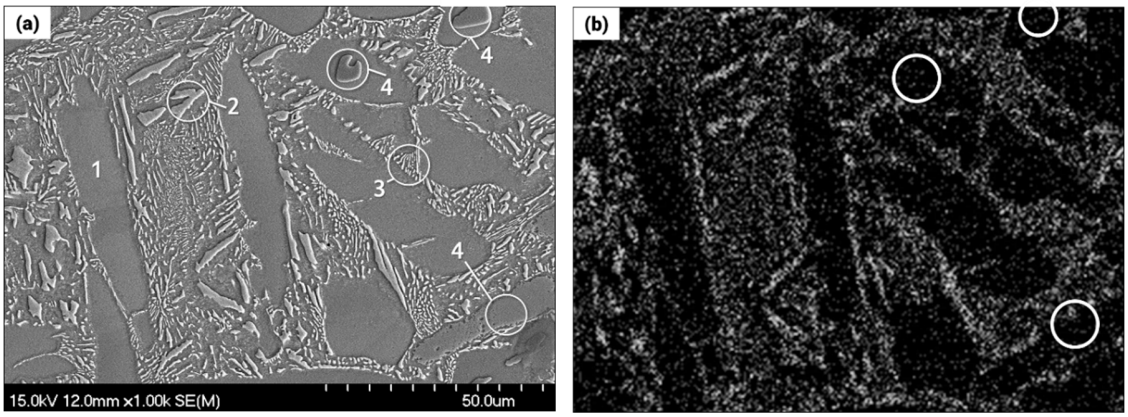

Figure 3-9. SEM micrographs of: (a) Ti-7.5wt-% Ni sintered at 1200ºC, and (b) the Ni elemental distribution in the same region as (a).

3.3.3.2 Sn addition

Sintering temperature and composition

In terms of the Ti-Sn binary compositions, the sintering temperature used appears to cause mixed effects for the resultant density, when compared to the CP-Ti data. Figure 10 highlights the results in two temperature regimes, either sintering below or above 1250°C. Although the Sn elemental powder melts during heating, and may provide a fast

diffusion route, the liquid phase only exists briefly before being absorbed into solid solution by the surrounding Ti particles. The transient melt may leave a porous skeletal structure, as capillarity wicks away the molten Sn, which will hinder the subsequent densification as more solid-state mass transport is required to fill the residual void space [59]. In this instance it is therefore preferable to minimise the Sn particle size during processing. In fact, all Ti-Sn samples were susceptible to this issue. The density improvement when sintering in the lower temperature range (i.e. below 1250°C) is more likely due to the higher green densities of the compacts [61]. In this case the density gain surpasses the loss from the skeleton expansion. However, when the sintering temperature is above 1250°C, the Sn additions appear to impede the samples from further densification. As the porosity analysis will discuss later, above 1250°C it is suggested that the sintering process had entered the final-stage. Any gas trapped in the voids from the transit liquid phase may then counteract densification by increasing volume expansion with temperature.

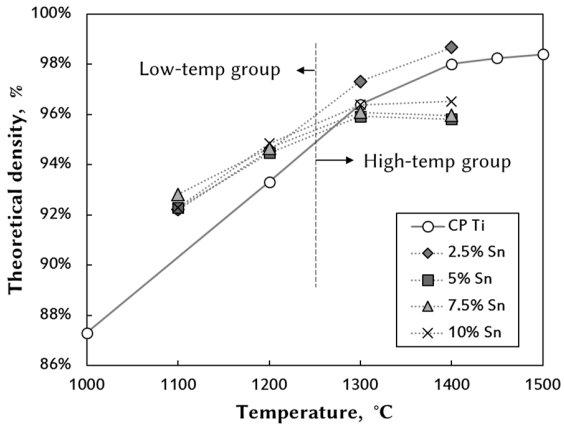

Figure 3-10. The density of Ti-Sn samples sintered at temperatures between 1100°C to 1400°C, as a function of Sn content. Data for CP-Ti is also shown as a baseline measure.

Furthermore, the effects of different Sn contents are somewhat limited. The variation in Sn level appears to exhibit no significant effect in terms of composition or sintering temperature. The one apparent exception in this instance is the lowest Sn content

sample (i.e. Ti-2.5Sn), which deviates from the other compositions, and demonstrates a continuing improvement in the densification with increasing temperature. This phenomenon indicates that the 2.5 wt-% Sn samples, while benefiting from the density increase at all temperatures, are not significantly affected by the generation of a skeleton structure and/or gas expansion. Contrary to the case of Ni additions, which should be kept below 7.5 wt-% to maintain dimensional stability, the addition of Sn does not cause any issue in terms of sample distortion during sintering for the evaluated compositional range (up to 10 wt-%).

Microstructure

The phase transformation response for the Ti-Sn alloys undergoes broadly similar metallurgical mechanisms as for the Ti-Ni alloys. However, all of the examined compositions will be single phase under equilibrium conditions, based on the phase diagram (Figure 3-1(b)). It was noted that grain boundary details were difficult to reveal by etching and polarised light imaging. In general, the microstructure is comprised of nominally equiaxial grains when sintered at low temperature, as shown in Figure 3-11(a). The morphology of these grains then transforms into one of elongated rods at the highest sintering temperature (Figure 3-11 (b)). Contrary to the behaviour with Ni elemental additions, the Sn content does not interfere with the α phase ratio because Ti-Sn is a single-phase alloy. Consequently, the sintering temperature, which controls the β grain size, is the determinant factor in the resultant α-Ti grain structures. Any potential influence of the cooling rate on microstructural development was not considered in the current work, as the nominal rate as maintained at 10 °C/min for all samples.

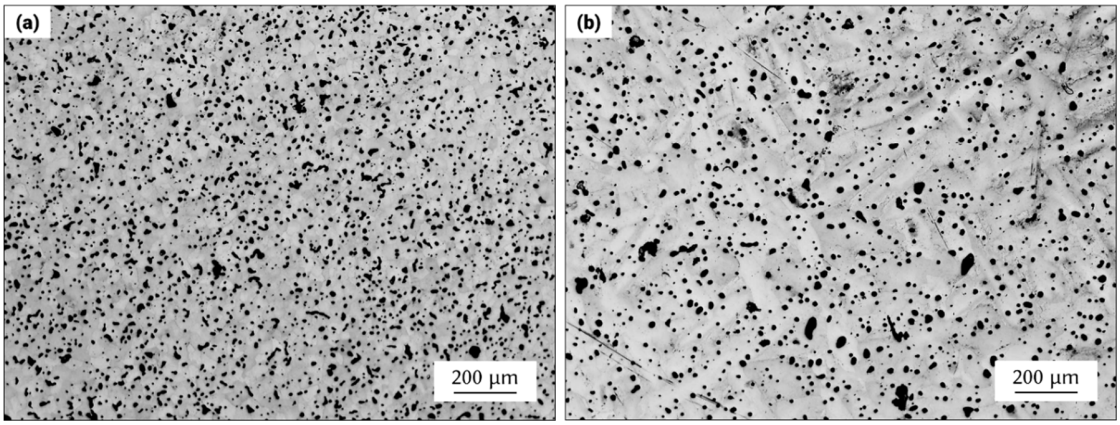

Figure 3-11. Polarised light optical micrographs of Ti-7.5%Sn samples, sintered at: (a) 1200ºC, and (b) 1400ºC.

3.4 Porosity Evolution

As noted earlier, to a certain extent the degree of sintering (in terms of the mechanistic stages) can be revealed from an analysis of the porosity size distribution, presented in Figure 3-12. For both the Ti-2.5Ni and Ti-5Ni compositions, there is a transition in the pore size distribution to a finer range with rising temperature (Figure 3-12(a) and (b)). From the sintering perspective, those samples have not reached the final-stage of sintering, and there is still opportunity for densification. The appearance of Ostwald ripening occurs when the Ni content is further increased (i.e. Ti-7.5Ni), as shown in Figure 3-12(c). From another perspective, when comparing the Ti-Ni samples sintered at the same temperatures, for example at 1200°C, an increased Ni content promotes the pore evolution sequence, owing to the higher liquid phase volume generated.

In contrast, the behaviour of the Ti-Sn alloys was relatively straightforward. When the sintering temperature increases, the pore size distribution of each composition moves towards larger sizes (i.e. coarsening) at the expense of small pores, with the observation that the primary distribution peak decreases in height. As a result, the *mean* pore size increases, while at the same time the *total* porosity volume decreases, as evidenced by the previously discussed densification data (Figure 3-10). Such a pore size evolution matches the typical Ostwald ripening mechanism, and denotes the sintering process is entering the

final-stage, in which all pressureless mechanisms of pore shrinkage have essentially been completed.

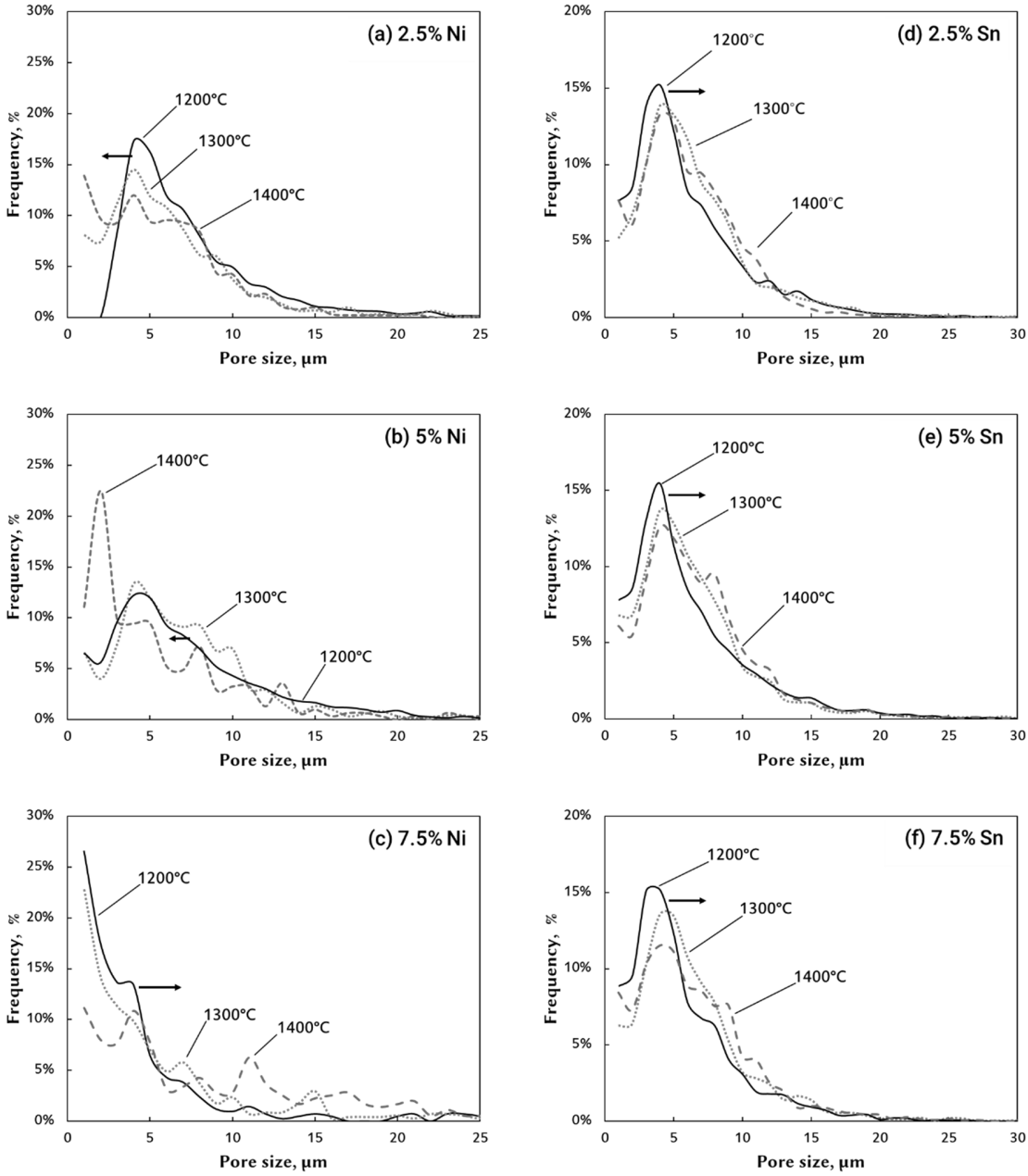

Figure 3-12. The effects of composition and sintering temperature on the pore size distribution and evolution for the Ti-Ni (a-c) and Ti-Sn (e-f) binary samples.

3.5 Mechanical Properties

3.5.1 Hardness

The Rockwell hardness measurements (HRA scale) for both of binary alloy systems are presented in Figure 3-13. For the Ti-Ni samples, the hardness generally matches the trend observed with respect to their densification response, as a function of temperature. The hardening effect from the Ni addition is evidently positive. Besides the occurrence of solid solution strengthening, an intermetallic Ti_2Ni phase is forming with higher Ni content, which is expected to affect the material hardness; a value of HRA 81 has been reported for a Ti_2Ni-TiNi composite system [76]. It is notable that the hardness decreases for the Ti-7.5Ni sample, sintered at 1400°C. This is believed to arise as the porosity evolution mechanism changes, with the occurrence of pore ripening (i.e. coarsening) at the higher temperature. It is interesting to note that the Ti-10Ni sample sintered at 1100°C exhibits relatively good hardness, in accordance with its comparatively high density.

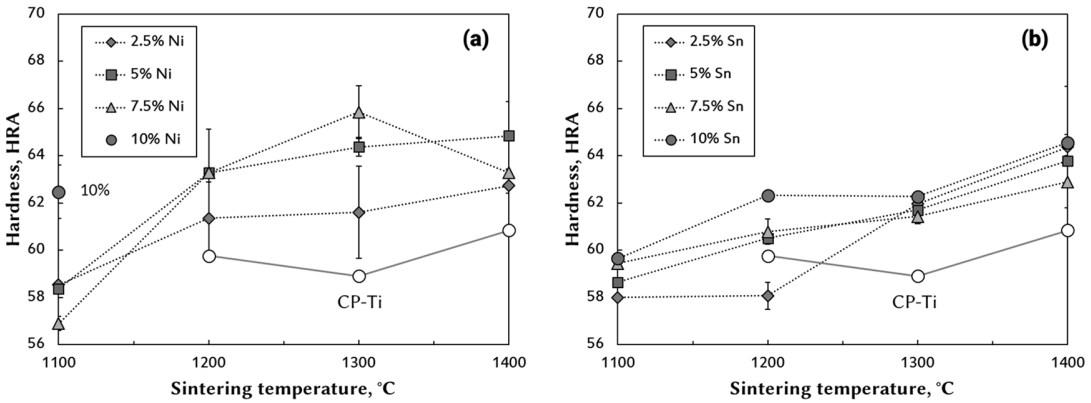

Figure 3-13. The measured Rockwell hardness (HRA) of the binary PM samples: (a) Ti-Ni, and (b) Ti-Sn.

On the other hand, the Ti-Sn alloys exhibit a more linear trend in terms of the hardness evolution, with lesser fluctuation between compositions. Despite having lower sintered densities when compared to the CP-Ti samples processed at temperatures above 1200°C, the strengthening effect of low Sn contents are clear, although progressively

higher Sn levels appear to be only slightly beneficial in terms of further hardness improvements. The strengthening effects from Sn are less significant than Ni, as no secondary hard intermetallic phase is introduced (versus Ti_2Ni formation in the Ti-Ni system). In support of this, the XRD analysis did not detect any Sn-related phases, confirming a single-phase α-Ti microstructure (i.e. Sn present in solid solution) in these samples. Each of the Ti-Sn samples examined was generally harder than the non-alloyed CP-Ti, although the densities are somewhat lower than the CP-Ti in the high temperature group (Figure 3-10).

3.5.2 Tensile Properties

As mentioned earlier, distortion and crucible adhesion occurred in the Ti-10Ni composition when sintering at 1200°C. Therefore, for the purpose of comparison between the two binary systems, only samples with up to 7.5 wt-% additions were prepared for the tensile tests. For the Ti-Ni samples, there was significant variation in the results (Figure 3-14), and it is difficult to draw clear conclusions. Most of the tensile properties of the Ti-Ni materials are lower than those recorded for the CP-Ti samples, with the exception of the elastic modulus values, which are scattered around the CP-Ti results. The 7.5 wt-% Ni samples have the lowest yield strength, fracture strength and ductility. The low ductility has caused premature failure and therefore the 7.5 wt-% Ni materials performed poorly. These samples have the highest content of the brittle intermetallic, Ti_2Ni, which may in part be responsible for this degradation in tensile response. The 5 wt-% Ni samples sintered at 1300°C had outperformed the other Ti-Ni compositions and CP-Ti in elastic modulus, yield strength and fracture strength, and hence achieves the peak condition for tensile properties for the Ti-Ni binary materials that were examined. A similar observation for CP-Ti, reported previously [57], also noted that CP-Ti samples sintered at 1300°C had reached an optimal configuration of grain size, pore size and pore concentration; in this instance sintering at a higher temperature also resulted in property degradation. It was also shown that the Ti HDH used in both that study and the present work has a higher oxygen content than ideal [57], which is also potentially contributing to the low ductility.

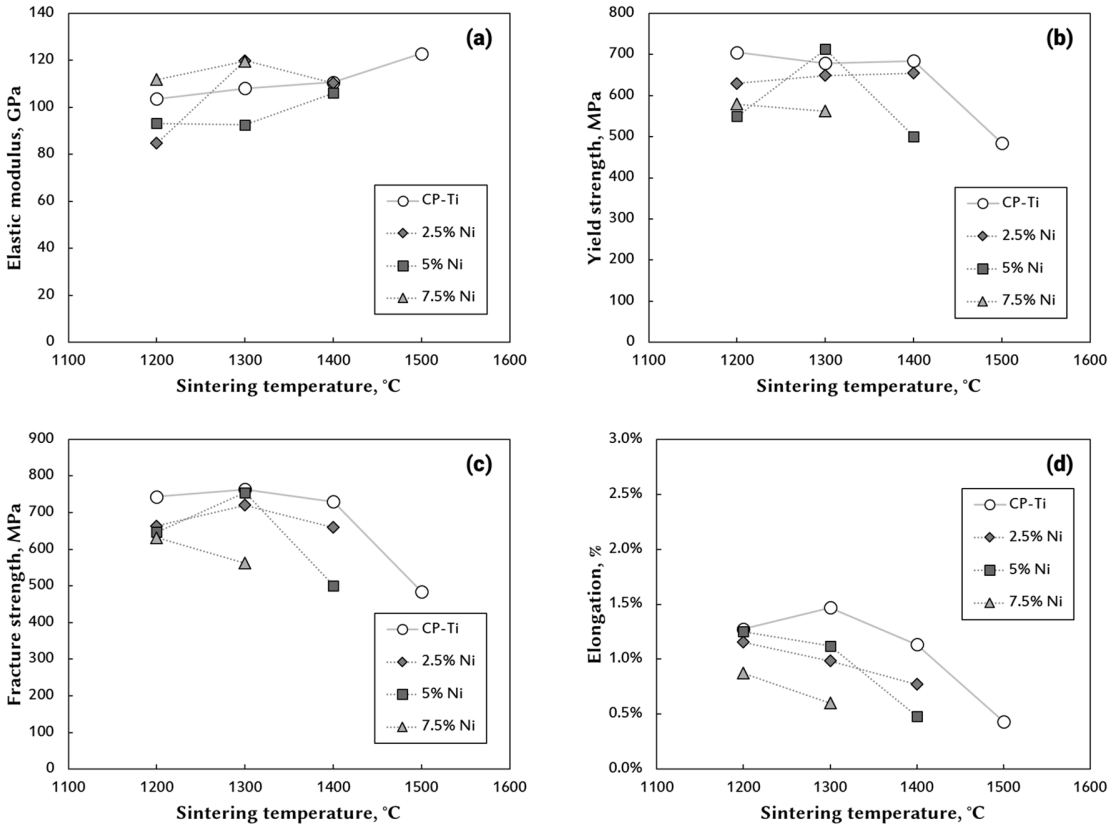

Figure 3-14. Tensile properties of the Ti-Ni alloys sintered at various temperatures: (a) Young's modulus, (b) 0.2% offset yield stress, (c) failure strength, and (d) ductility.

Examining the tensile fracture surfaces, there is a significant topological change found between samples for the differing sintering temperatures. The fracture surfaces of the 2.5 wt-% Ni and 7.5 wt-% Ni samples, sintered at 1200ºC, are selected to explain such observations (Figure 3-15). It is apparent that there is a significant morphological change from predominantly equiaxial grains on the failure surface (low Ni content), to columnar shaped grains (high Ni content). This transition mirrors the observations made in Figure 3-7(a) and (c); the brittle and rapid transgranular fracture facets coincide with the α-Ti phase locations. Therefore the decrease in ductility between the two representative samples can be directly associated to the α-Ti phase shape change (i.e. from equiaxial to elongated grains), which may be related to greater Ti_2Ni phase precipitation in the higher Ni content samples. In addition, as noted earlier, the Ti_2Ni is also a brittle phase, which will further

decrease the ductility. Consequently, the higher Ni content results in an overall lower ductility.

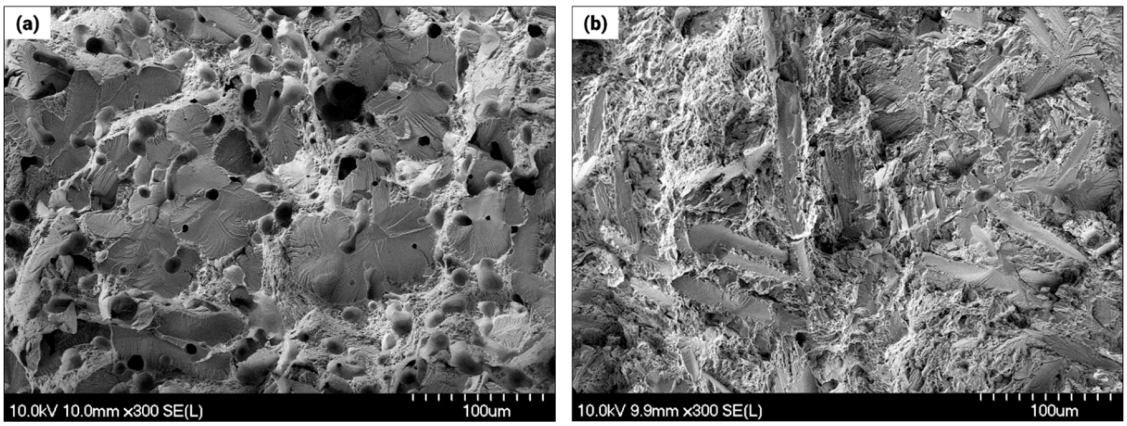

Figure 3-15. Representative tensile fracture surfaces of: (a) Ti-2.5wt-% Ni, and (b) Ti-7.5wt-% Ni. Both samples were sintered at 1200°C.

In terms of the Ti-Sn tensile properties, Sn addition generally does not improve the mechanical response (Figure 3-16). There are some exceptions for the samples sintered at 1200°C. The inferior properties most likely arise because the sintered densities of the Ti-Sn samples are lower than those achieved for the CP-Ti equivalents when sintering above 1200°C. Moreover, since there is no complex phase transformation involved, the evolution of the tensile behaviour exhibits a more linear response with respect to the sintering temperature. For the samples prepared at 1200°C, the yield strength, fracture strength and, in particular, the ductility are improved with higher Sn addition in the samples. The notably higher ductility in Ti-7.5Sn samples can be largely explained when comparing the tensile fracture morphologies for the samples prepared at 1200°C and 1300°C, as highlighted in Figure 3-17. There is a clear morphological change arising as a result of increasing the sintering temperature.

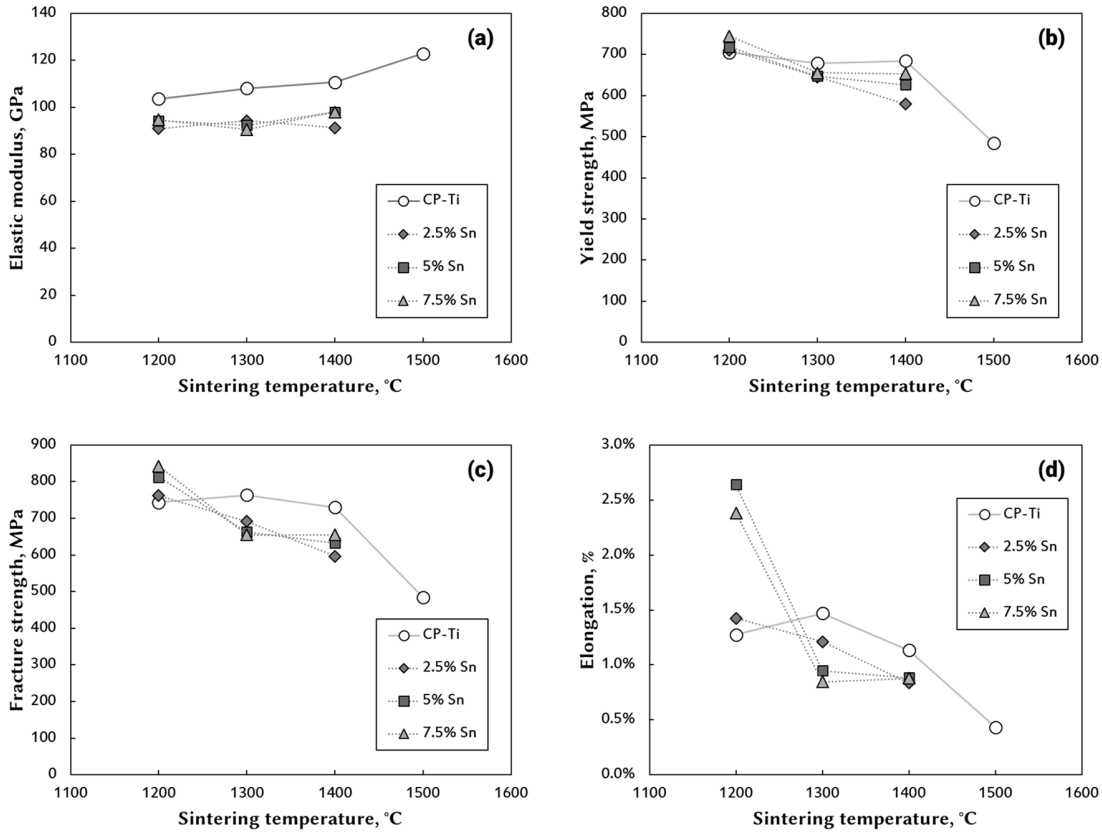

Figure 3-16. Tensile properties of the Ti-Sn alloys sintered at various temperatures: (a) Young's modulus, (b) 0.2% offset yield stress, (c) failure strength, and (d) ductility.

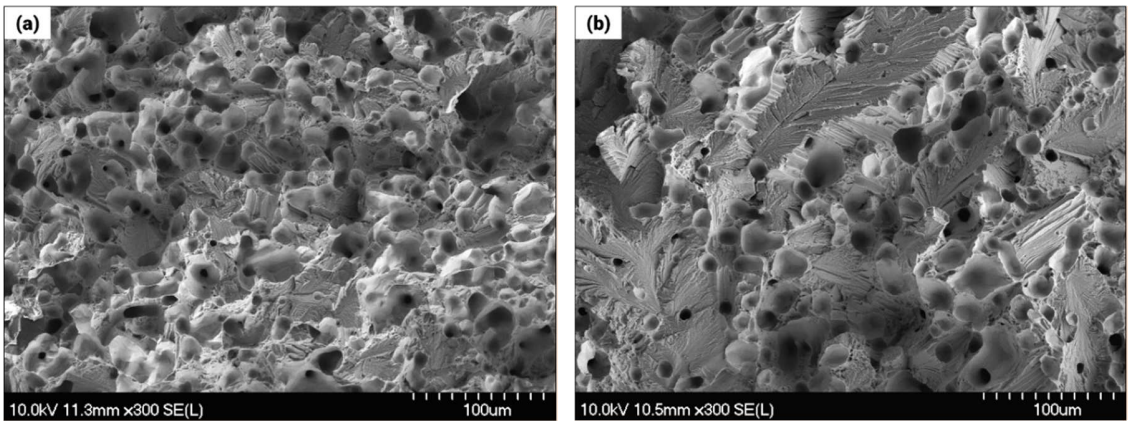

Figure 3-17. Representative fracture surface of Ti-7.5%Sn samples sintered at: (a) 1200°C, and (b) 1300°C.

3.5.3 Fracture Morphology

From examination of both the Ti-Ni and Ti-Sn fracture surfaces, the presence of the columnar α-Ti phase appears, at least in part, to be responsible for the decrease in ductility. Consequently, the processing/compositional factors that contribute to the more 'rod-like' α-Ti morphology need be controlled in order to maintain ductility. In general, the Ti-Ni samples feature a large area of flat transgranular fracture, with facets exhibiting a 'river pattern'. Conversely, the Ti-Sn samples possess more evidence of ductile dimples and pores. Both binary samples exhibit small, locally ductile regions, with micro-voids formed in between the aforementioned transgranular facet or dimple characteristics.

Nevertheless, the resultant mechanical properties of the binary systems arise from a complex combination of the densification response of the samples, their microstructures (i.e. phase assemblage, grain size, etc.), and the porosity content and configuration. It may be difficult to draw conclusions from any single factor. Furthermore, some trace elements (i.e. C, H, O, N) are known to influence the mechanical properties of Ti alloys [77,78]. With this in mind, it was demonstrated in our previous work that the HDH grade of Ti used in the present study exhibits a relatively high O content [57], which is likely to adversely affect some properties, notably the ductility.

3.6 Conclusions

A systematic investigation for the Ti-Ni and Ti-Sn binary alloys had been conducted by powder metallurgical process; the Ni and Sn additions had demonstrated distinctly different responses as a sintering aid to titanium in various aspects:

(1) The Ni additions were more positive than Sn in improving the sintered density at all sintering temperatures, benefiting from the persistent liquid phase sintering mechanism, and some localised liquid arising from the melting of intermediate phases. Conversely, the transient liquid melt from Sn incorporation was detrimental to the densification, due to the introduction of a less dense skeleton structure.

(2) The adding of Ni introduced the hard Ti_2Ni phase and altered the rounded α grains to angular shape, resulting in not only higher hardness but brittleness to the materials. The Sn addition, on the other hand, did not affect the Ti microstructure and therefore lesser change occurred to the mechanical properties.

(3) The porosity analysis provided good indication in terms of sintering mechanism, and therefore can be useful for PM processing evaluation.

More analyses are needed to understand the detailed liquid phase sintering reaction; future work in DSC would be helpful in determining the liquid formation in situ, and the use of dilatometer could identify the swelling/shrinkage during a sintering process. The results in this study nevertheless provide valuable knowledge in processing Ti-Ni and Ti-Sn binary materials.

Acknowledgements

The authors wish to thank Ms. Patricia Scallion for the SEM assistance and Mr. Dean Grijm for his support with sample machining. Funding was provided by the Natural Sciences and Engineering Research Council (NSERC) of Canada, through the Discovery Grants programme. The Canada Foundation for Innovation, the Atlantic Innovation Fund, and other partners who helped fund the Facilities for Materials Characterisation, managed by the Dalhousie University Institute for Materials Research, are also gratefully acknowledged.

Chapter 4. Synthesis and Sintering of Titanium Aluminide (Ti-48Al) Powder

(published in COM 2015 conference of Metallurgists, August 2015)

Hung-wei Liu[1], *Kevin Plucknett[1]

[1]*Dalhousie University (Sexton Campus)*
Department of Process Engineering & Applied Science
1360 Barrington St. Halifax NS, Canada B3H 4R2
*(*Corresponding author: kevin.plucknett@dal.ca)*

Abstract

Early attempts to manufacture titanium aluminides using blended elemental powders, through powder metallurgical processes, have been obstructed due to serious swelling during sintering. Although the use of pre-alloyed powder can avoid this undesired expansion problem, there are limited commercial powder sources available. Therefore, in the present research, fundamental studies on the synthesis of dual-phase (γ plus α_2) Ti48Al intermetallic materials is undertaken, in particular assessing powder manufacture. In order to produce pre-alloyed powders, highly porous Ti48Al pieces are initially sintered from elemental Ti and Al powder blends, and subsequently pulverised into powders. The powder size is then further reduced by use of either dry or wet milling processes (i.e. shatterbox grinding, attrition, or ball milling). Among these methods, shatterbox grinding has shown the highest efficiency, with a slight mechanical alloying effect observed. The manufactured powder morphologies and phases, as well the sintered material, will be discussed.

Keywords

Titanium aluminide, powder metallurgy, sintering, mechanical alloying, shatterbox, ball milling

4.1 Introduction

Titanium aluminide alloys have excellent retained strength at elevated temperatures. Their service temperature is generally intended up to ~700°C, which is comparable to the Ni-based superalloys and a great improvement to titanium alloys (limited to ~550°C). Combined with a low density (~3.8 g/cm^3), as a result of high amount of aluminium (>30 wt%), TiAl-based alloys provide considerable weight saving. Moreover, TiAl alloys have good oxidation and corrosion resistance, making them a promising material for high temperature applications, such as engine components. Aerospace and military industries have been adopting such material in some applications (e.g., low pressure turbine), to replace the conventional Ni-based superalloys (e.g., Inconel 713), achieving better fuel efficiency and high temperature performance. Two TiAl alloys (i.e., Ti-48Al-2Nb-2Cr and Ti-45Al-2Nb-2Mn + 0.8 vol.% TiB_2) have been developed and tested successfully at 560-750°C for engine applications [11]. The weight reduction (lower inertial mass) from adopting titanium aluminides not only improves the rotational performance, due to faster spin velocity and lesser lag (i.e., response time), but also decreases the load on the bearing components. As a result more weight saving can be achieved from both the direct material replacement and for the supporting parts, all of which translate to a considerably improved fuel economy [3]. However, the lack of ductility in titanium aluminides at room temperature makes them difficult to manufacture by traditional thermo-mechanical processes (e.g., forging or rolling). TiAl alloys are generally vacuum cast, followed by hot isostatic pressing, to eliminate casting defects [11,79]. As a result, titanium aluminide alloys are expensive and limited to niche applications.

Powder metallurgy (PM), a cost-effective manufacturing approach, has shown considerable success for industrial production of some Fe and Al alloys [55]. This near-net-shape process requires minimum post-machining and therefore could be an ideal approach for manufacturing titanium aluminide alloys. Such technology can potentially reduce the production cost and thus further expand the use of TiAl in high volume consumer products, such as exhaust valves and turbo charger rotors in automobiles [15,16,79]. However, applying elemental Ti/Al PM has demonstrated difficulties in fabricating dense TiAl alloys. A severe swelling phenomenon occurs when sintering the

elemental Ti and Al blend. Previous studies have attempted to control the expansion, including incorporating a low temperature hold to remove elemental Al (up to 150 hours, at 520°C to 650°C) [80], and using a rigid constrained mold to supress the swelling during sintering [81]. The use of prealloyed powder can circumvent the aluminium melting, and thus avoid the associated severe swelling during sintering. Therefore, prealloyed titanium aluminide powder for the press-and-sinter PM approach seems necessary. Nevertheless, there are limited commercial TiAl powder sources available. As a result, the current work assesses the manufacture of pre-alloyed TiAl powder.

Some fundamental aspects of elemental powder sintering are assessed, including the Al powder size, low temperature holding and two-step sintering. To achieve a powder with a suitable titanium aluminide composition, a heat treatment process has been developed, and the resultant phase transition through each procedural stage has been analysed. For solid state sintering, finer powder could facilitate the diffusion reaction and result in better densification; therefore, milling stages have been incorporated and evaluated. The developed pre-alloyed TiAl powder is finally evaluated in terms of its densification response through applying a regular sintering process.

4.2 Materials and Methodology

The powders used in this study were an Mg-reduced titanium sponge powder (-100/+325mesh, Lot# ES019-1-9) acquired from Reading Alloys, Inc. (Robesonia, PA, USA), a fine aluminium powder (AS MEP 107, 99.7% purity, D_{50} = 6.4 μm), and a coarse Al powder (AS 081, 99.5% purity, D_{50} = 43 μm); both Al powders were obtained from Ecka Granules GmbH (Fürth, Germany). Figure 4-1 illustrates the morphology of a typical powder blend. The titanium had a more angular shape while the Al powder was rounded. The particle size distribution of each of the powders is presented in Figure 4-2, showing considerable size differences between them.

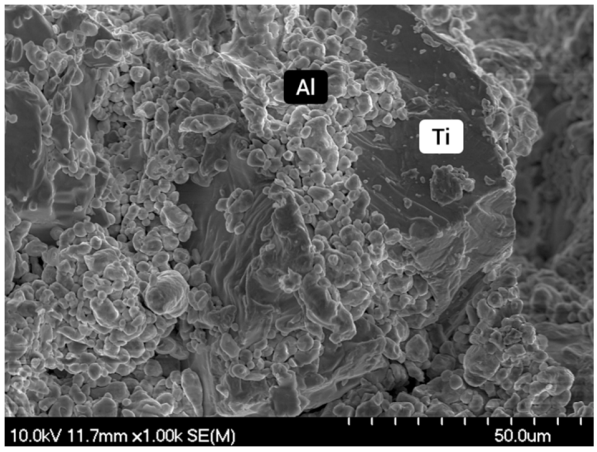

Figure 4-1. Micrograph of the Ti and Al (fine) elemental powder blend.

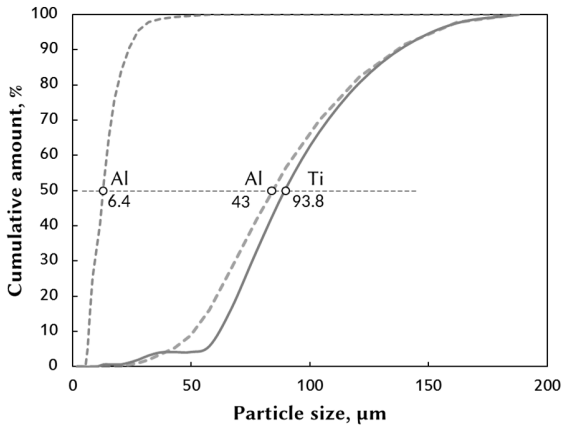

Figure 4-2. Particle size distribution of initial elemental Ti and two Al powders.

Titanium with 48 atomic weight percent Al (hereafter % for atomic weight percent in this chapter) powder blends were mixed (Turbula T2F, Glen Mills Inc., Clifton, NJ, USA) for 30 minutes. For the elemental PM trials, round disc samples (15 mm in diameter, ~4 g mass) were firstly uniaxially pressed by hydraulic compaction press (Satec 5594-200HVL, Instron, Norwood, MA, USA) at 100 MPa to shape the preforms; higher pressures up to 400 MPa were subsequently applied to the preformed samples by cold isostatic pressing (CIP; Avure Technologies Inc, North Lewis Center, OH, USA). The pressed green discs were then sintered in a high vacuum (10^{-5} torr) furnace (J-8x10-WM-1650-VG, Materials

Research Furnaces, Sunhook, NH, USA) for various heating profiles, as outlined in Figure 4-3.

For the TiAl powder production, each portion of a 30 g Ti-48%Al elemental blend was CIPed at 100 MPa to produce billets for sintering. The Ti-48%Al pieces were sintered in a tube furnace (Sentrotech STT-1600C, Strongsville, OH, USA) at 1200°C, for two hours, under constant argon flow. The heating and cooling rate were controlled at 5 °C/min. The cooling rate decreased to a natural furnace cooling when the temperature was below 200°C. The synthesised pre-alloyed metal billets were subsequently manually broken into smaller pieces. The coarse powder was further pulverised by shatterbox and ball milling methods, as highlighted in Table 4-1.

In the ball milling steps, a suspension solution of 250 ml hexane solution was required to avoid powder agglomeration. It should be noted that a shatterbox milling treatment for 30 minutes was performed prior to the wet processes, to bring down the powder size to suitable scale for subsequent processing. The ground powder was dried in air under a fume hood for 24 hours and then collected. To validate the produced powders, individual samples (~6 g mass) were CIPed at 400 MPa, and sintered at 1300°C for 2 hours. The complete process procedures are outlined in Figure 4-3. The green density was calculated from the dimensions of each pressed sample. The sintered density of the samples was determined by an oil immersion method, in accordance with the ASTM Standard B328. The particle size distribution was determined using a particle size analyser (Master Particle Sizer 20600, Malvern Instruments, Worcestershire, UK). The powder phases were identified by an X-ray diffractometer (D8 Advance, Bruker Instruments, Madison, WI, USA) and the microstructures of the synthesised powders, and the sintered samples made from those powders, were examined using a SEM (Hitachi S-4700, Tokyo, Japan). The sample compositions were analysed by an EPMA (JEOL JXA-8200 SUPERPROBE, Peabody, MA, USA).

Table 4-1. Pulverisation method parameters.

Method	Shatterbox milling	Ball milling
Process time	30 min	24 h
Media type	Alumina puck	Alumina ball (11 mm ∅)
Media to powder weight ratio	n/a	20:1
Chamber volume	50ml	250ml
Suspension solution	n/a	Hexane

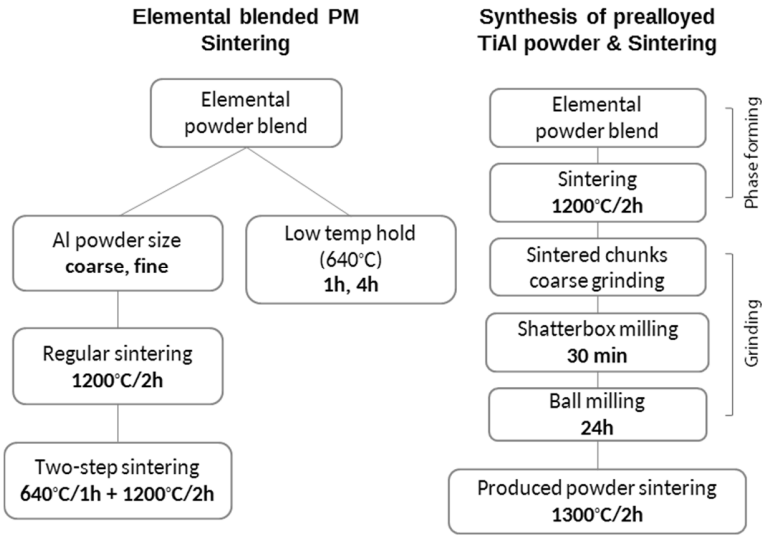

Figure 4-3. Sample production and experimental procedures.

4.3 Results and Discussion

4.3.1 Sintering of Blended Elemental Powders

Conventional blended elemental PM approach was examined in the study. Prior to sintering, the ductile, elemental Ti and Al powder blend could be pressed to a high green density, close to 95% of theoretical (Figure 4-4). However, serious swelling occurred after sintering (Figure 4-5). To avoid swelling, a two-step sintering process was designed, in which a low temperature stage (i.e., 640°C for one hour) was implemented; the elemental

blended samples were heat treated under solid state diffusion conditions, before Al melting (660°C) taking place. Nevertheless the extra heating stage did not minimise the expansion. The effects of Al powder size were also examined (Figure 4-6). Coarser Al powder did exacerbate the expansion, due to the larger voids after Al had melted. Furthermore, extending the low temperature holding from one to four hours only slightly improved the densification (Figure 4-7). In addition, from Figure 4-5 and Figure 4-6, higher pressing pressure (400 MPa vs. 300 MPa) shows improved sintered density (57.9% vs. 53%, respectively) likely because of the higher green density. The sintered structure (two-step heating) is generally poorly densified, showing a "loose", open structure, as demonstrated in Figure 4-8.

Although such swelling problems have been addressed in early researches, it could not be eliminated [81–83]. The severe swelling is due to several factors:

(i) fine porosity form Kirkendall effect as a result of large diffusivity difference between Ti and Al [84],

(ii) the formation of $TiAl_3$ loose structure [85],

(iii) expansion from the Al melt, and

(iv) larger pores from Al melt flowing away caused by gravity and capillary force [86].

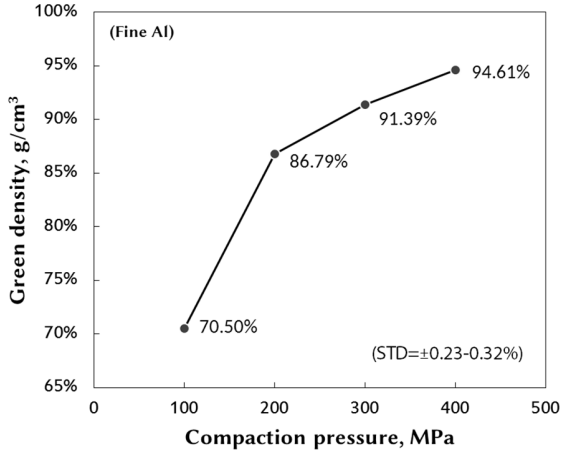

Figure 4-4. Effects of compaction pressure to green density.

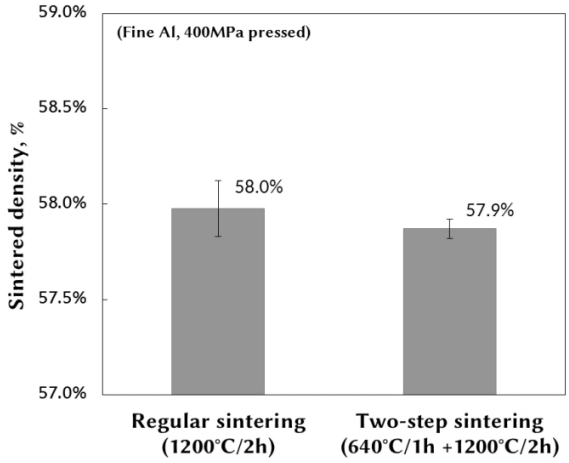

Figure 4-5. Sintered density of one and two step sintering process.

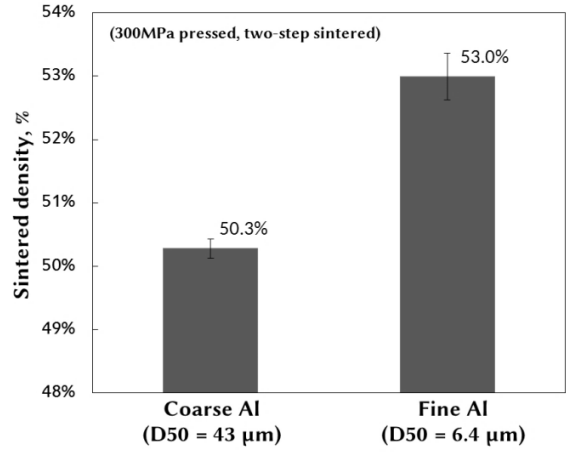

Figure 4-6. Al size effect in sintered density.

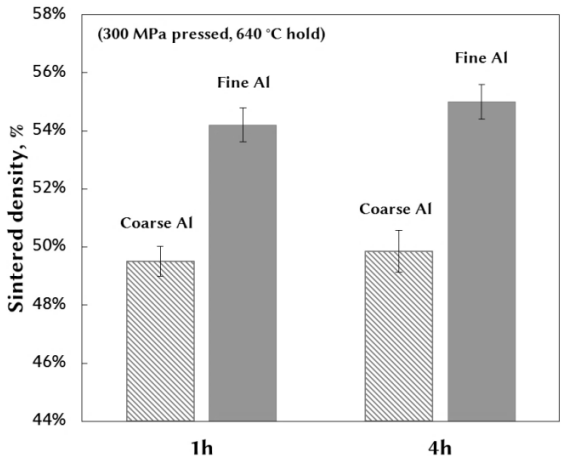

Figure 4-7. Effects of Al particle size and holding time in low temperature (640°C) sintering tests.

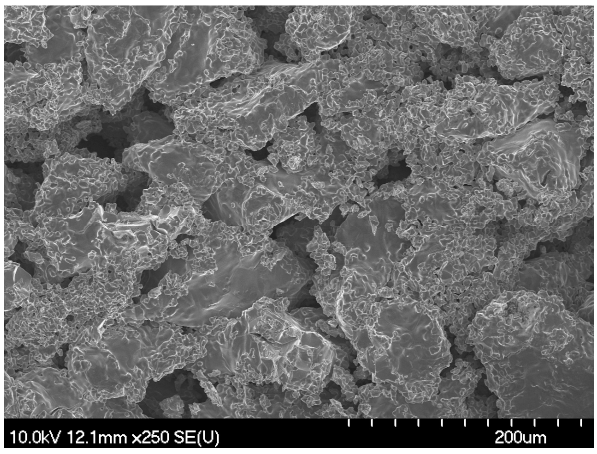

Figure 4-8. Loose structure from sintering elemental Ti/48Al blend (two-step sintering).

4.3.2 Constituent Phase Evolution and Prealloyed Powder Production

Due to the difficulties encountered in elemental powder sintering, prealloyed TiAl powder was produced in this study to avoid the Al melt and Kirkendall effects, so that swelling was avoided. In order to investigate the reaction sequences, the crystalline phases at each stage were examined by XRD, as shown in Figure 4-9. The material underwent several phase transformations at different processing stages, from the elemental blend to the prealloyed powder, and finally to the sintered products. At low sintering temperature

(640°C), before the Al begins to melt, samples consisted of mostly intermediate phases (i.e., $TiAl_2$ and $TiAl_3$) and Ti_3Al. It should be noted that low temperature sintering (640°C) was not a separated procedure in the prealloyed powder production; extra samples were produced in this condition only to examine the phase constituents. The elemental Ti and Al powder compact is similar to the diffusion couple situation, where previous studies had found that the only intermetallic phase $TiAl_3$ was formed if the temperature was maintained below the melting point of aluminium [80,87]. It was shown that the $TiAl_3$ acted as a physical barrier, and there was essentially no interdiffusion between Ti and $TiAl_3$ when spark plasma sintered at 600°C for up to one hour, leaving unreacted Ti [88]. However in the present research, the elemental Ti and Al had fully reacted, leaving no trace of Ti and Al, and the predominant phase was $TiAl_2$, followed by Ti_3Al and $TiAl_3$. Prolonging the soaking time from one to four hours at 640°C did not affect such constituents (XRD not shown).

When the elemental powder compact (green) was sintered at 1200°C for two hours, the sintered samples were generally TiAl, with a small amount of Ti_3Al. This process was adequate in temperature and duration, as none of the intermediate phases existed. In both of the subsequent grinding processes, particularly ball milling for 24 hours, TiAl peak broadening occurred because of the strain and the associated crystal lattice imperfections introduced from severe deformation. In addition, Ti_3Al peaks (notably the strongest one) were promoted with more milling, indicating a mechanical alloying effect. Although the diffracted intensity not linearly dependent on concentration, it can be used as a general indication for the phase amount [89]. The relative ratio of the strongest peaks of the Ti_3Al to TiAl phase had increased with the amount of grinding. In the last manufacturing process examined (i.e., final sintering), it is clear that the broader TiAl peaks reappeared and, more importantly, the Ti_3Al peaks developed further. This indicates the final material should consist of more Ti_3Al phase. Based on the Ti-Al phase diagram, the Ti-48Al alloy consists predominantly of the phase γ-TiAl, with a small volume fraction (~6.6 vol.%) of the phase α_2-Ti_3Al below 500°C, under equilibrium conditions [90].

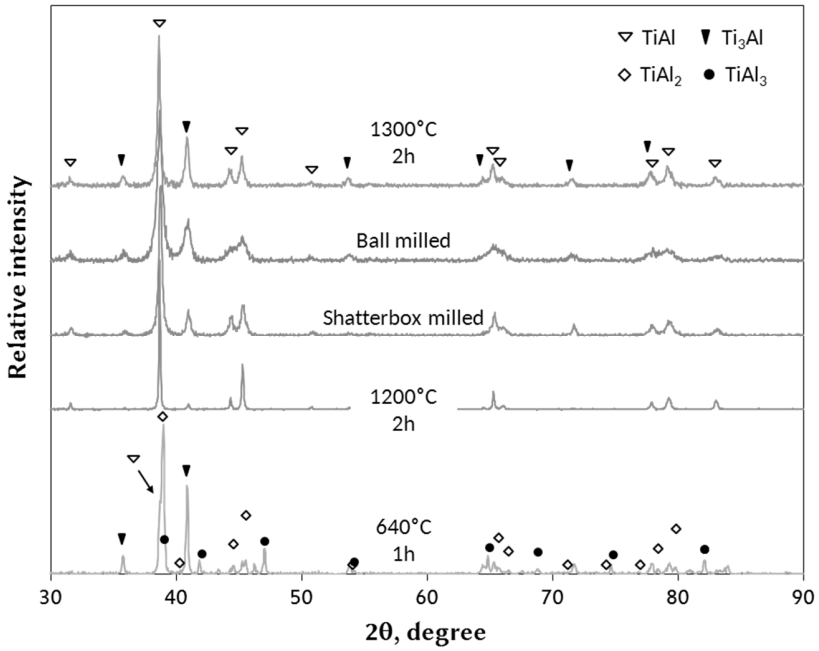

Figure 4-9. XRD patterns showing phase evolution at individual processing stages.

After shatterbox milling the powder generally has a rounded shape, while further ball milled powder is more angular (Figure 4-10). In the present study, the effects of powder morphology were not investigated. It should be noted, however, that the powder packing and compaction behaviour, and the subsequent sintering densification could be affected by the powder size and shape. Figure 4-11 illustrates the milling effects in terms of particle size reduction. It is believed that a finer powder would facilitate solid state sintering and improve the densification. However, the contaminations associated with the milling processes would likely increase. The initial sintered density was ~83.7% of theoretical (standard deviation ±0.37%) using the ground powder, a significant improvement compared with the elemental blend sintering.

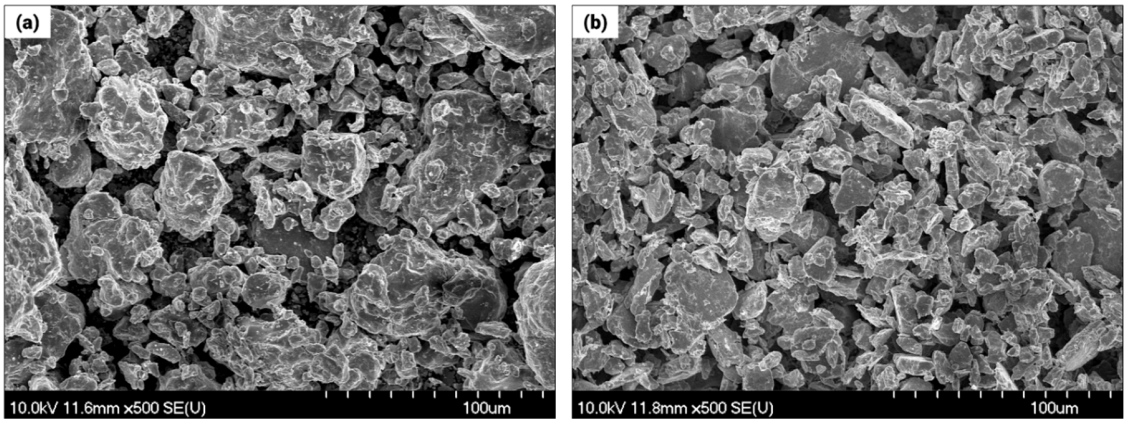

Figure 4-10. Micrographs of (a) shatterbox milled and (b) subsequently ball milled pre-alloyed powders.

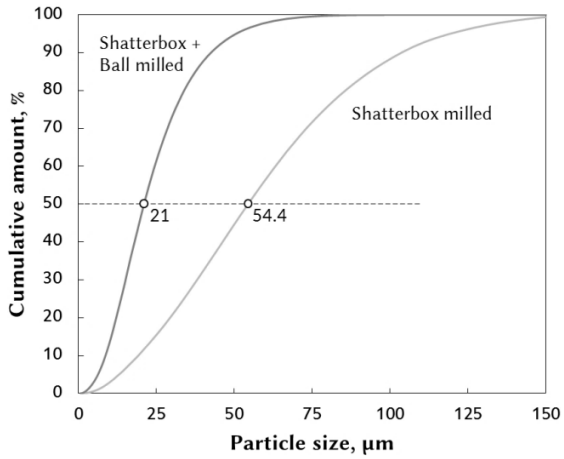

Figure 4-11. Particle size reduction resulted from shatterbox and the subsequent ball milling.

4.3.3 Microstructure Characterisation

Examining the microstructures of the sintered and etched samples, four phase features are generally distinguished, as indicated in Figure 4-12. These features are identified as: A - light smooth area, B - dark smooth area, C - roughened area and D - more roughened area. Although their morphologies are noticeably dissimilar, from the chemistry analysis (i.e., EPMA) all four areas are generally not distinct in terms of the Ti to Al ratio (very close to 1:1) with only small fluctuations in concentration (standard deviation

±1.08% to 3.92%). It is believed that the different morphologies (see detailed SEM in Figure 4-13) between the etched surfaces are in part due to their different crystalline orientations (A and B), and also the various ratio of Ti_3Al and TiAl combinations. As indicated earlier in the XRD analysis, the final sintered material is comprised of TiAl and Ti_3Al phases. Nonetheless, there are few locations that were attributed to a specific Ti to Al ratio spread throughout these phases. However, only with increased sintering duration to 4 hours (results not shown) did this atomic ratio became more clear and prevalent in those phases, particularly in regions C and D. Generally those locations contained around 6o at.-% Ti, and such Ti to Al constituent ratio (Ti:Al = 6:4) is believed to consist of a mixtures of 3 parts TiAl and 1 part Ti_3Al. The ratio and morphology suggest that area A and B are the single γ-TiAl phase, whereas the C and D are the two-phase γ plus α_2 (TiAl plus Ti_3Al) areas. Based on those observations, the sample possesses a duplex structure consisting of γ and γ/α_2 phase configurations, and with higher level of sintering (longer time) Ti seems to concentrate to the roughened areas (i.e., area C and more to D). Combined with the discussed XRD results, the resultant phases in each stage can be summarised in Table 4-2, showing a phase evolution for the Ti48Al material.

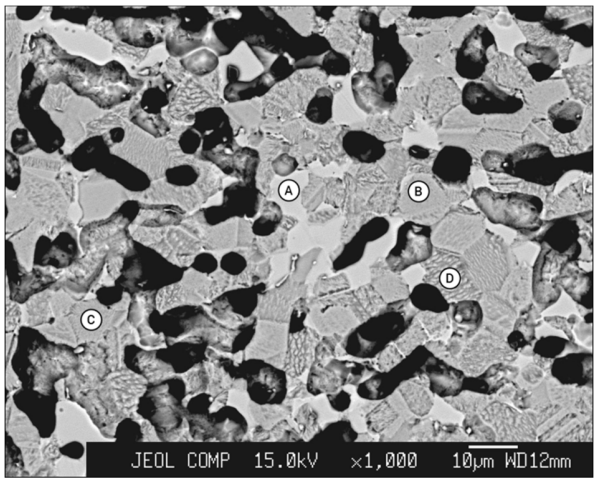

Figure 4-12. Microstructures of the sample (1300°C for 2 hours) sintered with prealloyed Ti48Al powder, displaying four phase morphologies. Area A and B show smooth surfaces, while area C and D display roughened morphologies.

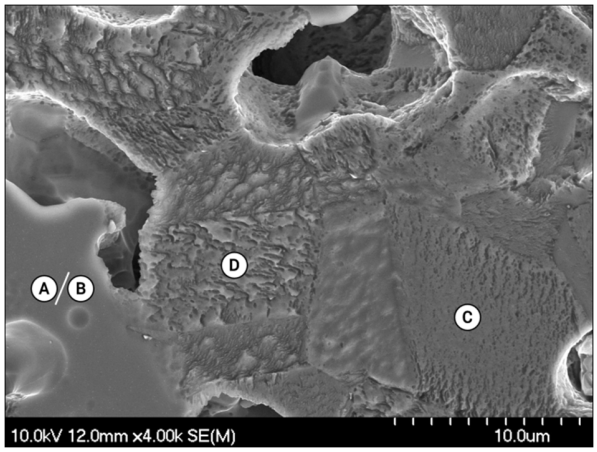

Figure 4-13. High magnification micrograph of the sintered sample (1300°C for 2 hours) showing detailed phase features: area A and B as smooth areas, while area C as the roughened area and area D as the more roughened area.

Table 4-2. Phase(s) at different process stages.

Stage	640°C / 1h	1200°C / 2h	Grinding	1300°C / 2h	1300°C / 4h
Phases	$TiAl_2$ + Ti_3Al + $TiAl_3$	TiAl (minimal Ti_3Al)	Promoting Ti_3Al	TiAl + Ti_3Al	Better defined (γ+α_2) phase

4.4 Conclusions

A pre-alloyed TiAl powder, in the 20 μm (D_{50}) size range, was produced in the present study. Sintering using such powder resulted in an improved density (~84% of theoretical) in comparison to when using an elemental blend (~58% of theoretical). Sintering an elemental Ti/Al blend generated a poorly densified structure, due to swelling from the $TiAl_3$ formation (Al melting) and Kirkendall porosity. Once the sintering temperature was above 1200°C, all intermediate phases ($TiAl_2$, $TiAl_3$) disappeared and a duplex γ and γ/α_2 structure was developed. The secondary milling process not only reduced the particle sizes but also promoted the Ti_3Al phase (presumably though mechanical alloying). The powder manufacturing processes established in the study could be further improved for better efficiency, and other parameters, such as the particle size ranges, can be controlled based upon the current experiences. It was apparent that the Ti concentrated

to the γ/α_2 two-phased area with further sintering, resulting in a 3TiAl plus Ti_3Al (Ti:Al=6:4) combination. Future work evaluating a broader range of sintering conditions will provide a better understanding of the diffusion mechanisms and sintering behaviour. In addition, studies of the effects of powder size, in terms of sintered densification and associated contamination, will be conducted to investigate the relations between the processing approaches and properties.

Acknowledgements

The authors would like to thank the Natural Science and Engineering Research Council of Canada (NSERC) and its Automotive Partnerships Canada (APC) program for their financial support of this research. They would also like to thank Wescast Industries Inc. and Kingston Process Metallurgy Inc. for their financial, in-kind and technical support. The support of the Canada Foundation for Innovation, the Atlantic Innovation Fund, and other partners who helped fund the Facilities for Materials Characterisation, managed by the Dalhousie University Institute for Materials Research, are gratefully acknowledged.

Chapter 5. Titanium Aluminide (Ti-48Al) Powder Synthesis, Size Refinement and Sintering

(submitted to Advanced Powder Technology, June 2016)

Hung-Wei Liu and Kevin P. Plucknett*

Materials Engineering, Department of Process Engineering and Applied Science, Dalhousie University, 1360 Barrington St., Halifax, Nova Scotia, Canada

Abstract

Titanium aluminide based alloys have shown significant potential in high temperature applications, but the high production cost of TiAl considerably limits its utilisation. Although the use of powder metallurgy processes can reduce the cost by minimising post-machining, an economical powder production route is still required. Therefore, in the present study a pre-alloyed Ti-48Al powder is developed using an elemental Ti and Al powder blend prepared using a simple vacuum heat treatment. A formation model of the intermetallic phases (i.e. TiAl, Ti_3Al, $TiAl_2$, $TiAl_3$) during powder synthesis is proposed. In order to improve the sinterability, various milling methods (i.e. ball, attrition and shatterbox milling) are examined to reduce the particle size. The sintered microstructures, particularly the two-phased (α_2-Ti_3Al γ-TiAl) lamellar structures are also investigated. Improved densification is achieved at 1300°C, held for 2 hours, using the manufactured powder, compared to the elemental powder blend (~55%). With higher sintering temperatures or longer hold periods, increased density TiAl components are possible.

Keywords

powder metallurgy; microstructure evolution; milling; scanning electron microscopy; optical microscopy

5.1 Introduction

Fuel efficiency in transportation has become not only an economical consideration but also an environmental issue. To reduce fuel consumption, the use of light materials or better engine performance in a vehicle are important. Titanium aluminide (TiAl) based alloys have drawn considerable attention for engine applications due to their low density and excellent high temperature properties, including good strength retention and oxidation resistance above 500°C [91]. These properties make TiAl alloys very attractive alternatives to the conventional high temperature Ni-based super-alloys (e.g. Inconel 713C) [16]. As a consequence, the aerospace and military industries have adopted TiAl alloys in several areas. For example, the Ti-48Al-2Nb-2Cr alloy developed by GE is used in the production of low-pressure turbines [14,92], while the Ti-45Al-2Nb-2Mn + 0.8 vol% TiB_2 (XD) alloy is designed for missile fin applications [11,93]. Despite these advantages, TiAl-based alloys generally have low ductility at room (or low) temperature. Consequently, it is difficult to perform thermomechanical processes or post-fabrication machining to the semi-finished products. To avoid or minimise component forming, several studies in the automobile industry have been conducted to utilise the TiAl alloys formed through near-net shape casting processes. Considerable effort has been devoted to minimising the composition segregation and texture during solidification [94], for example, using the LEVICAST [16] or centrifugal casting processes [13]. Although TiAl-based valves and turbochargers have been successfully produced [13,20], the manufacturing costs are high, and therefore the current applications of TiAl-based alloys are particularly restricted in consumer markets.

As an alternative, powder metallurgy (PM) processes provide the near-net shape forming capability, but with lowered segregation concerns. The simple press-and-sinter process, using elemental powders, delivers a cost-effective approach and has been successfully developed for selected steel and Al alloys in mass production [55]. However, for TiAl-based alloys, sintering elemental Ti-Al powder blends results in severe swelling in the sintered products; expansion is caused by the formation of $TiAl_3$ in the early sintering stages [85]. Moreover, there is a small Kirkendall porosity volume generated, due to large diffusivity difference between Ti and Al atoms [81], and as well larger pores formed when

the Al melts and flows away due to gravity or capillary force [95]. As a result, many PM studies on TiAl-based materials use gas atomised prealloyed powders to avoid swelling [96], and are conducted using hot isostatic pressing (HIP) to ensure a fully dense material. Nonetheless, there is very limited availability of commercial prealloyed TiAl powder, and the HIP process adds a significant cost in manufacturing. Therefore, some recent research has been focused on hot pressing or other more economical fabrication methods [95–97]. Conversely, several other studies have attempted to mitigate the elemental sintering expansion by implementing long sintering times, higher temperatures or multiple sintering stages into the process [81]. However, it invariably has remained that the porous structure is difficult to densify.

In the present study, instead of improving on the elemental sintering, the porous sintered product was subjected to various milling treatments as a prealloyed powder, and the elemental Ti-Al blend sintering was considered as an initial stage to form the intermetallic phases (i.e. γ-TiAl and α_2-Ti_3Al). Thus, sintering will be a solid-state diffusion process with the pre-alloyed TiAl particles. This way, the swelling problem should be circumvented during sintering while still utilising the economical elemental powders. Several milling processes were examined in the present work to reduce the powder size. The effects of powder size on the sintering response and resultant microstructures were investigated, together with the sintering time and temperature. The phase evolution and sintering mechanisms of the manufactured powders were subsequently analysed.

5.2 Materials and Methods

The two elemental powders used in this study were an Mg-reduced Ti sponge powder (-100/+325mesh, Lot# ES019-1-9) acquired from Reading Alloys, Robesonia, PA, USA and an Al powder (grade: AS MEP 107) from Ecka Granules, Fürth, Germany.An elemental powder blend of Ti-48% Al (all compositions are given in atomic percent unless stated otherwise) was thoroughly mixed in a Turbula T2F mixer (Glen Mills Inc., Clifton, NJ, USA) for 30 minutes. Each portion of 30 g Ti-48%Al powder blend was cold

isostatically pressed (CIP; Quintus Technologies Inc., Västerås, Sweden) at 100 MPa to form green compacts. The Ti-48%Al compacts were then heat-treated in a tube furnace (STT-1600C, SentroTech, Strongsville, OH, USA) at 1200°C for two hours, with a constant Ar gas flow through the whole process. The heating and cooling rate were controlled at 5°C/min. The cooling rate decreased to a natural furnace cool when the temperature was below 200°C. The sintered (prealloyed) compacts were later broken down roughly using a manual hand press. The coarse metal pieces were further milled by various means, as summarised in Table 5-1. In addition, some coarse pieces were also instead hand ground to serve as the baseline process for subsequent milling.

Table 5-1**.** The parameters employed for the various milling methods.

Method	Ball milling	Attrition milling	Shatterbox milling	Shatterbox (large) milling
Process time	0.5, 1, 2, 24 h	0.5, 1, 2 h	30 min	10, 20, 30, 60 min
Media type	Zirconia 11 mm ∅	Zirconia (YSZ) 6 mm ∅	n/a	n/a
Media to powder weight ratio	20:1	20:1	n/a	n/a
Suspension solution	Hexane (HX)	IPA	n/a	n/a
Code*	BM**	AT**	SB	SBL

**Process designation: code-process time-solution or addition*
***Both BM and AT procedures included a prior SB-30m process.*

For the wet processes (i.e. ball and attrition milling), a suspension medium of 250 ml hexane or isopropanol alcohol (IPA) was added to the milling chamber to avoid powder agglomeration during milling. It should be noted that a 30-minute shatterbox milling treatment was performed on the powder to bring down particle size to a suitable scale prior to the wet processes. The ground powder was dried in air under a fume hood for 24 hours and then collected. Regarding the dry process (shatterbox milling), two sizes of shatterbox, along with their respective rolling tables, were employed. While the small shatterbox (50 ml, 835 rpm; Model 8500, SPEX SamplePrep, Metuchen, NJ, USA) provided only

moderate grinding efficiency, the larger shatterbox (250 ml, 950 rpm; Model TM/MAX2, TM Engineering Ltd., Burnaby, BC, Canada) operated with a more rigorous motion in combination with a heavier ring and puck, consequently delivering much higher crushing momentum. As such, the larger shatterbox process was stopped for 15 minutes for every 5 minutes of milling to prevent excessive heat increase and maintain a moderate temperature until the desired milling time was completed. In the tests relating to the use of process control agents (PCA), a small amount (1 wt-% or 1.5 wt-%) of Licowax® (LC) was added to the powder mixed in the shatterbox (large) milling process.

To investigate the sinterability and the related particle size effects of the produced powders, 6g samples from the respective grinding processes were cold isostatic pressed (CIP) at 400 MPa and then sintered at 1300°C with the previously outlined furnace conditions. An overview of the sample preparation procedures used in this study, including each of the milling methods employed, is outlined in Figure 4-3. The sintered density of the samples was determined using the oil impregnation method, in accordance with the ASTM Standard B328 (MPIF Standard 42). Differential scanning calorimetry (DSC; NETZSCH 404F1) was employed in order to detect the Al melting temperature of powder mixtures during sintering. The particle size distribution of the respective ground powders was measured using a particle size analyser (Master Particle Sizer 20600; Malvern Instruments, Malvern, UK). The crystalline powder phase composition was identified through X-ray diffraction (XRD; D8 Advance, Bruker Instruments, Madison, WI, USA). The microstructures of both the manufactured powders and sintered samples were characterised using a scanning electron microscope (SEM; Model S-4700, Hitachi High Technologies, Tokyo, Japan). Localised sample compositions were analysed using an energy-dispersive X-ray spectroscopy (EDS; Model Inca X-MaxN, Oxford Instruments, Concord, MA, USA) detector, housed within the SEM. More detailed phase identification was conducted using a wavelength-dispersive X-ray spectroscopy (WDS) in an electron probe micro-analysis system (EPMA; JXA-8200 Superprobe, JEOL Ltd., Tokyo, Japan). Chemical analyses of selected interstitial elements (i.e. C, H, O and N) were conducted by ATI Wah Chang analytical laboratory (Albany, OR, USA); C was determined using a Leco CS-444, H with a Leco RH-404, and O and N with a Leco TC-436 (all instruments Leco Corp., St. Joseph, MI, USA).

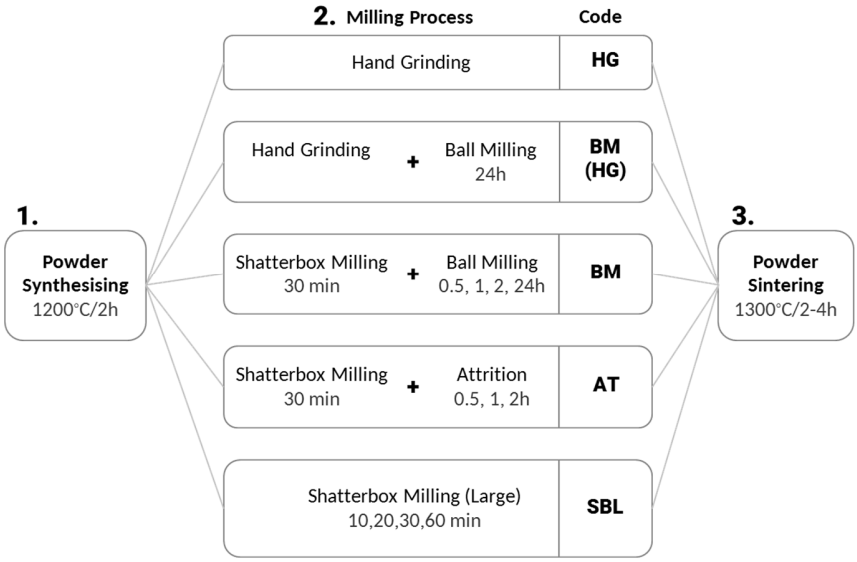

Figure 5-1. Experimental process flowchart, outlining the respective milling methods.

5.3 Results and Discussion

5.3.1 Phase Constituents after Powder Processing and Sintering

As shown in the micrographs of the starting materials in Figure 5-2, the Ti powder displays a more angular particle morphology, while the Al powder is generally rounded. Figure 5-3 illustrates the particle size distribution for both powders, indicating a considerable size difference between them, which will facilitate moderate packing densities during compaction.

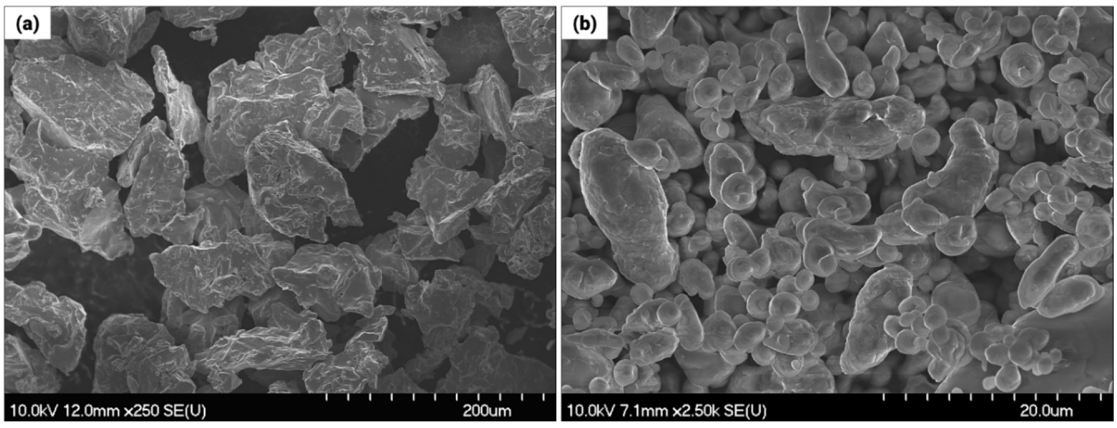

Figure 5-2**.** Typical SEM micrographs of the elemental starting powders: (a) Ti and (b) Al.

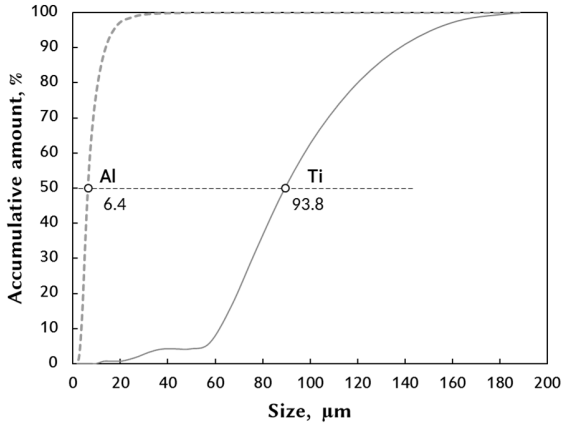

Figure 5-3. Particle size distribution of the elemental Ti and Al starting powders.

As noted earlier, in order to avoid the swelling and Kirkendall porosity issues, it is anticipated that a pre-alloyed titanium aluminide powder is necessary for solid state sintering. The pre-alloyed powder developed in the current study was produced from sintering elemental Ti and Al compacts, using a one-step isothermal heating. The synthesised powder was subsequently milled to reduce its particle size, and the milled powder was again pressed and sintered to generate the finished product. This section discusses the crystalline phases in the material at respective stages in the process (i.e. powder synthesising, milling, sintering). The phases were analysed by XRD and their respective patterns after each process stage are shown in Figure 5-4. Separate samples, sintered at low temperature (640°C), were also prepared for analysis to more fully understand the phase transformation before the Al powder has melted (i.e. at nominally 660°C).

From Figure 5-4 it is apparent that samples sintered at 640°C, no trace of residual unreacted pure Ti and Al was shown, and the material consisted of mostly intermediate titanium aluminide phases (i.e. $TiAl_2$ and $TiAl_3$), together with the targeted 'equilibrium' phases (i.e. TiAl and Ti_3Al) according to the phase diagram at temperatures below 500°C [84]. However, several previous studies of Ti and Al diffusion couples have concluded that the $TiAl_3$ phase was the only reaction product at temperatures from 400 to 650°C, despite

the use of long annealing times [98–100]. A PM study conducted by Yang and Hwang also confirmed that only the $TiAl_3$ phase was seen when annealing the elemental Ti and Al powder compact at 645°C for 15 hours [81]; in their study coarse Al (149 µm) and Ti (-100+270 mesh) powders were utilised. The large particle sizes can be anticipated to result in a lower Ti-Al contact area, and hence the diffusion would be much slower than the one in the present study, using significantly finer powders. The contacting area is even lower in the Ti-Al diffusion couple experiments if considering the contacting area per unit volume, since phase transformations are determined not only by thermodynamics but also kinetics, particularly in a non-equilibrium reaction. As a result, the complex phase transformation was likely facilitated at 640°C using the fine Al powder, and phases other than $TiAl_3$ were therefore formed in the present experiment. Further increasing the isothermal hold time to four hours, at 640°C, did not result in any significant differences in the XRD pattern (not shown).

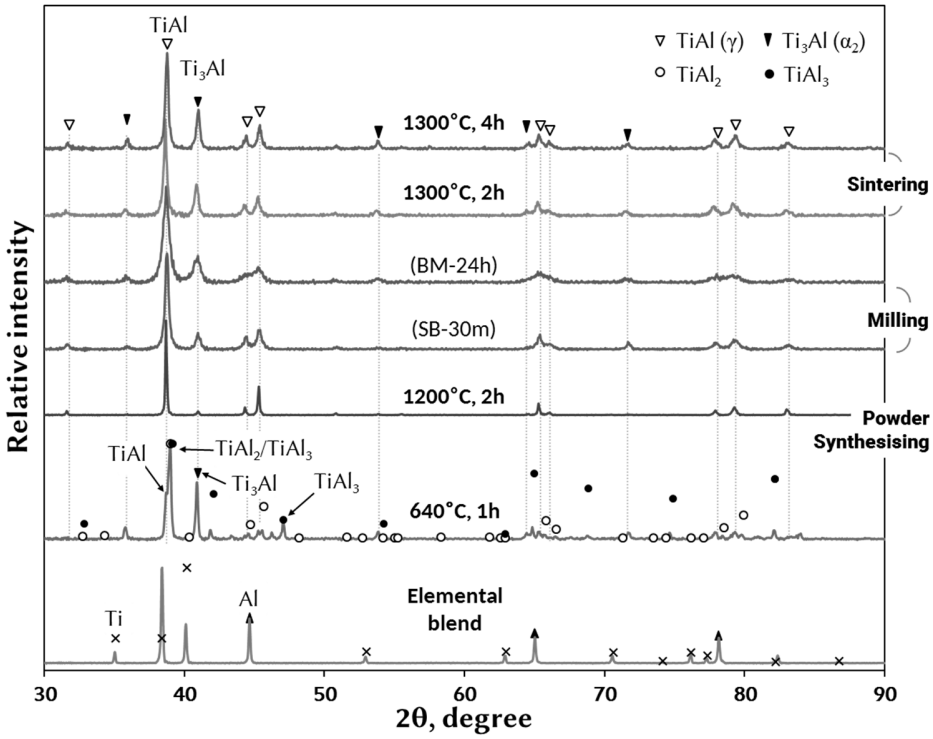

Figure 5-4. XRD pattern highlighting the crystalline phases in materials processed at various stages.

When the powder synthesis was nominally completed (i.e. heat treated at 1200°C for 2h), all the intermediate phases in the powder mixture had disappeared, and the resultant XRD pattern distinctly shows the γ-TiAl phase with a small amount of α_2-Ti_3Al. The strong Ti_3Al phase peak in the material heat treated at 640 °C considerably decreased after heat treatment at 1200°C. Further examination on the synthesised powder revealed it was not homogeneous. Instead the powder was comprised of layered internal structures; this is discussed in more detail in Section 5.3.4: *Powder internal structure formation*. If fully revealed during analysis, the respective phase portions would effectively account for their relative XRD peak intensities. Consequently, the change in the XRD intensity is thus due to the phase transformation occurring inside the composite powder particles at differing temperatures. Further discussion of the phase transformations occurring inside the powder, and the resulting sintered microstructures, will be provided in Section 5.3.4.

As noted earlier, after the synthesis stage was completed, subsequent milling processes were employed to reduce the final powder size. In the case of ball milling for 24 hours, the process also *appeared* to promote a degree of mechanical alloying within the powder, as indicated from the increasing Ti_3Al major peak (Figure 5-4). However, besides the potential phase transformation in the layered structures within the powder, the Ti_3Al peak growth in the XRD might also be contributed from a greater degree of revealing of the internal Ti_3Al structure after the particles were further milled. On the other hand, when the powders were milled and more strain was introduced in to them, the XRD peaks evidently broadened relative to the as-synthesised powder. Similarly, the Ti_3Al peak growth and broadening phenomena also occurred with both the attrition and shatterbox milling processes. In the last processing stage (i.e. heat-treatment at 1300°C), a greater amount of the Ti_3Al phase had formed, and a clearly two-phase γ-TiAl/α_2-Ti_3Al mixture was developed. In addition, prolonging the sintering time to four hours further promoted formation of the Ti_3Al phase. Based on these results, the Ti_3Al phase develops under more equilibrium conditions, presumably disassociating from the TiAl when the lamellar structure was forming (discussed in more detail in Section 5.3.5.2)

5.3.2 Milling Processes Comparison

As outlined in the experimental procedures (Figure 5-1), a variety of milling processes were performed on the synthesised compacts to acquire finer powder sizes. The effectiveness of each grinding process was evaluated by its ability to reduce the particle size. Figure 5-5 highlights the median particle size (D_{50}) resulting from the respective grinding processes. The particle size of the hand ground powder (D_{50} = 113 μm) is also included as a reference. For 30 minutes of milling time, shatterbox grinding (SBL with 1 wt-% Licowax®) achieved the finest powder size, showing the best process efficiency. However, the effectiveness of the shatterbox milling gradually deceased as the milling time increased from 30 minutes to one hour (figure not shown). The use of the Licowax® processing agent proved to be helpful, although the prealloyed TiAl powder would not be expected to be ductile and there should not be any obvious cold welding effect [101]. The optimal amount for the Licowax® addition was also confirmed to be below 1.5 wt-%. In comparison, use of the small shatterbox system was far less efficient compared to the large shatterbox due to its significantly reduced grinding momentum. In terms of application, the shatterbox milling step was a relatively simple approach and required no suspension medium or drying stage, in comparison to the wet methods (discussed below). However, the heat generated during milling might raise concerns of fire when a processing additive such as Licowax® is added, and considerable care should be taken to control the temperature during grinding.

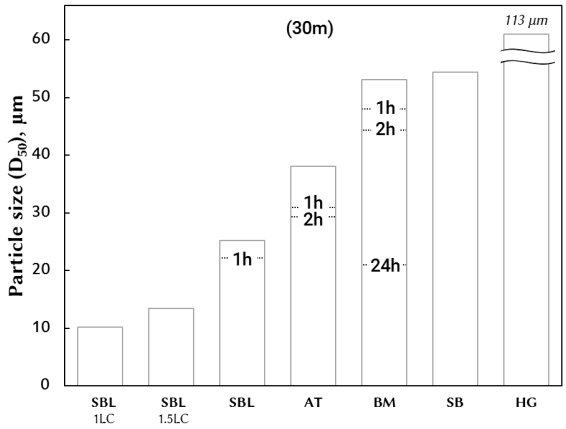

Figure 5-5. Particle size (D_{50}) after various grinding processes, conducted for various times from 30 minutes up to 24 hours, including the results from the hand ground process. (HG: hand ground, SB: shatterbox, BM: ball milling, AT: attrition, SBL: shatterbox large, LC: Licowax).

In comparison, the two wet milling processes were noticeably less effective than the shatterbox milling (Figure 5-5). However, the solvent solution helps to maintain low temperatures, while the closed system allows long grinding times to be employed. Compared to ball milling, the attrition milling treatment was a more effective process for size reduction. With only two hours of attrition milling the powder size could be reduced in to the 30 μm range (D_{50}). Nevertheless, it was noted that the attrition milling efficiency also reduced significantly after two hours for the present configurations used in this work. Consequently, prolonging the milling time beyond two hours cannot be expected to generate further significant reduction. Adjusting other process parameters, such as the weight ratio or the type of ball media (e.g. alumina or zirconia) and the solution, may promote further grinding. For example, in this study it was found that the use of hexane, a relatively non-polar solvent, was not able to effectively suspend the particles in the slurry, which resulted in poor grinding efficiency for the parameters examined (data not shown). Conversely, in the ball milling process, hexane showed no such agglomeration issues and fine powder size (D_{50} ~20 μm) could be achieved. This might be the result of the ball milling process utilising a sealed environment, while the attrition mill is effectively 'open', such that evaporative losses are possible. However, it was not as effective in reducing the particle size when considering the amount of time needed. The 24-hour milling was

assessed solely for comparative purposes. Moreover, longer operation time would introduce more contamination from the atmosphere in the milling container, the suspending solution or the milling media.

For the TiAl alloys, minimising the levels of carbon, oxygen, hydrogen and nitrogen is particularly crucial, as those elements have significant influence on the resultant mechanical properties [102]. Table 5-2 highlights the impurity concentrations determined for selected milling processes. In order to compare the various milling methods with different process times, the impurity results are normalised to their grinding time as well as to the hand ground (HG) reference levels.

Table 5-2. Impurity concentrations (and associated normalised levels*) of carbon, hydrogen, nitrogen and oxygen after the various processing stages. Sintering of the BM-24h powder was conducted at 1300°C for 2 hours.

	HG	SB-30m	AT-1h	BM-24h	SBL-30m	SBL-30m 1LC	BM-24h (Sintered)
Carbon, ppm	130	150 (2.3)	**370 (2.8)**	**1400 (0.4)**	640 (9.8)	**6100 (94)**	1000 (0.3)
Hydrogen, ppm	12	57 (9.5)	**150 (12.5)**	**380 (1.3)**	250 (41.7)	**1600 (267)**	67 (0.2)
Nitrogen, ppm	270	410 (3)	630 (2.3)	630 (0.1)	**16000 (118)**	1400 (10.4)	840 (0.1)
Oxygen, %	0.5	0.84 (3.4)	1 (2)	1.2 (0.1)	**2.4 (9.6)**	**4.6 (18.4)**	1.4 (0.1)

**normalised by milling hours and the HG reference, $(hr \cdot HG)^{-1}$*

In the shatterbox milling process, the powder interacts directly with the system atmosphere. As a result, the powder absorbed considerable amount of oxygen and nitrogen from the air; the presently available systems for this work do not have any mechanism for atmosphere control. Moreover, when compared with the small shatterbox system, the more effective grinding capability of the large shatterbox translated to more severe contamination during size refinement. In the test of processing agents, when Licowax® was added in the shatterbox milling, it is apparent that the nitrogen absorption was inhibited;

this observation likely arose from the formation of a wax coating on the powders. Nevertheless, the carbon and hydrogen levels increased significantly from adding the wax.

While the dry milling processes introduced a moderate amount of oxygen and nitrogen impurities, the powders milled by the wet processes were prone to carbon and hydrogen absorption. Although the use of an organic solvent (i.e. hexane or IPA) contaminated the powder, it also insulated the powder from the atmosphere and thus prevented major contamination by oxygen and/or nitrogen. After the milled powder (BM-24h) was sintered, both carbon and hydrogen impurities were significantly reduced through volatilisation (Table 5-2). Conversely, the oxygen and nitrogen very slightly increased, while likely arose from the sintering environment (tube furnace with following Ar). Alternatively, the interaction (i.e. ease of absorption) of Ti with these impurities can be considered from a thermodynamics perspective, besides the environment factors. Ti has the most negative enthalpy of formation with oxygen, followed by nitrogen, carbon and hydrogen [103]. Therefore, oxygen would react with Ti relatively easily, and consequently this resulted in the worst contamination in all the milling processes examined. Aside from oxygen contamination, the other impurities were in much lower concentrations, and the environmental conditions consequently had a greater impact on them.

Different milling processes resulted in various powder morphologies, as illustrated in Figure 5-6. As shown in Figure 4-10(a), the powder after being shatterbox (large) milled has a generally rounded shape. When the Licowax® processing additive was incorporated into the milling process, the milled powder was much finer and more irregular in shape, indicating that the powder underwent significant plastic deformation. Closer visual inspection revealed the powder appeared to be at least partially coated with the wax additive (Figure 4-10(b)). In contrast, the ball milled powder exhibits a flatter and more angular shape, while the attrition milled powder possesses both angular and rod- or plate-like morphologies (Figure 4-10(c-d)). The powder packing, compaction behaviour and the subsequent sinter densification will, of course, be affected by the powder morphologies. However, the influence of the powder morphology on sintering was not investigated in the present study.

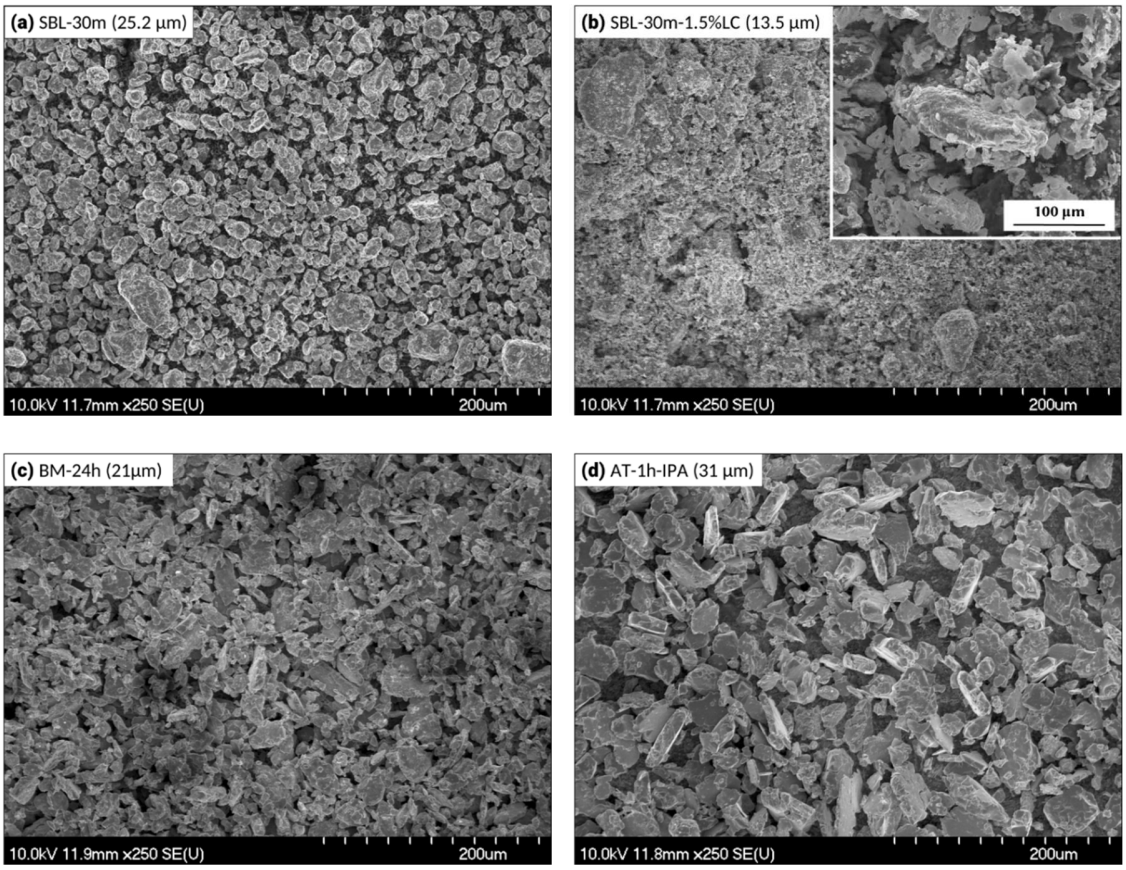

Figure 5-6. Typical SEM micrographs of the ground powders: (a) shatterbox milled for 30 minutes, (b) shatterbox milled for 30 minutes with 1.5%LC, (c) ball milled for 24 hours, and (d) attrition milled (in IPA) for one hour.

5.3.3 Powder Size Effects to Sintering Behaviours

In this section the pressing response and sintering behaviour of the milled powders are investigated. The pre-alloyed powder consisted of intermetallic phases and therefore the powder was hard to deform. The use of a hard and brittle powder could be beneficial in milling, as it is less likely to agglomerate and a smaller ultimate particle size could be achieved. However, the rigid pre-alloyed powder was difficult to compact into 'green' samples, because there was relatively minimal powder deformation and interlocking between the particles. As a result, the green strength was relatively low, while the green density was generally in the range of 60% of theoretical (e.g. BM-24h powder, green density = 61.73% ± 0.32%). In terms of a PM process, the relatively low green density may hinder the diffusion in the subsequent sintering process.

As mentioned previously, the use of a pre-alloyed Ti-48%Al powder assures a solid-state diffusion mechanisms during the sintering process, due to the absence of a molten aluminium liquid phase. In this case, the particle size is crucial in terms of contact points/area and related diffusion, and consequently the sample densification. In addition to a reduction in powder size, each of the milling processes can also be expected to introduce a considerable amount of crystal defects (e.g. dislocations, vacancies and associated strains) to the individual grains; this is evidenced in terms of the XRD peak broadening (Figure 4-9). Consequently, better densification was generally expected from using finer powders, due to shorter diffusion distances, a greater concentration of contact points and the higher energy stored in the particles. With this in mind, Figure 5-7 shows that the sintered density increases with finer particle size, regardless their milling processes. However, as the particle size was reduced to below 30 μm, there was generally no distinct improvement in densificaiton at the same sintering condition (1300°C, 2h), suggesting that factors other than size were restricting the densification. When the samples were sintered for a prolonged period (i.e. four hours), substaintial sintered density improvement to 88.4% was achieved. Essentially th same level of density (88.5%) was also attained when increasing the sintering temperature to 1350°C for the finer 10 μm powder (SBL-30m-1LC) samples. From the above results, it is clear that the main sintering conditions used currently (i.e. 1300°C, 2h) lacks sufficient thermal activation and time for complete diffusion. As a consequence, raising both the temperature and sintering time are considered necessary for achieving higher densification.

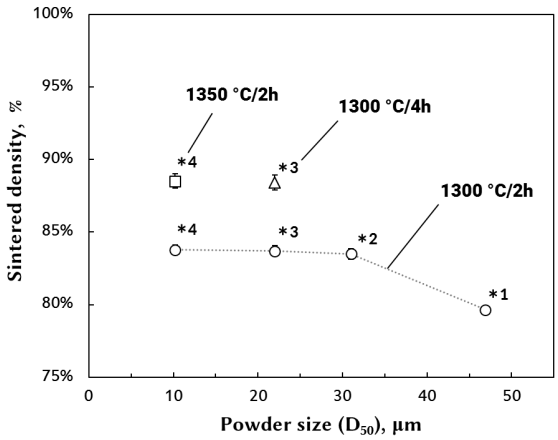

Figure 5-7. The effects of particle size on the sintered density. Various powder sizes were acquired form different milling processes (1: BM-24 (HG), 2: AT-1h, 3: BM-24, 4: SBL-30m-1LC).

The particle sizes affected not only the sample densification, but also influenced the resultant sintered microstructures. Figure 5-8 highlights a significant difference in the microstructure obtained from sintering both coarse and fine powders. Here the coarse powder (D_{50} = 46.9 μm) was obtained from grinding the pre-alloyed material by hand, followed by ball milling for 24 hours, whereas the fine powder (D_{50} = 21 μm) was achieved by initially shatterbox milling for 30 minutes, followed by the same ball milling step for 24 hours. The sintered sample prepared using the coarse powder shows a more porous structure, and a core structure within the grains (Figure 5-8(a)). In contrast, the sample sintered using the finer sized powder is denser, and does not exhibit the core structures, as shown in Figure 5-8(b). Detailed discussion on the formation of the respective microstructures will be given in Section 5.3.5.

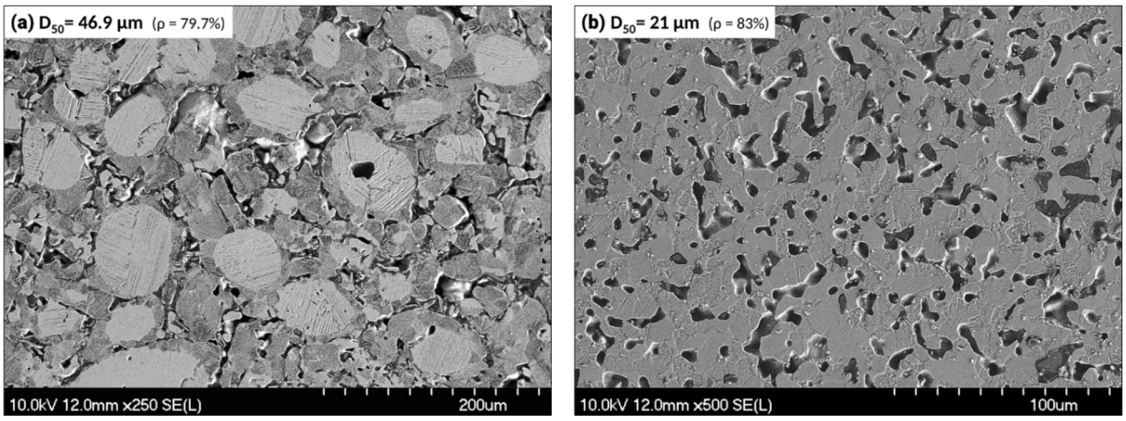

Figure 5-8. Representative SEM micrographs showing the effects of particle on the sintered (1200°C/2h) microstructure of the titanium aluminide samples, using: (a) coarse and (b) fine starting powders.

5.3.4 Powder Internal Structure Formation

The sintered microstructure was greatly influenced by the initial powder, as shown previously in Figure 5-8. As a consequence, before discussing the sintered microstructures it is crucial to understand the mechanisms of powder structure formation. Based on the present observations a reaction model between the Ti and Al powder is proposed, which illustrated in . It should be noted the proposed model considers reactions under the non-equilibrium conditions, while in the previous section 5.3.1, the XRD results exhibit the consequent phases after respective processes (i.e. samples cooled to room temperature). The sequence of phases that are generated during sintering is:

(1) $Ti + Al \rightarrow TiAl_3$
(2) $TiAl_3 + Ti \rightarrow TiAl$
(3) $TiAl + TiAl_3 \rightarrow TiAl_2$
(4) $Ti + TiAl \rightarrow Ti_3Al$

Initially, Ti reacted with Al to form the $TiAl_3$ phase, which has the lowest free energy at all temperatures in comparison with the TiAl and Ti_3Al intermetallic phases, as shown in [99,104]. This reaction can be expected to be rapid, due to the use of small Al powder (D_{50} = 6.4 µm), which could facilitate solid-state diffusion with the Ti powder at temperatures below the Al melting point. In addition, the occurrence of Al melting during heating would promote rapid diffusion rate for Al. Although the small Al powder might

diffuse into the Ti readily, even before any 'massive' melt formed, the DSC experiments (cooling curves) detected a small amount of Al melt at around 665°C when using identical raw materials and heating parameters. Therefore, even with a very fine Al powder, there would be a liquid phase (i.e. an Al-based melt) during sintering. Furthermore, the limited Ti solubility (< 2-3% Ti) in Al ensures that Al was the dominant diffusion species during the early diffusion stage.

Once all Al has diffused and reacted with the Ti (in atomic terms, three times more Al is required in comparison to Ti, to form $TiAl_3$), the $TiAl_3$ would begin to react with Ti and develop into the TiAl phase [104]. The intermediate $TiAl_2$ phases could grow subsequently as they require the existence of TiAl phase [105]. As more Ti diffused out of the core, the intermediate $TiAl_2$ layer continues to form until the outermost $TiAl_3$ layer eventually disappears ((d)). In the meantime, the Ti_3Al layer may develop as well. Nevertheless, it has been suggested from the free energy information and XRD analysis (Figure 4-9), that the Ti_3Al phase appeared later in the heat treatment process, at higher sintering temperature and longer time. It is interesting to point out that in spite of the TiAl phase having a lower free energy than Ti_3Al only below 500°C, the material (sintered at 640°C) consisted of predominately TiAl, based on the XRD and SEM results, indicating that the TiAl phase forms rapidly, and how dynamic (non-equilibrium) the reaction is in a powder sintering process. (d) shows a schematic of the likely resultant powder structure at 640°C. As the sintering temperature gradually increases ((e)), the extent of the equilibrium Ti_3Al and TiAl phases continues to increase before the eutectoid reaction, occurring around 1120°C. At the targeted sintering temperature (i.e. 1200 or 1300°C), the Ti_3Al and TiAl phases should undergo the eutectoid reaction and transform to the α phase if adequate reaction time is given. However, as the material slowly cools down after the heating process, the α phase would transform back to the Ti_3Al and TiAl phase combination.

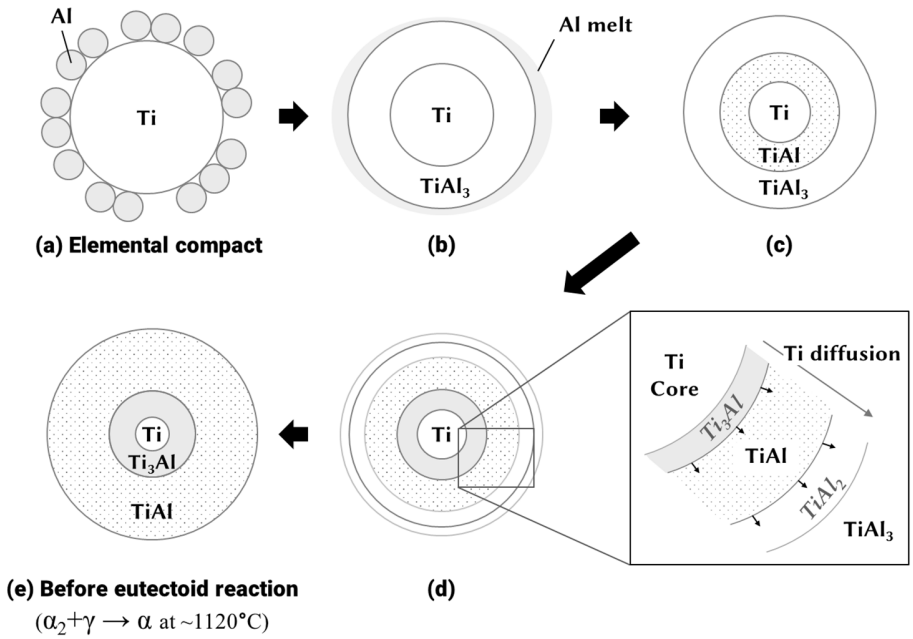

Figure 5-9. A simple schematic representation of the layered structure formation mechanism in elemental Ti and Al powder sintering.

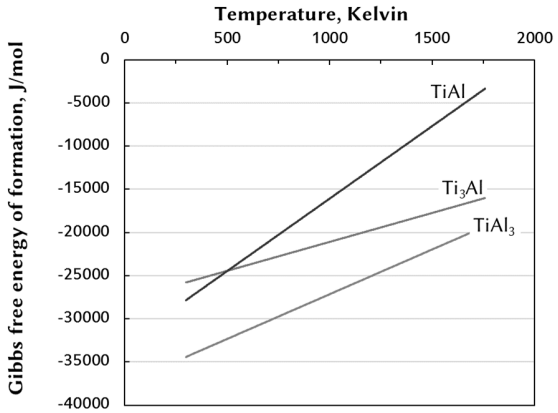

Figure 5-10. The change in Gibbs free energy of formation, as a function of temperature, of the Ti-Al intermetallic phases (figure drawn using equations from [104]).

Under the present (slow) sintering conditions, there may still be a Ti-concentrated core in the powder. Despite that, the XRD analysis did not show any clear Ti peaks, which

are not expected to exist after the powder sintering process; a very small fraction of residual Ti (~90% Ti by WDS analysis in the EPMA) was observed in the core of the synthesised powder as demonstrated in Figure 5-11. The outer layer of the powder was identified as TiAl via WDS analysis, followed by a middle layer of Ti_3Al, and a small core of Ti-rich material. As discussed in Section 5.3.1, considerable decrease of the main Ti_3Al XRD peak occurred when the heat treatment temperatures increased from 640 to 1200°C. Here, with the layered powder structure (Figure 5-11), a likely explanation is that as the reaction progresses, more powder surface ($TiAl_3$) transforms to the TiAl phase. In the later attrition stages, the powder was refined down in size and the internal structure (i.e. phases) was revealed. As a consequence, the XRD relative intensity of each phase more accurately reflected their volume fraction in the powder batch.

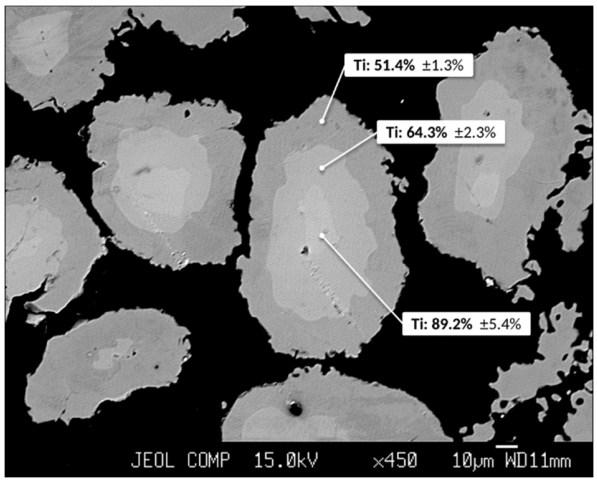

Figure 5-11. Cross sectional backscattered electron SEM micrograph of the initial manufactured powder (1200°C, 2h, hand ground).

5.3.5 Microstructure Characterisation

5.3.5.1 Coarse powder sintering

In the previous section, the formation of a layered structure in the powder has been discussed. Such inhomogeneity in the powder consequently led to a cored structure after sintering, when employing coarser feedstock powders (Figure 5-8(a)). In this section, the

sintered microstructure is analysed and a basic sintering mechanism model is proposed to explain the experimental observations (Figure 5-12). In the green compacts (i.e. the pressed (coarse) synthesised powder), the outer layer (TiAl) of a particle bonds with other adjacent particles at the beginning of sintering, through fundamental diffusion-based consolidation. As the sintering proceeds, the Ti-rich core (including the Ti_3Al) in the powder developed evidently into a lamellar structure. The high Ti concentration core gradually diffuses outwards until it disappears. Figure 5-13(a) shows a residual Ti-rich core after sintering. During sintering, many lamellar areas might be on contact (Figure 5-13(b)) and they gradually evolve into domains, which are areas containing laths in the same direction. As a result, a lamellar grain may consist of several domains. With the current slow heating and cooling rate, the lamellar structure can grow considerably (> 100 μm in diameter), and the smooth boundaries (growth front) that are formed are also the result of slow atom mobility [106]. In addition, some lamellar phase was also found to have nucleated at the particle boundaries.

Further analysis on the lamellar structured regions revealed not only the parallel lamellar laths, but also the fact that there appears to be two lamellar morphologies (i.e. fine and coarse laths), as seen in Figure 5-14(a). However, microstructural and composition analyses indicate that the two features were likely the result of different crystalline orientations. When analysing the compositions by EDS or EPMA, it was difficult to precisely measure the individual fine lamellar laths. Closer examination of them indicated the 'smoother' lath (area A in Figure 5-14(b)) had slightly higher Ti (+3%) than area B. Nevertheless, the compositional difference is clear between the lamellar structure (~58% Ti, α_2/γ phase) and the surrounding rim (~46% Ti, γ phase).

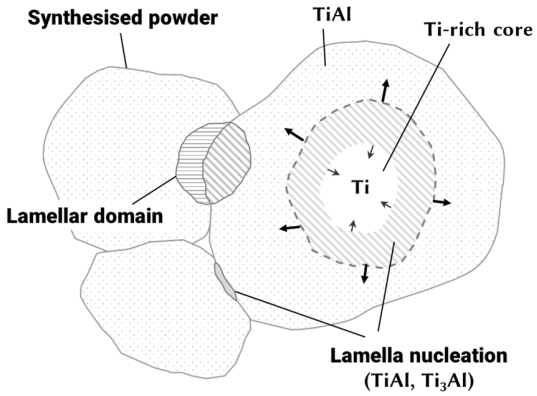

Figure 5-12. A simple schematic representation of the lamellar structure formation mechanism.

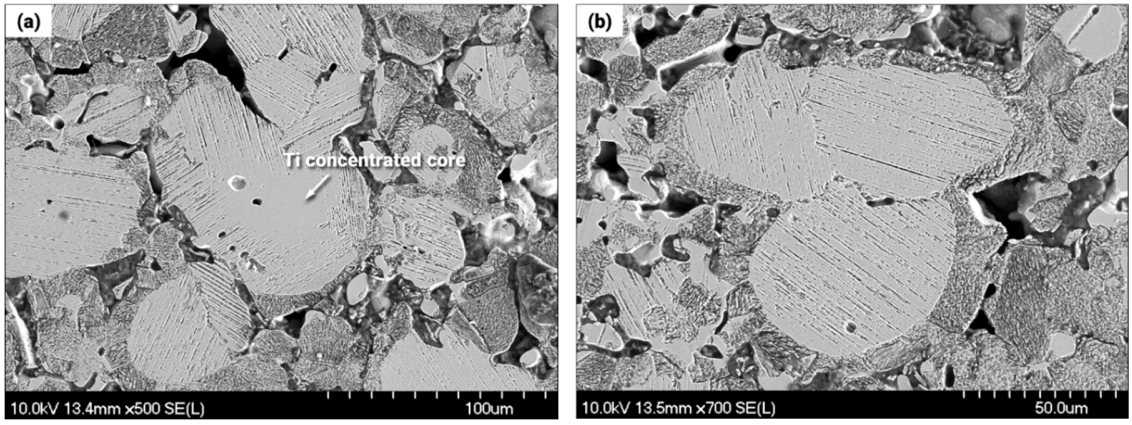

Figure 5-13. Representative SEM micrographs showing: (a) Ti concentrated structure remaining in the grain, and (b) lamellae grains combined to form domains of a larger lamellar region. Samples were sintered at 1300°C for 2 hours using coarse powder (D_{50} = 46.9 µm).

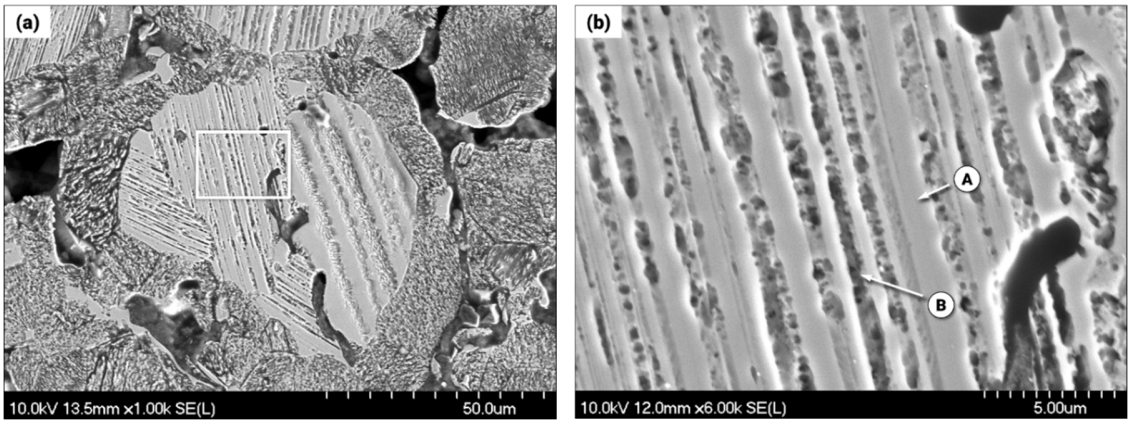

Figure 5-14. Representative SEM micrographs showing: (a) lamellar features with two different widths, and (b) closer inspection in the inset region in (a), showing the detailed lamellar lath structures. Samples were sintered at 1300°C for 2 hours using coarse powder (D_{50} = 46.9 µm)

5.3.5.2 Milled powder sintering

When the synthesised powder was further milled by the means outlined in Section 5.3.2, the layered structure was further broken down and fragmented, resulting in a more uniform spatial distribution of each of the phases. Consequently, the core structure was not observed in the sintered samples prepared with the finer powder. Instead, three morphological features are generally distinguished in these samples, as indicated in Figure 5-15. Areas A and B show 'roughened' morphologies, while area C has a smooth surface. The samples sintered at 1300°C for either two or four hours generally have similar microstructural features, but the phases have some measurable variations in composition (Table 5-3). In Figure 5-15 (sample sintered at 1300°C for 4h), area C is identified as single-phase γ-TiAl, while areas A and B are in γ-TiAl/α_2-Ti_3Al two-phase composition region. Although the morphologies between areas A and B are noticeably dissimilar, area A is generally exhibits no significant difference to area B in terms of the composition (with only small fluctuations). Similar to the two lamellar features in the previous section, the difference between the two etched surfaces is believed to be merely due to different crystalline orientations. Nonetheless, in both areas A and B there were some regions attributed to very specific Ti:Al ratios for both phases. When comparing the samples sintered at two hours with those prepared at four hours, this atomic ratio became more clear. A high fraction of locations specifically consisted of ~60% Ti, and this ratio suggests a

3TiAl:1Ti_3Al phase combination. Based on this observation, in the materials sintered for a longer time, the areas of type A and B gradually transform to a lamellar phase, whereas the type-C areas remain at ~51%Ti (i.e. γ-TiAl phase). In comparison to the cored structure in samples sintered using the coarse powder, the sintered microstructures of the fine powder samples eventually evolved to a duplex microstructure that consisted of γ-TiAl (i.e. area C) and γ-TiAl/α_2-Ti_3Al (i.e. areas A and B) phase configurations.

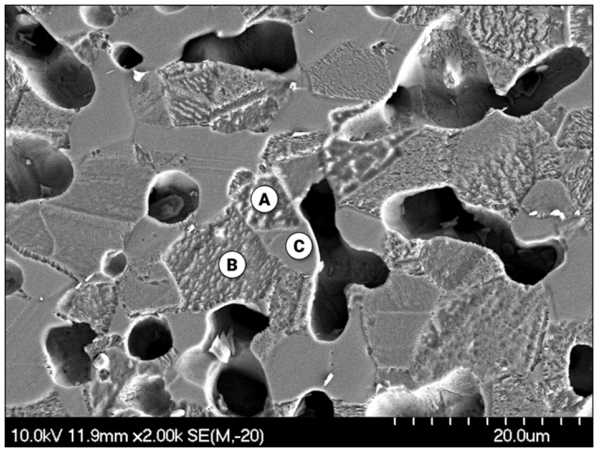

Figure 5-15. Phase features of the sample sintered at 1300°C for 4 hours, using the BM-24h starting powder.

Table 5-3. Titanium concentrations (measured in at.-%) within the different phase regions of samples sintered using either coarse or fine power, prepared at 1300°C for 2 or 4 hours.

	Powder	Density	Lamellae / A, B	Rim / C
1300°C, 2h	Coarse (HG)	79.7%	57.7 ±2.5	46.1 ±4.1
1300°C, 2h	Fine (BM-24h)	83.7%	50.3 ±2.1	51.3 ±4.4
1300°C, 4h	Fine (BM-24h)	88.4%	55.8 ±5.0	51.6 ±4.0

5.4 Conclusions

In the present study, an economical pre-alloyed TiAl powder was produced using elemental powder blends. This 'in-house' manufactured powder was subsequently sintered, resulting in considerably improved densification compared to sintering elemental Ti-Al

blend, as any swelling problems were avoided. Smaller particle size was beneficial in terms of sample densification, regardless of the milling methods that individual powder blends experienced. However, the size effect was less noticeable when the powders exhibited sizes below 30 μm. Sintering parameters were briefly investigated and it was noted that the current sintering conditions (1300 °C for 2 hours) was insufficient to achieve full densification. Higher sintering temperatures or longer sintering times will be needed in order to achieve further improved densities. Nevertheless, other process factors that might hinder densification should be also investigated. For example, the effects of powder contamination and methods to produce a cleaner powder.

The intermetallic phase transformations were found in the order of $TiAl_3$, TiAl, $TiAl_2$, Ti_3Al during the elemental powder blend sintering. Eventually the powder possessed a complex, cored structure, with phases from the outer layer to the core: TiAl, Ti_3Al and (occasionally) residual Ti. In the case of sintering a coarse precursor powder, combined with slow heating and cooling rates, it allowed observation of the lamellar structure evolution, which involved nucleation at the particle boundaries, grain growth along with the Ti diffusing out of the concentrated core, and grain merging to form domains. When sintering the milled powders, the compositional change suggested Ti aggregated to the lamellar phase while the microstructural morphologies remained generally unchanged. With higher sintering temperature or longer time, a higher fraction of well-defined 3TiAl:Ti_3Al ratios occurred in the lamellar phase.

Acknowledgements

The authors would like to thank the Natural Science and Engineering Research Council of Canada (NSERC) for their financial support of this research through the Automotive Partnerships Canada (APC) program. We would also like to thank Wescast Industries Inc. and Kingston Process Metallurgy Inc. for their financial, in-kind and technical support. The support of the Canada Foundation for Innovation, the Atlantic Innovation Fund, and other partners who helped fund the Facilities for Materials Characterisation, managed by the Dalhousie University Institute for Materials Research, are also gratefully acknowledged.

Chapter 6. Densification Behaviour and Microstructure Evolution of Ti-48Al Consolidated by Spark Plasma Sintering

(submitted to Journal of Materials Science, June 2016)

Hung-Wei Liu, D. Paul Bishop and Kevin P. Plucknett*

Materials Engineering, Department of Process Engineering and Applied Science, Dalhousie University, 1360 Barrington St., Halifax, Nova Scotia, CANADA

Abstract

Spark plasma sintering (SPS) is a fairly novel powder metallurgy (PM)-based process. Compared to more traditional PM processes, SPS technology provides greater sintering efficiency for the Ti-48Al alloy, due to its fast heating and cooling rates, combined with an applied pressure and electric field during the process. In this study, three fundamental processing factors (i.e. sintering temperature, time and particle size) are investigated, and their effects on densification, hardness, and phase transformations are studied. Three grain morphologies were found in the microstructures, present in different ratios in the samples, depending on the sintering parameters. A model is proposed to explain the (α_2) grain phase growth and the transformation of two types (fine and coarse) of lamellar structural development. The pore configurations (i.e. size and quantity) are examined, and their interactions with the phases, which suggests the phase formation sequence and sintering state, are also discussed.

Keywords

powder metallurgy; γ-TiAl; α_2-Ti_3Al; hardness; Ostwald ripening; scanning electron microscopy

*kevin.plucknett@dal.ca

6.1 Introduction

Titanium aluminide (γ-TiAl) based alloys have attracted considerable interest from the aerospace and, more recently, automobile industries due to their low density, and high retained strength and oxidation resistance at elevated temperatures (>500°C) [91]. Those properties make TiAl an excellent material to replace the much heavier Ni-based superalloys for engine applications [16]. Several TiAl alloys have been developed in the past few decades, such as the Ti-48Al-2Cr-2Nb (GE) alloys, developed for low-pressure turbine applications [92,107] and the Ti-43Al-4Nb (TNM) alloys for sheet components [108–111]. However, TiAl alloys generally suffer from low ductility particularly at room temperature, and thus they are difficult to manufacture when using more conventional thermomechanical processes. Consequently, the production cost is high and the applications of TiAl alloys are greatly restricted. Many near-net shape approaches, which can considerably minimise the need for post-machining, have been investigated to overcome the poor workability of the material [20,112,113]. Among them, powder metallurgy (PM) based processes can provide a cost-effective route, and do not possess the common concerns relating to compositional segregation during the casting process [114].

One PM approach that has shown great potential in recent years is the spark plasma sintering (SPS) process [115–118]. This novel technology utilises a pulsing on-off DC current, and applies pressure to the powder simultaneously. For conductive powders, the electrical current flows through the material and heat is generated due to the Joule effect [37,119]. The heating occurs between the particle contact regions, where the electrical resistance is the greatest. As a result, the SPS technique provides considerable localised and thus very efficient heating for metallic powders. Furthermore, because of the nature of the applied current, the SPS process also heats and cools very rapidly, and hence grain growth can be significantly reduced. Very fine sintered microstructures, with grain sizes from a few microns down to hundreds of nanometers, can be retained when using nano-scaled starting powders [120]. It is consequently possible to achieve comparable sintering results to more conventional methods, while using lower sintering temperatures and shorter holding times. For TiAl-based alloys, the sintering temperature is generally in 1100-1300°C range, which is held for less than 10 minutes in a SPS process. In comparison, the

conventional hot pressing method typically requires a hold time of 1 to 2 hours at, or even above, 1300°C [107,121]. Besides the thermal effects, it has also been demonstrated that the electrical field generated from the current also imposes pronounced influences on mass transportation during sintering. Munir and colleagues have published a detailed review discussing the field effects in the SPS process that relate to these phenomena [43].

In early TiAl PM research, using the pressureless press-and-sinter method, several works have demonstrated significant swelling in the samples when sintering elemental Ti and Al blends. Although some SPS investigations were conducted using the more economical blended elemental route successfully (with Ti and Al elemental mixtures), Kirkendall porosity and compositional inhomogeneity were still prevalent [88,122]. Moreover, further studies using SPS or hot pressing approaches, have reported that the Al melt can be squeezed out of the powder mixture when sintering elemental Ti and Al blends [97,107]. Therefore, in the present study, a pre-alloyed TiAl powder was initially produced in-house for the SPS assessment. The pre-alloyed TiAl powder was produced by pressureless heat-treatment of an elemental Ti and Al blend, and the partially sintered porous products were crushed and milled to a refined particle size and then used as the precursor powder for the SPS investigation.

The present study reports upon the fundamental sintering responses of a γ-TiAl/α_2-Ti_3Al alloy powder using the SPS approach. The effects of processing parameters (i.e. temperature, time, particle size) on the sample densification were studied, and the sintered microstructures were analysed, with an emphasis placed on the phase formation and evolution, and the relationship of porosity with other phases in the materials.

6.2 Materials and Methodology

The pre-alloyed Ti-48Al (all compositions are given as atomic percentage, unless stated otherwise) powder was prepared in-house using elemental raw powders, specifically a sponge titanium powder (-100/+325mesh; ADMA Products Group, Hudson, OH, USA), and an aluminium powder (Grade DG20; Ecka Granules, Fürth, Germany). The elemental blend was initially pressed into discs, and subsequently heat treated at 1200°C for 2 hours

in a tube furnace (Model STT-1600C, SentroTech, Stronsville, OH, USA) under constant argon flow. The heating and cooling rate were controlled at 5°C min^{-1}. The cooling rate decreased to a natural furnace cool when the temperature dropped below ~200°C. The heat treated discs were then roughly crushed using a manual press. Further grinding was conducted within a 250 ml alumina bowl on a shatterbox mill (Model TM/MAX2, TM Engineering Ltd., Burnaby, BC, Canada) operating at 950 rpm, for between 90 and 600 seconds. The particle size distributions were measured using a particle size analyser (Model Master Particle Sizer 20600, Malvern Instruments, Malvern, UK).

Once the powder was prepared, a ~6g batch was loaded into a graphite die set, which consisted a 20 mm diameter die with an upper and lower punch. Graphite foil was used to cover the die interior and the punch surfaces prior to powder loading to minimise potential reaction with the die set itself. The die set was subsequently loaded into the SPS system (Model SPS Model 10 Series, Thermal Technology LLC, Santa Rosa, CA, USA) to consolidate the powders. To ensure no residual air in the chamber, the SPS furnace was evacuated and back-filled with argon twice. When the vacuum was suitable ($< 2 \times 10^{-2}$ torr), the sintering process was performed at temperatures ranging from 800 to 1300°C, with an isothermal hold time from 0 up to 10 minutes. A pressure of 50 MPa was applied to the sample during the heating process. The current and voltage of the SPS process was automatically controlled by the system computer to follow the heating scheme. The heating and cooling rates were controlled at ~100 °C min^{-1}. A pyrometer was used to monitor the temperature (effective at above 600°C). After the samples had cooled, the graphite foil was removed by light sanding to reveal the surface of the SPS processed samples.

The sintered density was subsequently determined using the oil immersion method, in accordance with ASTM Standard B328 (MPIF Standard 42). The specimens were then polished for microstructural analysis. Kroll's solution (2 ml HF, 6 ml HNO_3, 92 ml H_2O) was used to etch selected samples. The crystalline phases of the SPS densified samples were identified using X-ray diffraction (XRD; Model D8 Advance, Bruker Instruments, Madison, WI, USA). The microstructures were examined using an optical microscope (Model DP-71, Olympus Corp., Tokyo, Japan), with differential interference contrast (DIC) imaging, or a scanning electronic microscope (SEM; Model S-4700, Hitachi High Technologies, Tokyo, Japan). The SEM was operated in either combined secondary

electron (SE)/backscattered electron (BSE) mode, or with a negative bias to limit the imaging mode to BSE. Local compositions of phases were determined using an energy-dispersive X-ray spectroscopy (EDS; Model Inca X-MaxN, Oxford Instruments, Concord, MA, USA) in the SEM or a wavelength-dispersive X-ray spectroscopy (WDS) in an electron probe micro-analysis system (EPMA; Model JXA-8200 Superprobe, JEOL, Tokyo, Japan). Carbon content was measured using a carbon/sulphur analyser (Model Eltra CS-2000, Eltra GmbH, Haan, Germany). The pore size (Feret diameter) and the area fraction statistics were measured and compiled using optical images and the analysis software ImagePro 6.3 Plus (MediaCybernetics, Rockville, MD, USA). Each data set was comprised of more than 500 measurements. The hardness characteristics of the sintered samples were measured using a Rockwell hardness tester using the HRA scale (Model Wilson® Rockwell 2000, Buehler Corporation, Lake Bluff, IL, USA).

6.3 Results and Discussion

6.3.1 Material characterisation

The basic morphology of the fabricated Ti-48Al powder, after hand grinding, is shown in Figure 6-1(a). Cross-sectional examination of the powder revealed an internal 'core-rim' structure (Figure 6-1(b)). EDS analysis indicated that the core region contained a higher Ti concentration (~61%), while the surrounding rim area has lower Ti (~51%). The powder structure was formed as a result of elemental Ti and Al sintering. When the powder is milled using the shatterbox, this complex internal structure was broken down through attrition and the two phases were then expected to be well distributed in the resulting powder blend. The particle size distribution achieved after various milling times, in terms of the relative D_{50} value, is shown in Figure 6-2.

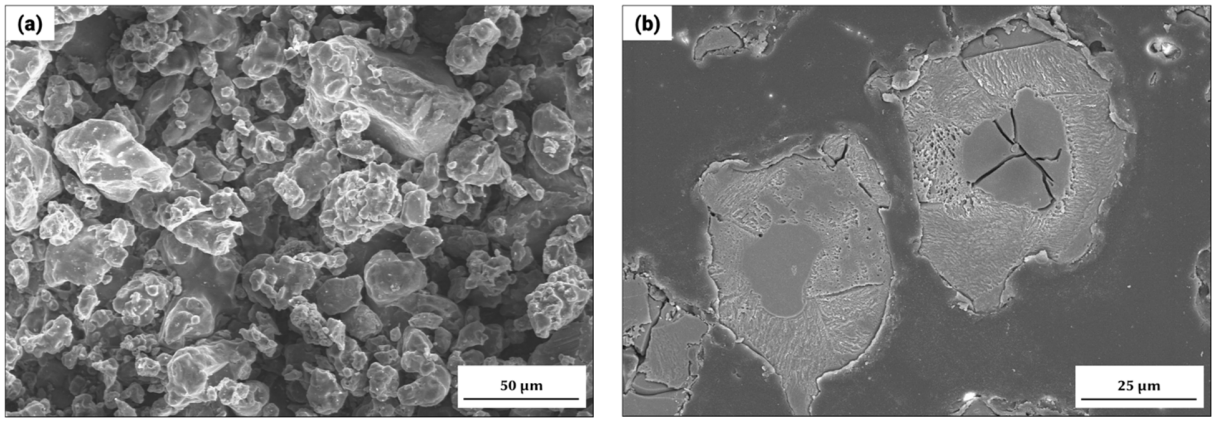

Figure 6-1. Morphology of: (a) the 'in-house' manufactured Ti-48Al pre-alloyed powder after hand grinding (combined SE/BSE image), and (b) the polished and etched cross-section of the powder (low negative bias BSE image).

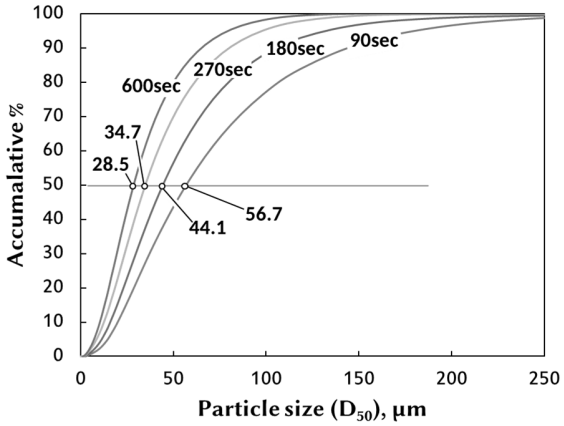

Figure 6-2. The measured particle size (D_{50}) of the Ti-48Al powder following various grinding times.

6.3.2 Densification, hardness and carbon contamination

In this set of experiments, the SPS process was only conducted using a 3 minute isothermal hold, and consequently the effects of temperature were specifically explored. Figure 6-3(a) demonstrates that, as might be anticipated, the powder densification response is strongly temperature dependent. Despite the short sintering time, almost fully dense material can be achieved with a 3 minute hold at 1300°C (98.9% of theoretical density), showing excellent efficiency for the SPS process. In contrast, from our earlier work,

samples conventionally vacuum sintered using a tube furnace only attained ~88% of theoretical density when using a 4 hour hold at 1300°C. In this respect the advantage of the SPS process is clear against more conventional sintering. Nevertheless, in a SPS study using a pre-alloyed (i.e. Ti-47Al) powder, full densification was achieved at noticeably lower temperatures (as low at 1000°C) than the present work [123]. The improved densification was potentially due to higher kinetics during sintering using the mechanically alloyed powder [123]. The milled powder had complicated shapes with more inner pores and defects, and the differences in morphology may contribute to different densification mechanisms. Guyon et al. consolidated two TiAl-based powders (an atomised powder versus one that was milled) using SPS, and they observed that the milled powder experienced a different deformation mode (grain boundary sliding assisted by surface/grain boundary diffusion) during densification, while for the atomised powder, heterogeneous deformation modes promoted by dislocation glide and twinning occurred [117]. In another SPS work, comparing various types of Ti powder (gas atomised, hydride/de-hydride, and sponge), the densification sequences were different for the respective powders and their sintered microstructures were distinctly dissimilar, although sintering of the individual powders all resulted in full densification after the process [124]. However, it should also be noted that the measured SPS processing temperature is actually directly on the die in most SPS systems, and hence not the true reaction temperature of the sample itself. This temperature difference can vary substantially, depending on the material [37]. The use of a pyrometer in the current experiments might also cause some differences in temperature measurement compared to other experiments conducted when using a thermocouple. As a consequence, direct comparison between SPS experiments using different facilities can be difficult.

In the present study, full densification might be realised if the sintering temperature was raised above 1300°C. However, sintering at 1300°C unexpectedly resulted an issue where part of the sample was bonded with the punch. It was speculated that some powder likely passed the graphite foil and became bonded with the contact surface of the punch. As a consequence, in order to continue the study, sintering temperatures higher than 1200°C were not considered further, in order to avoid potential damage to the equipment.

Although the present study did not fully investigate the mechanical properties of the SPS processed samples due to size limitations (20 mm diameter), their hardness properties were evaluated as a general indication. As illustrated in Figure 6-3(b), the hardness values of the sintered materials follow the general density trend. The values for the samples that are close to fully dense (i.e. those sintered at 1200 and 1300°C) are comparable to the values reported for a nominal TiAl cast material (despite the fact that the two-phase Ti-48Al is harder, due to the presence of Ti_3Al phase) [125]. Compared to a broadly similar composition (Ti-47Al) in another SPS study, the hardness values are higher than the present ones even at lower sintering temperatures, due to their higher sintered densities (their materials were nominally fully dense) [123].

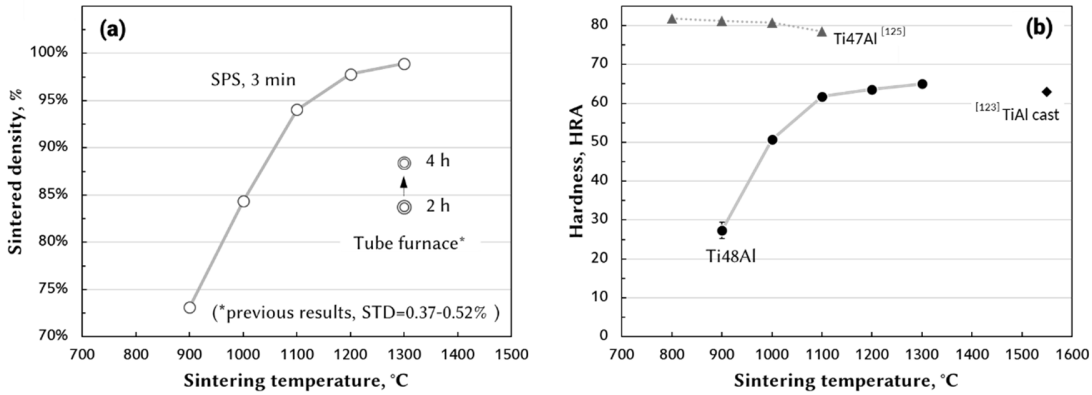

Figure 6-3. (a) The effects of SPS temperature on the density of the sintered samples, as a percentage of theoretical (standard deviation error = 0.18% at 1200°C). (b) The hardness of the sintered samples as a function of SPS processing temperature. The reference data are acquired from [123,125]. Note that the standard deviation errors for the Ti48Al samples were very small, and are only apparent for the porous 900°C processed sample.

Another important factor in a sintering process is the isothermal heating time. In the present study, a series of sintering experiments, using various hold times, were conducted with the sintering temperature maintained at 1200°C. Figure 6-4 illustrates the effects of sintering time on sample densification. It is clearly seen that although the density initially improves with time, there is no further improvement after 5 minutes hold. In comparison, Figure 6-4 demonstrates that the hardness decreases with increased hold time.

This observation can be ascribed to grain growth after the longer sintering times. Further details regarding the grain growth response will be discussed in the subsequent section. The current results suggest that a 3 to 5 minute hold is adequate, while a longer sintering time could be detrimental to the mechanical properties. As mentioned in the Introduction, the SPS process is generally conducted with a hold period of less than 10 minutes, and near fully dense TiAl-based alloys can be produced in this manner. Any excessive sintering time would promote unnecessary grain growth and impair the mechanical properties.

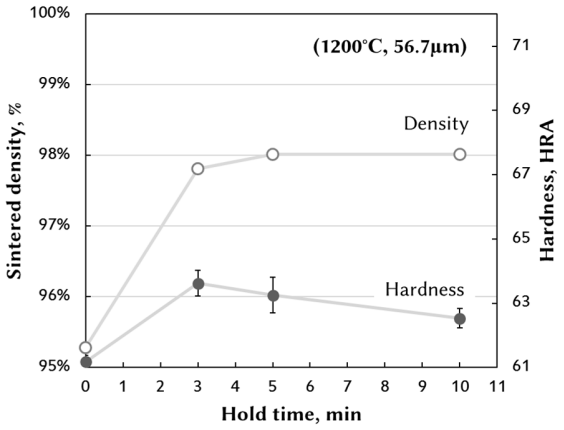

Figure 6-4. The effects of SPS hold time on the density, as a percentage of theoretical (standard deviation = 0.18% at 1200°C), and the hardness of the sintered samples as a function of SPS processing hold time.

As the sintering process is conducted in a graphite die, carbon contamination was anticipated, even though the sintering process was considerably shorter in duration when compared to other traditional, slower heating techniques (e.g. electric heating furnace). This is a common concern in any SPS process using a graphite die and punches. Table 6-1 lists the carbon concentration from the raw powders to the final SPS densified products. The carbon concentration was considerably increased when prolonging the sintering residence time in the SPS die. Formation of the titanium carbide (TiC) phase was identified by XRD analysis, although no clear titanium carbide phase was observed from SEM examination of the microstructure and associated EDS analysis. As shown in Figure 6-5, the sintered materials generally exhibit an XRD pattern showing a mixture of the γ-TiAl

and α_2-Ti_3Al phases, while two TiC peaks are also clearly distinguished. The formation and existence of the TiC might influence the mechanical properties of the TiAl alloy, but its effect is beyond the scope of the present study.

Table 6-1. Carbon concentrations at different processing stages.

	ppm
Elemental Ti/Al blend (raw)	53*
Pre-alloyed TiAl	65*
Shatterbox milled (90 seconds)	74*
Spark plasma sintered (1200°C/3 minutes)	183
Spark plasma sintered (1200°C/10 minutes)	675

**Measurement is close to the detection limit.*

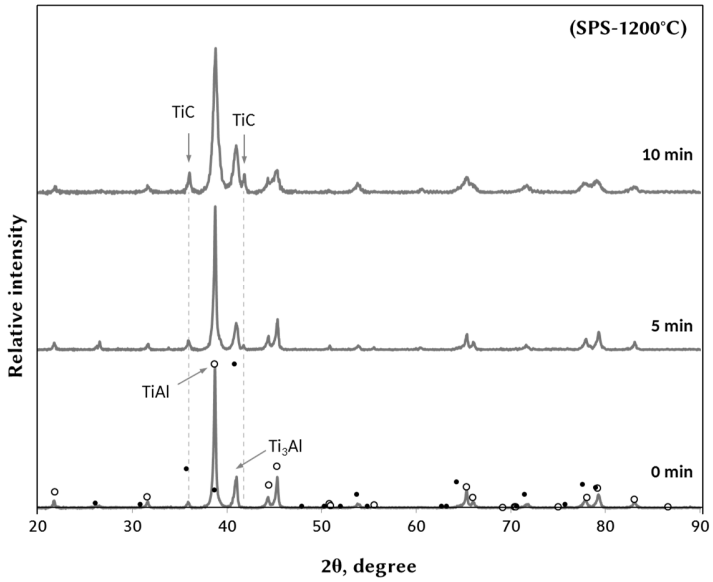

Figure 6-5. XRD patterns obtained for the Ti-48Al powders after different SPS hold times, showing increasing TiC formation with longer sintering time (1200°C sintered samples).

The present work also investigated the effects of Ti-48Al particle size on the SPS process. In solid state sintering a smaller particle size translates to shorter distances for diffusion, and a greater number of contacting points for bonding between particles. The present synthesised Ti-48Al powder was ground down to several different ultimate particle sizes in the shatter box mill, as previously outlined in Figure 6-2. As expected, a decreasing initial particle size resulted in better densification during sintering (Figure 6-6). Furthermore, use of the finer powder resulted in an earlier shrinkage onset, and the difference continued to increase until the peak temperature was reached, as demonstrated by the SPS ram displacement curves (Figure 6-6(b)). The two shrinkage curves for the same coarse powder closely overlap, indicating consistent measurements. Improved densification using the fine powder is likely to arise, at least in part, from a higher concentration of particle-particle contact points during the SPS process. The sample hardness also increased accordingly, as the sintered density was improved. However, longer grinding time would give rise to higher contamination from the grinding environment. There are significant measured increases in oxygen and nitrogen concentration from the atmosphere when conducting extended grinding for 30 minutes (data not shown). Although the grinding time was much shorter for the samples presented in the present work, contamination should always be minimised as much as possible. The outlined contaminating elements can be expected to be interstitially located in the alloy, and will most likely alter the mechanical properties.

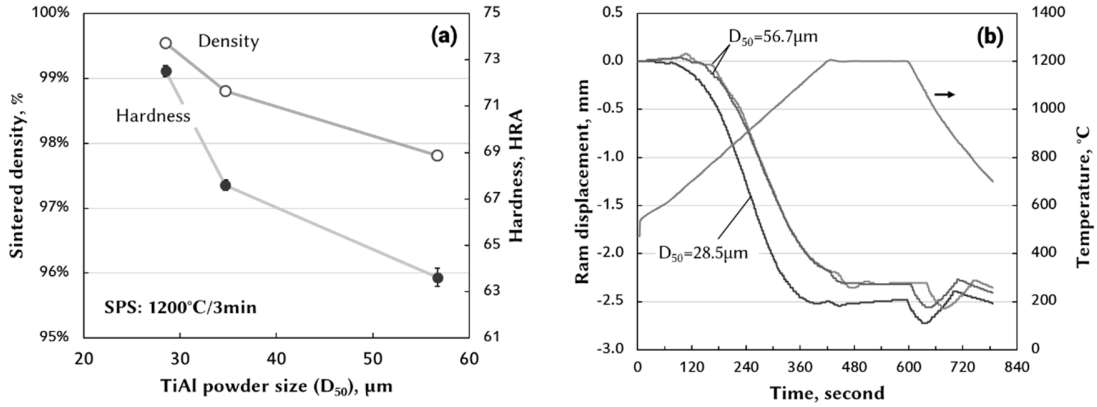

Figure 6-6. (a) The effects of Ti-48Al particle size on the sintered density (1200°C/3 min) and HRA hardness. (b) SPS densification curves (i.e. ram displacement) for the fine (D_{50} = 28.5µm) and coarse (D_{50} = 56.7µm) Ti-48Al powder through the sintering process; the reproducibility of the process is highlighted from the duplicate curves obtained with two coarse powder samples.

6.3.3 Microstructural analysis

6.3.3.1 Phase identification

Detailed microstructural analysis of the samples sintered at temperatures below 1300°C generally identified four phase categories following etching, as presented in Figure 6-7. The samples sintered specifically at 1300°C will be discussed in the next section as the microstructure is greatly dissimilar, due to a rapid diffusion mechanism. In Figure 6-7, the rounded grain includes a smooth surfaced core (region A), and a surrounding region (B) which exhibits a light impression of parallel lamellar lines. Some grains can contain the lamellar lines internally (Figure 6-10(a)), while other grains may only possess entirely A- or B-type features. Further away from this grain in Figure 6-7(a) is a 'roughened' area with several morphologies (identified as regions C1-3 and D). While the regions C1, C2 and C3 appeared to exhibit very dissimilar appearances, they exhibited very similar compositions. The morphological differences were therefore likely due to different crystalline orientations and the way these differing orientations responded to the etchant. On the other hand, area D appeared less rough in terms of the surface texture. The four categories were not only determined by the appearance, but also grouped based on their compositions. Figure 6-8 schematically illustrates the composition range for each of the groups on the Ti-

Al phase diagram, based on both the EDS and WDS results. The four features were distinguished as follows: (i) A - α_2 grain, (ii) B and C - α_2/γ two-phase area and (iii) D - γ phase. It was clear that the Ti concentration decreased moving away from the core to area B, and then region C, and it is the lowest in area D.

Although both regions B and C were in the two-phase range, they exhibit different morphologies due to differing γ:α_2 ratios. Area B contained more α_2 phase and had fine lamellar lines, whereas area C had more γ phase and showed a rougher surface. It was difficult to characterise the rough surface from the etched micrographs. However, from the lightly etched SEM micrographs (Figure 6-7(b)), a coarser lamellar structure is suggested within region C before it was severely etched. When comparing the lightly and regularly etched micrographs, the Ti rich regions were more resistant to the etchant; those regions (i.e. A and B) appeared smooth in the SEM, or bright under the optical microscope. Those findings suggest the γ phase exhibited a coarser lamellar structure and was more prone to etching (lower Ti content). The development and structure of the grains and the two-phase regions will be discussed in the following section.

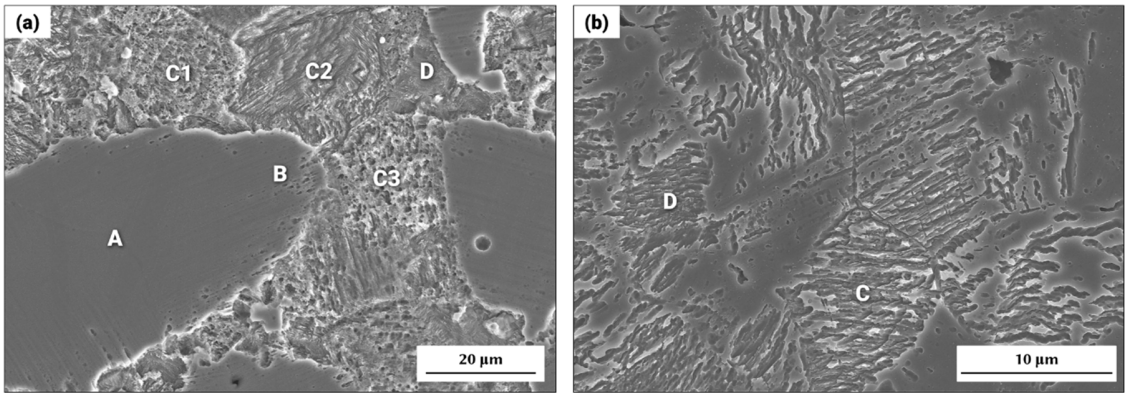

Figure 6-7. (a) SEM image highlighting typical phase features in a sample sintered at 1200°C/5min (combined SE/BSE image). (b) SEM image showing typical microstructural features for a lightly-etched sample sintered at 1200°C/3min (combined SE/BSE image).

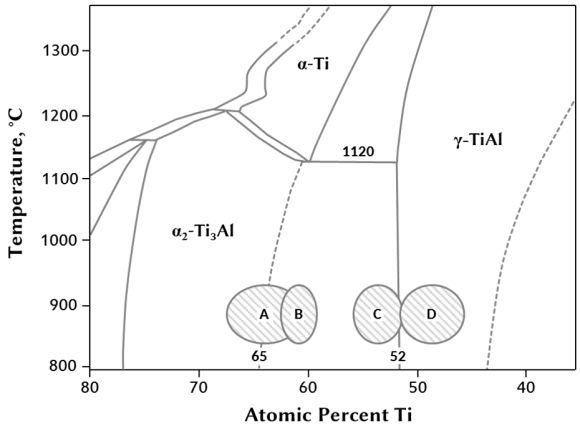

Figure 6-8. Schematic representation of the composition range for each identified microstructure feature; the section of the Ti-Al phase diagram is adapted from [8].

6.3.3.2 α_2 and lamellae phase development

As discussed previously, after processing at 1200°C the SPS processed material consisted of a combination of α_2 grains, the composite α_2/γ area, and the separate γ phase. The two basic phases constitute the microstructure in different ratios and forms, depending on the processing parameters: sintering temperature, time, and initial particle size. To analyse the evolution of α_2 grains, polished and un-etched optical micrographs were assessed. Although the grain size was not measured statistically, the growth and nucleation of grains was observed. In Figure 6-11(a-c), the grain size increases notably with increasing sintering time. Such grain growth was also confirmed by the α_2 peak growth in the XRD analysis (Figure 6-5). Furthermore, as discussed in Section 6.2, the apparent stagnation of densification with longer sintering time also suggested the conditions for grain growth had been reached.

With reduced initial starting powder size, the resultant α_2 grains were smaller (but present in a comparable concentration) in the sintered microstructure (Figure 6-11(d-f)). As noted earlier, the grain structure was, at some level, inherited from the powder. Consequently, when the particles were broken down further with longer milling time, more core (Ti-concentrated) fragments were exposed, which consequently developed into α_2 grains, dispersed uniformly in the sintered microstructure. When the starting powder was smaller, there was a higher concentration of particle-particle contact points, which could

promote nucleation of the α_2 grains. If sufficient sintering time was provided, those newly nucleated grains might still grow. Nevertheless, the amount of α_2 grains was ultimately governed by the overall composition of the material. From the Ti-Al phase diagram, the α_2 phase is less than 7 vol.% of the Ti-48Al material (the remainder being the γ phase) at room temperature. Besides the α_2 phase growth, more apparent grain growth was contributed from the α_2/γ (i.e. area B mentioned previously in Section 6.3.3.1) lamellae formation.

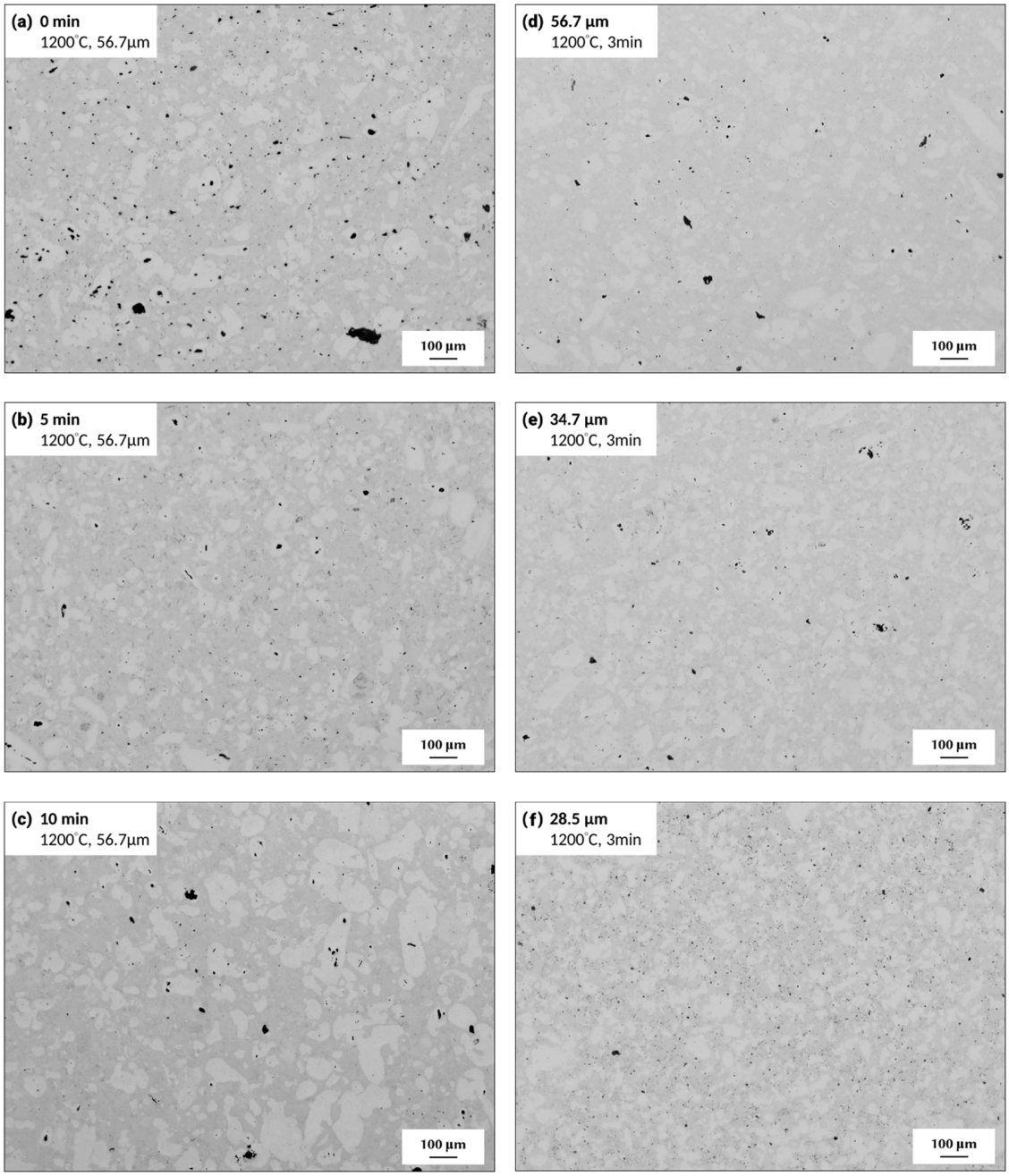

Figure 6-9. Representative optical micrographs of sintered samples processed using different sintering hold times, from 0 to 10 minutes (a)-(c); and particle size from 56.7 to 28.5 µm (d)-(f)

Assessing sintering temperature, the grains did not develop in size notably at the lower sintering temperatures, as there were still significant amounts of pores and densification was still predominant. Using optical DIC imaging, the internal structure within the grains was revealed more clearly. For samples processed at 1200°C, evidence for lamellar domains within the α_2 phase were clearly seen (Figure 6-10(a)). However, when the sintering temperature was increased to 1300°C, an apparent hexagonal structure developed inside the grains (Figure 6-10(b)), confirming the hexagonal DO_{19} structure of the α_2-Ti_3Al phase [126]; this also indicated that the sintering process entered the final stage while the grains transformed to their equilibrium shape (i.e. minimising interfacial free energy) [127].

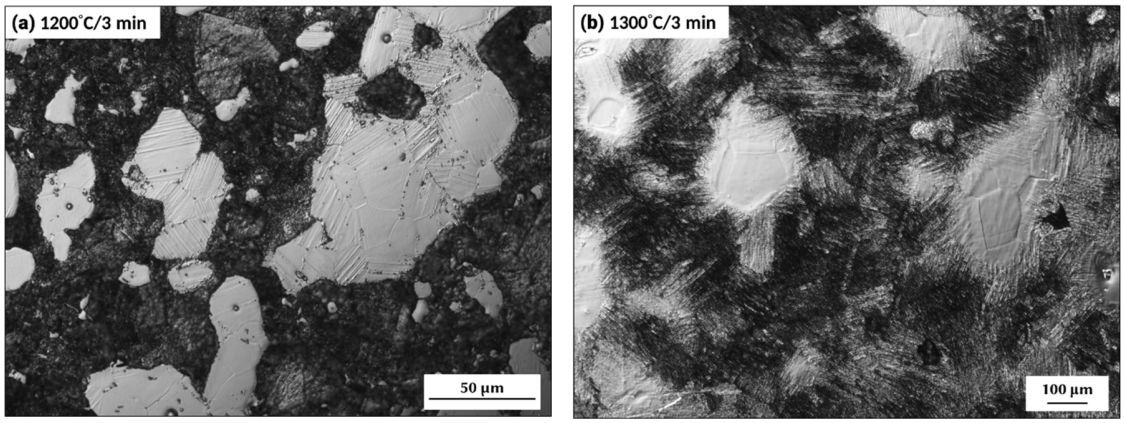

Figure 6-10. Representative DIC optical microscopy images of: (a) the internal microstructure in the α_2-Ti_3Al grains (SPS processed at 1200°C/3 minutes), and (b) hexagonal core structure formation when the sintering temperature was increased to 1300°C (held for 3 minutes).

These transformations occurred not only within the α_2 grains but also in the lamellar structure. In contrast to the small lamellar domains presented in Figure 6-7 (i.e. area C), an apparent coarse lamellar structure had developed along the Ti diffusion direction, away from the cores. Figure 6-11 illustrates the early progress (i.e. 1200°C) of this transformation; the lamellar expansion can be clearly seen. When the sintering temperature was increased to 1300°C, diffusion is expected to be much faster, and consequently the coarse lamellar structure was more significantly evolved. Furthermore, under these

processing conditions the material was relatively dense, such that the aforementioned lamellar expansion area and the 'roughened' two-phase area, discussed earlier, underwent a rapid transformation due to the general absence of hindering obstacles (i.e. pores).

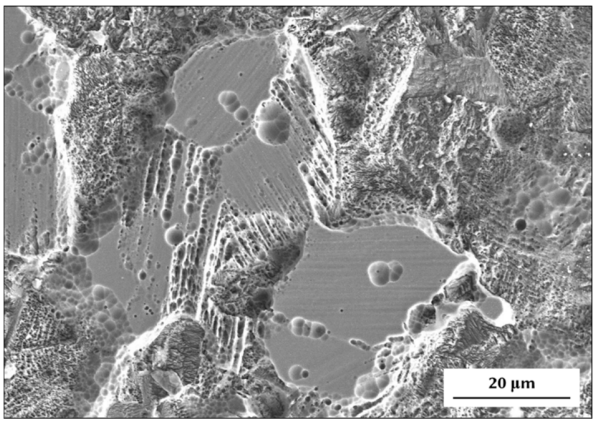

Figure 6-11. Typical SEM image showing initiation of the lamellar structure formation after SPS processing at 1200°C/5 min (combined SE/BSE image).

The progression of such massive lamellar formation, when transitioning from 1200 to 1300°C, is highlighted in Figure 6-12. As presented in Figure 6-12(b), after cooling the 'roughened' regions are transformed to an obviously lamellar structure, and both the grains and lamellar structures are coarsened. Larger γ-TiAl phase regions also develop at this stage. The samples sintered at 1300°C also presented a more homogeneous chemical composition between the grain and lamellar structure, and both responded to the etchant with a relatively similar resistance. The grains were consequently not as noticeable as they were before the rapid transformation (i.e. when using a sintering temperature below 1300°C). In addition, the phase evolution in the 'rough' two-phase area was more difficult to examine, because there were several morphological features presented within these regions, as highlighted in Figure 6-13. The various morphologies were due to both differences in crystalline orientations and the α_2:γ ratio within the grains, each of which leads to particular responses to the etchant. The resultant microstructure resembles a more apparent 'duplex' structure, which is comprised of the rounded γ grains and the α_2/γ lamellar structure (Figure 6-13(b)).

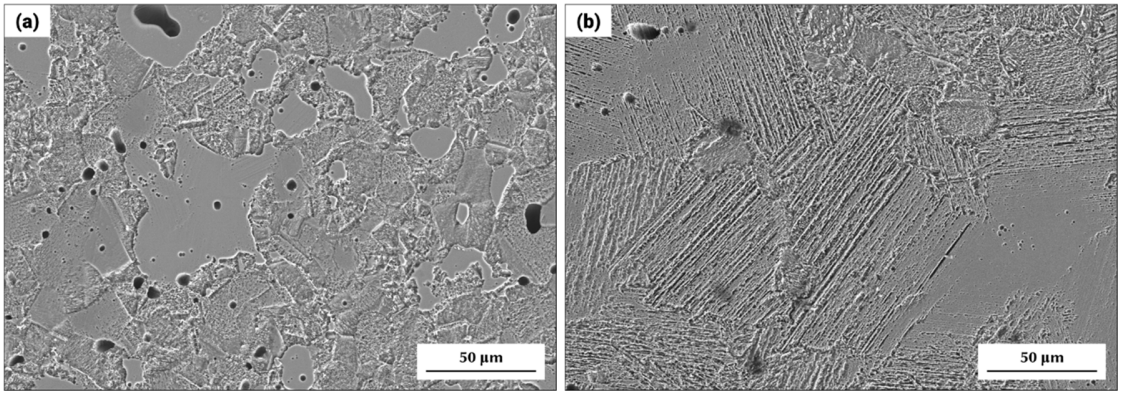

Figure 6-12. Representative SEM microstructural changes observed when transitioning from SPS processing temperatures of: (a) 1200°C/3 minutes to (b) 1300°C/3 minutes. Both examples show combined SE/BSE images

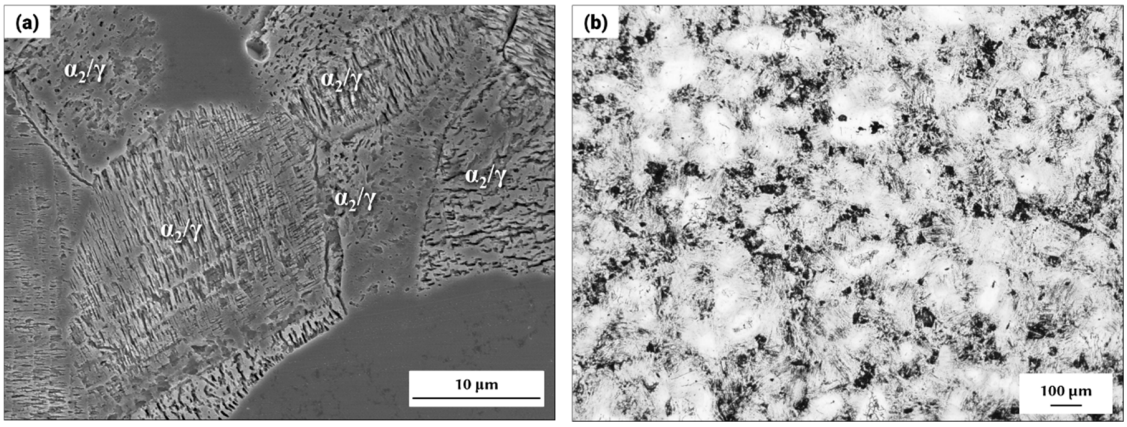

Figure 6-13. (a) Typical SEM image highlighting identification of the various morphological features in the two-phase area after sintering at 1200°C/10 minutes (combined SE/BSE image). (b) Optical micrograph of an etched sample (SPS processed 1300°C/3 minutes), showing a 'duplex'-type structure.

The effects of sintering temperature, time and initial particle size have been discussed in this section. Figure 6-14 summarises the lamellar transformation using a single α_2-Ti_3Al grain model. Such a simple configuration is adopted from the initial powder structure that contains a Ti-concentrated core. At the lower processing temperatures (i.e. <1300°C), grain growth was contributed directly from the α_2 phase nucleation or, in most cases, from the α_2/γ lamellar structure formation when Ti diffuses out of the core. This

newly grown area consisted of very fine lamellar structures, and could potentially be easily overlooked without suitably controlled etching. Many α_2 grains were comprised of multiple subgrains, and a fine lamellar structure was also growing within some of the subgrains (Figure 6-10(a)). At lower sintering temperatures, the lamellar structure was restricted to the fine laths, even with a longer sintering time, owing to the relatively slow diffusion kinetics. However, when the sintering temperature was increased to 1300°C, a coarse lamellar structure developed out of the grains, and the laths were wider and more pronounced, due to the increased thermal energy.

The phase transformation behaviour of the composite α_2/γ regions was more complicated. The two-phase area exhibited several morphological features within the grains, as individual grains comprised of various α_2:γ ratios, as well as different crystalline orientations. It is proposed that the Ti atoms segregate to the α_2-Ti_3Al phase in order to form alternating α_2 and γ phases. Some grains which contain lower Ti initially would transform to a generally rounded γ phase morphology, if no α_2 phase nucleates (Figure 6-15). Additionally, the microstructure evolution of Ti-48Al also involves the interaction of residual pores with each phase. The role of these remaining pores will be discussed in the following section.

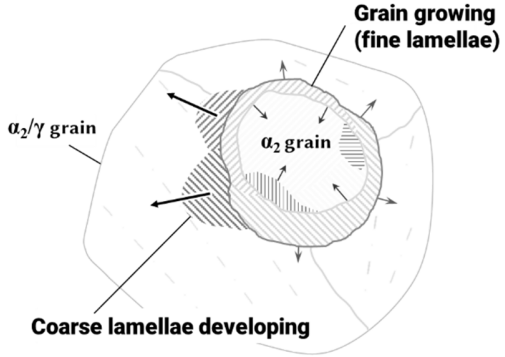

Figure 6-14. Proposed microstructural transformation mechanism within an α_2-Ti_3Al grain after cooling to room temperature.

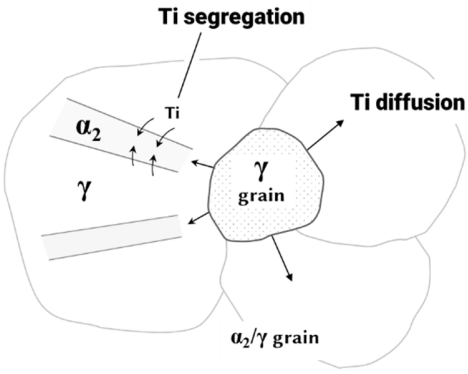

Figure 6-15. Schematic representation of Ti diffusion and segregation in the two-phase (α_2/γ) regions.

6.3.3.3 Pore evolution and agglomeration

Pore configurations in a material can be used as an indicator in terms of the sintering stages. As densification progresses, pores shrink and their concentration invariably decreases simultaneously. However, when the densification rates gradually decrease in the final sintering stage, the pores coalesce to reduce the system (surface) energy in the material. The pores therefore undergo an Ostwald ripening stage, which describes how the larger pores grow in size at the expense of the smaller ones. In the present study, the pore size (Feret length) and associated area fraction (used as the 'pore quantity') were measured from the un-etched optical micrographs, and then plotted to illustrate the pore evolution for the sintering temperature (Figure 6-16(a)) and time (Figure 6-16(b)), as well as the initial powder particle size (Figure 6-17).

From the pore configurations evolving with temperature or time, shown in Figure 6-16, both variables revealed the general trends of the Ostwald ripening stage. This phenomenon was especially obvious when examining the time effects (Figure 6-16(b)). Initially the pore size and the area percentage both decreased with time, indicating densification in the material. However, when the sintering time exceeded 5 minutes, the pores grew noticeably, while the area percentage continued to decrease, suggesting the process had reached the final sintering stage. Further sintering would not significantly improve densification but may cause adverse pore swelling (i.e. over-sintering).

Conversely, in terms of "non-thermal" parameters, specifically the starting particle size (Figure 6-17), for a lower powder size the pore length decreased accordingly due to smaller voids between particles in the green compacts. The pore area fraction did not show a definite trend, in spite of the density increasing (shown in Figure 6-16). It should be noted that as the porosity area fraction decreases to less than a half percent, and imaging artifacts may affect the software in determining the actual porosity content.

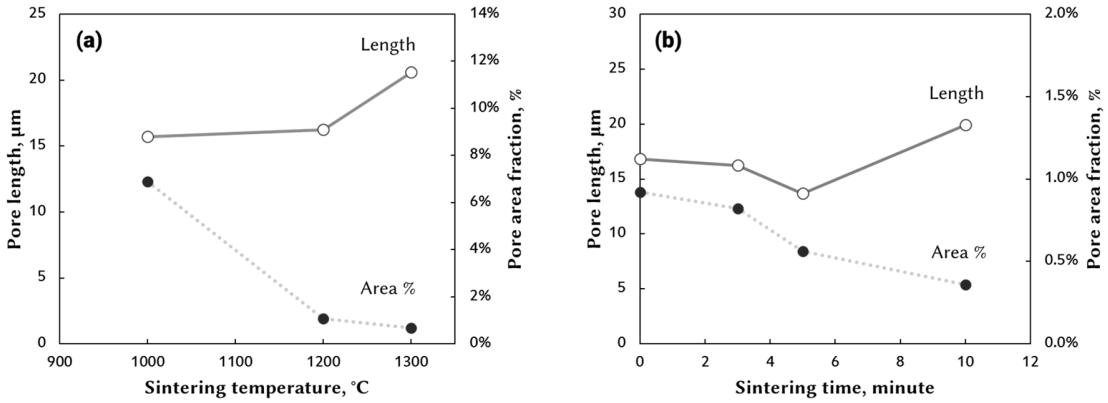

Figure 6-16. The pore length and area fraction of SPS processed samples, showing the effects of: (a) sintering temperature (held for 3 minutes), and (b) holding time (at a temperature of 1200°C). Both experiments used a starting powder with $D_{50} = 56.7$ µm.

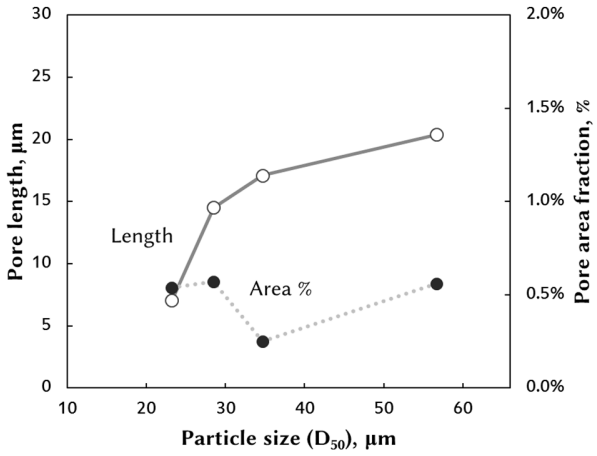

Figure 6-17. Starting particle size effects on the final SPS processing pore configuration (samples sintered at 1200°C for 3 minutes).

Furthermore, the pore locations and their associated migration were also noted under various sintering conditions. For example, in the sample sintered at 1200°C for 5 minutes, larger pores were generally situated within the α_2-Ti_3Al grains (shown in lighter contrast in Figure 6-18(a)), whereas the small pores were primarily dispersed in the two-phase region (shown in darker contrast in Figure 6-18(a)). With a longer sintering times, the smaller pores gradually disappeared through densification, but they also coalesced to form larger pores. This observation not only confirmed the previously mentioned Ostwald ripening phenomenon, but also highlighted how the two-phase region might 'grow' (i.e. diffuse) more to eliminate the pores, while the α_2 grains grew more slowly or later in the process. As a consequence, comparatively larger pores remained in the α_2 grains. This is further supported by the previous discussions, as it is apparent that the grain (α_2) phase was developed later, after processing at a higher sintering temperature (or longer time), as evidenced by the XRD. Furthermore, the grains gradually grew around or potentially even encompassed the pores, as demonstrated in Figure 6-18(b). Once the pores were included within the grains, they began to aggregate. Figure 6-18(c) illustrates that the smaller pores diffused along the grain boundaries and eventually merged with the larger one in the polycrystalline particle core. Such behaviour might also occur in the lamellar phases, as there was also pore growth, although it was difficult to observe the phenomenon from the micrographs.

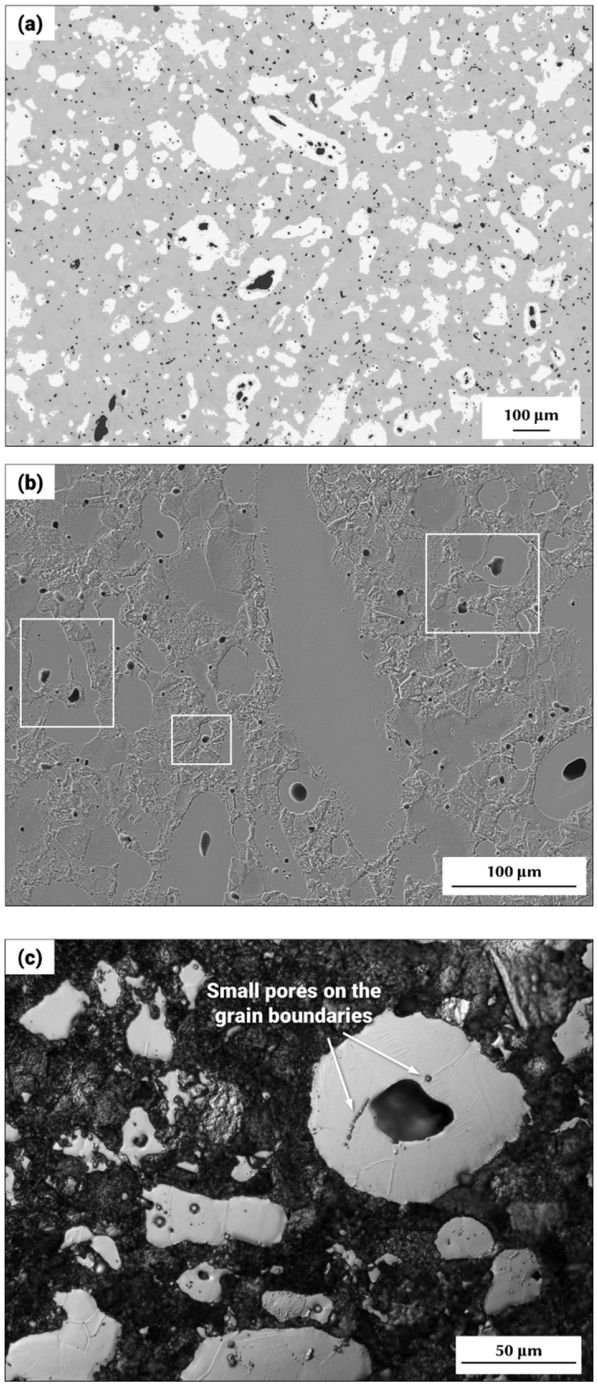

Figure 6-18. (a) Contrast enhanced optical micrograph of pore locations within the sintered microstructure (1200°C/5 minutes). (b) SEM micrograph showing pore entrapment after sintering at 1200°C/3 minutes (combined SE/BSE image). (c) Optical micrograph of pore agglomeration (1200°C/5 minutes).

6.4 Conclusions

In the present study, the SPS process had shown significantly greater sintering efficiency, in terms of densification, than conventional vacuum sintering. Near fully dense (~98%) Ti-48Al samples were achieved when sintering at 1200°C with a hold time of merely three minutes. It was found that sintering longer than three minutes did not improve the densification significantly, but reduced the hardness due to grain growth. The use of a smaller starting particle size contributed to a generally finer microstructure (i.e. residual pores and grains) and slightly improved the sintered density.

During sintering, the Ti-concentrated α_2 grains could grow directly following α_2 phase nucleation, or more likely from the fine lamellar structures, which developed at lower sintering temperatures (<1200°C). However, with increased diffusion kinetics at higher temperatures (>1200°C), a clear hexagonal structure developed within the grains, while the 'roughened' (i.e. α_2/γ lamellar composite structure, after etching) phase underwent a massive transformation. Coarse and long lamellar structures initiated from the edges of the grains and developed throughout the whole material.

As the densification progressed, the pores generally evolved following the Ostwald ripening mechanism, exhibiting a decrease in pore quantity but an increase in mean size. The relationships between the pores and aluminide phases suggested the 'roughened' composite areas grew faster, or earlier, as the pores were smaller and present in larger numbers in those regions. In comparison, it was shown that the α_2-Ti_3Al grains developed more slowly, or later in the process, because the pores were larger in size and difficult to collapse, resulting the fact that the grains gradually grew around the pores.

Acknowledgements

The authors would like to thank technical support from Randy Cook and Greg Sweet. The financial support for this research comes from the Automotive Partnerships Canada (APC) program (Grant No. APCPJ 411917-10), funded by the Natural Science and Engineering Research Council of Canada (NSERC). We would also like to thank Wescast Industries Inc. and Kingston Process Metallurgy Inc. for their financial, in-kind and technical support. The support of the Canada Foundation for Innovation, the Atlantic Innovation Fund, and other partners who helped fund the Facilities for Materials Characterisation, managed by the Dalhousie University Institute for Materials Research, is also gratefully acknowledged.

Chapter 7. Preliminary Results of B_4C-reinforced TiAl Composite Consolidated by Spark Plasma Sintering Process

7.1 Introduction

In the Introduction, the advantages of Ti alloys were discussed, such as their excellent corrosion resistance and specific weight-to-strength ratio. However, Ti alloys generally suffer from inferior wear and creep resistance. To improve these inadequate properties, Ti alloys can be reinforced with high strength and high stiffness ceramic phases to form a titanium matrix composite (TMC). Conventional TMCs incorporate a variety of reinforcements, such as continuous fibres, discontinuous whiskers and/or particulates. Continuous SiC fibres have been applied to improve the creep resistance in Ti alloys, for example for use as shafts, hollow fan blades, or compressors in aerospace engines [128]. The automobile industry has also adopted TMCs for the intake and exhaust valves in engines [129]. However, fibres or whiskers can cause highly anisotropic mechanical or electrical properties [130]. Furthermore, the large difference in coefficients of thermal expansion (CTE) between the fibre and the matrix can cause residual thermal stresses in the components [128]. Moreover, expensive SiC fibres and costly manufacturing process have limited the commercial use of TMCs.

As a potential alternative, powder metallurgy is a cost-effective approach to produce composites with isotropic properties using particulate reinforcement phases. Of the many potential reinforcements, it is well documented that TiC and TiB_x (x=1, 2) are among the most ideal ceramics, due to not only their high strength but also the matching modulus and density to titanium. For the Ti-B_4C system, two potential reactions can occur:

$$\mathbf{Ti + 1/3B_4C = 2/3TiB_2 + 1/3TiC} \qquad \textbf{Eq.7-1}$$

$$\mathbf{Ti + 1/5B_4C = 4/5TiB + 1/5TiC} \qquad \textbf{Eq.7-2}$$

The likelihood of these occurring depends on the reaction conditions. Reaction Eq. 7-2 is more likely to occur as the Gibbs free energy is lower than reaction Eq. 7-1. However, TiB and TiB_2 may both be present due to the limited mass transport in solid-state sintering [131]. The incorporation of TiB_x particles can significantly improve high-cycle fatigue resistance of the Ti alloys [128].

On the other hand, boron carbide (B_4C) is a light (2.52 g/cm^3) material with remarkable hardness and wear resistance, combined with a high melting temperature. This ceramic is considered to be the most effective way to form both TiC and TiB_x *in situ* in the matrix [132,133]. Reactive sintering of the composite *in situ* generally produces finer grain sizes and cleaner interfaces between the reinforcement and the matrix, resulting in better strength and creep resistance compared to *ex situ* formed TMCs (i.e. when particles are added in directly) [134].

One of the main applications of the TiAl alloys is for high temperature components, where creep and wear properties are particularly important. Therefore, incorporation of reinforcements to the material may be beneficial. Zhang and co-workers have focused on the B_4C material and applied TiAl (10-40 wt-%) to reinforce it using hot pressing. In their work, the elemental Ti, Al and B_4C powders were ball milled before sintering. The authors observed that Ti was prone to react with B in the B_4C to form TiB_2 during ball milling; the TiB_2 disappeared when the TiC was generated after hot pressing. The TiAl reinforced B_4C possessed the anticipated mechanical properties of the composite [135]. Nevertheless, comprehensive research investigating TiAl-based intermetallic composites is still lacking.

Following from the earlier work presented in Chapter 6, the SPS technique has been successfully utilised for many difficult-to-sinter ceramics. The SPS process has also demonstrated its efficiency for sintering TiAl powder, and therefore provides a potential alternative manufacturing method to produce TiAl-based composites.

7.2 Materials and Methodology

For the present work, a fine B_4C powder (D_{50}=11.4µm), as shown in Figure 7-1, was blended (up to 6 wt-%), and then sintered with the 'in-house' produced TiAl powder (D_{50}=56.7µm) (see Figure 6-1). For initial studies, the SPS temperature was 1200°C, held

for a period of 3 minutes. Detailed sintering procedures and analysis methods can be found in Chapter 6.

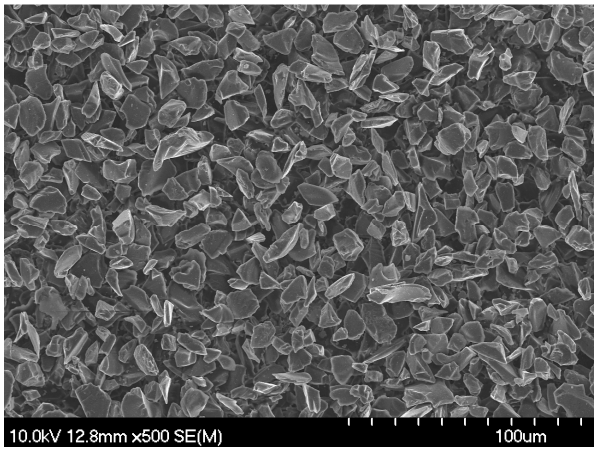

Figure 7-1. SEM morphology of the reinforcing B_4C ceramic particulate

7.3 Results and Discussion

In this research, for the sake of simplicity, the B_4C was assumed to sinter with the TiAl power with no reaction volume change, and therefore the density calculation of the composite was based on a simple rule of mixture. Figure 7-2 shows that more B_4C reinforcements seemingly improve the sintered density and hardness in a linear manner. The phase evolution (XRD) in Figure 7-3 clearly indicates that TiB, TiB_2, TiC and Ti_2AlC are formed with increasing B_4C addition; some B_4C was not completely reacted with the matrix, likely at 4 and 6 wt-%, and the remaining B_4C grains can be seen in the SEM micrograph in Figure 7-4. However, more thorough analysis is needed to identify the phases in the composite, as many characteristic XRD peaks are closely overlapping, such as peaks of B_4C with those of TiB_2, and peaks for TiB with TiC.

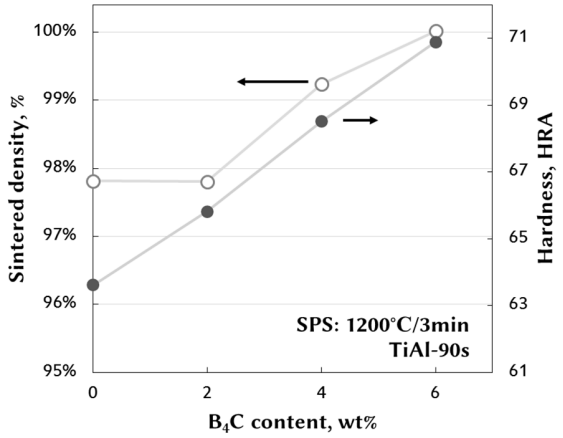

Figure 7-2. Effects of B_4C reinforcement addition to densification and hardness.

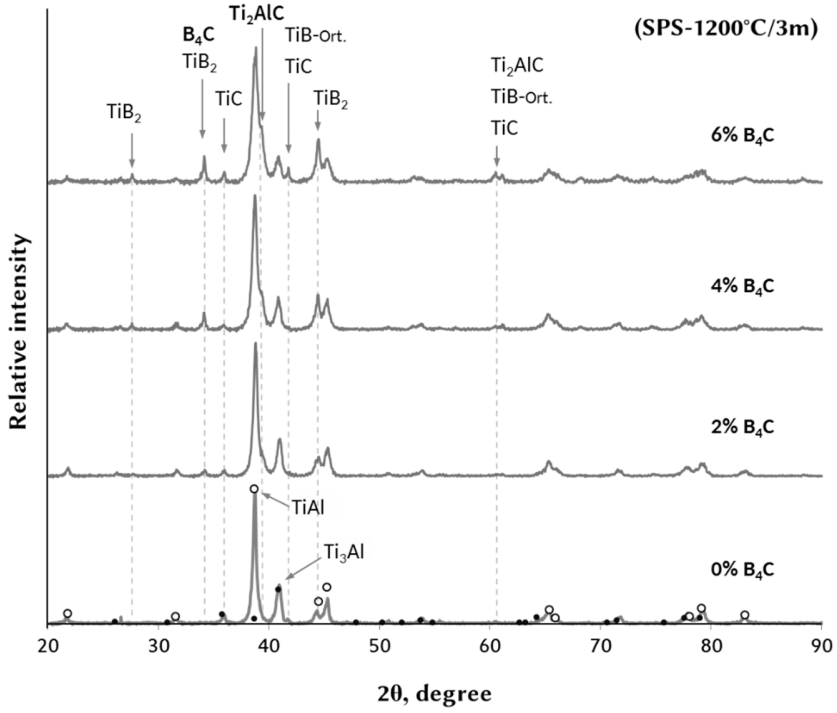

Figure 7-3. Phase evaluation when adding more B_4C reinforcement. Material was sintered at 1200°C for 3 minutes.

The sintered sample (TiAl-6wt.% B_4C) was polished and etched to reveal the resultant microstructure (Figure 7-4). Some B_4C particles (dark contrast) still remained

after sintering, and from a closer inspection (Figure 7-4(b)), several layers and agglomerated (TiB_2) whiskers are visible. EDS analysis was conducted to show the compositional distribution across the B_4C grain in Figure 7-4(b), and the result is presented in Figure 7-5. Zone 1 is essentially the B_4C grain core. However, the atomic ratio (B:C=60:40) does not match the stoichiometry of B_4C. This is perhaps due to the inaccuracy of EDS when detecting light elements (atomic number B=5, C=6) [136]. Nevertheless, carbon appeared to diffuse faster than boron though Zone 1 to 4. On the other hand, Ti diffused faster than Al to Zone 2, while Al was seemingly hindered from entering Zone 2, and thus accumulated in Zone 3.

In Figure 7-4(b), the whiskers and rods were tentatively identified as TiB_2, which tended to agglomerate and locate between the B_4C grains. Moreover, pores are also concentrated in the same regions. Therefore, it is likely that those areas were the locations where some B_4C grains completely transformed into TiB_2. In a recent Ti-B_4C SPS study, the TiB_2 whiskers were observed to form around the B_4C particles, and when the B_4C size was small (D_{50}=0.5μm), the B_4C reacted and disappeared completely. Furthermore, in the same study, it was found that sintering with small B_4C powder increased the tensile properties considerably (although elongation to failure suffered) [134].

TiB_2 not only can theoretically strengthen the matrix, but it has also been reported to have a strong pinning effect on the grain boundaries, thus enhancing mechanical properties (also mentioned in 2.2.2) [137]. Voisin and colleagues have observed that the size of the lamellar colonies in the TiAl (for a 4822 alloy) was strictly limited due to boron addition, even at a low concentration of 0.08 at.% (no obvious boride formed) [138]. Nevertheless, Gorsse and Miracle have reported that TiB_x whisker aggregation is undesirable, because cracks could initiate from the cluster regions at low strain [139]. In the same study, the authors also pointed out that heat treatment can eliminate the TiB_x whisker clusters. However, annealing at higher temperatures or for a longer duration (1200°C/100h or 1300°C/6h) unavoidably led to grain growth [139]. Alternatively, Ni and colleagues have applied an extrusion process in order to break down the clusters [131]. Nevertheless, more experiments are still needed to understand the complicated reactions between the B_4C powder and the γ and α_2 phases in the TiAl alloy.

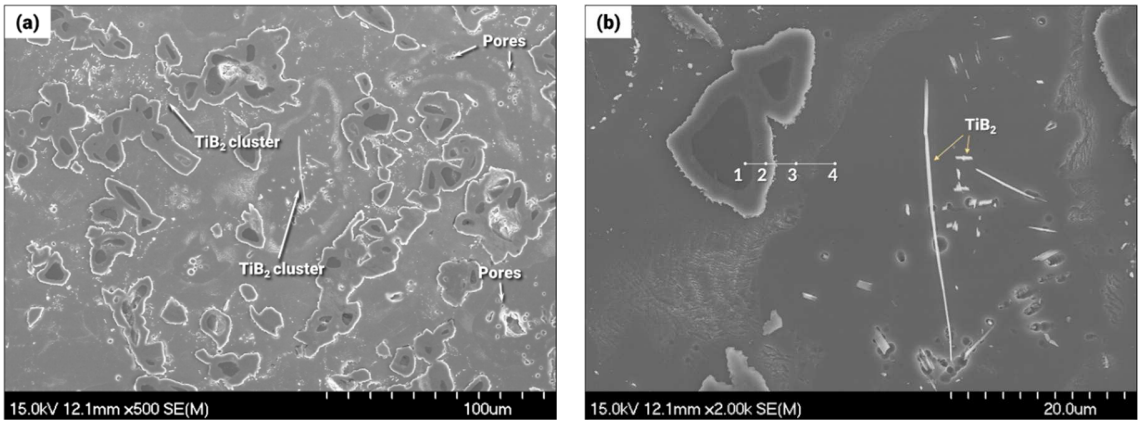

Figure 7-4. Representative SEM micrographs showing: (a) microstructure of TiAl-6wt.% B_4C consolidated using spark plasma sintering. (b) Closer inspection of (a), showing the compositional layers and TiB_2 whiskers.

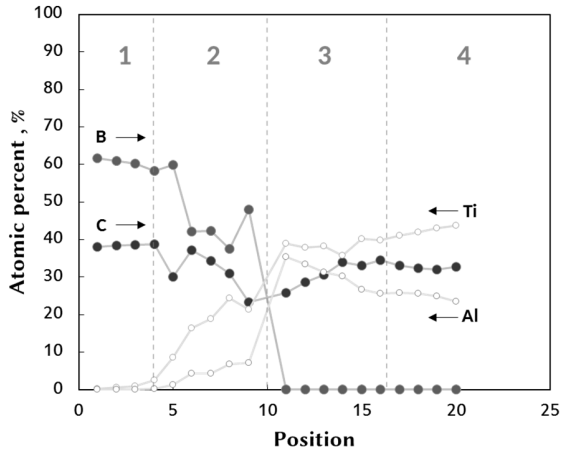

Figure 7-5. Cross-sectional chemical profile of the B_4C particle in Figure 7-4(b).

7.4 Summary

In this chapter, the effects of B_4C reinforcement of TiAl have been investigated using the SPS process. Preliminary experiments have shown promising results in terms of densification and hardness improvements with increasing B_4C addition. From the microstructural analysis, the remaining B_4C particulates were dispersed in the matrix and a diffusion layer was observed. Compositional distribution across the B_4C particles indicated the diffusion directions for the individual elements (i.e. B, C, Ti and Al) and suggested their relative diffusion rates. The TiB_2 precipitates exhibited a whisker morphology, and they were clustered between the B_4C particulates. The formation of pores was also found to accompany the TiB_2 clusters, suggesting the initial locations of the fully reacted B_4C particles. Nevertheless, more experiments are needed to understand the reaction between the reinforcement and the matrix, and furthermore the interaction between B_4C and the lamellae (α_2/γ) or the γ-grains in the aluminide matrix. Other possible phase constituents (i.e. TiB, TiC, Ti_2AlC), which were detected by the XRD in the sintered material with the increasing B_4C content, require more analysis to be fully identified.

Chapter 8. Conclusion

In this thesis, two titanium alloys (i.e. Ti-Ni and Ti-Sn) and a Ti-48Al-based intermetallic alloy were produced using cost-effective powder metallurgical (PM) approaches, namely traditional pressureless sintering and the fairly novel approach of spark plasma sintering (SPS), respectively. The fundamental processing parameters have been investigated for both techniques, and the resultant microstructures and properties of the products have been studied and explained in the present work.

In the first part of the thesis (Chapter 3), Ni and Sn (up to 10 wt-%) were added to Ti to improve the sinterability, because of their respective anticipated liquid forming ability (liquid phase sintering, LPS) during the sintering process. For the Ti-Ni alloys, a persistent liquid occurred when the temperature reached the solidus line of the two-phase region (β + L). Possible transient liquids may develop when the Ni and Ti experienced eutectic reactions at lower temperatures (i.e. Ni_3Ti (1304°C), TiNi (1118°C), and Ti_2Ni (942°C)). On the other hand, the Sn addition only generated transient liquid, which may partially improve the green compact packing when Sn melts at 232°C.

Improved sintered density (compared to non-alloyed Ti) was clearly seen for the Ti-Ni alloys of all compositions (2.5 to 10 wt-% Ni), indicating the benefits of LPS. The improvement was the most obvious when sintering at 1300°C with 7.5%Ni addition, and almost 99% of theoretical density was achieved. Alternatively, the Ti-Sn alloys displayed minor improvements at lower temperatures, but lowered densities were observed above 1250°C. Such results suggested the transient liquid forming from the Sn additions was not effective, although the soft Sn powder contributed to a better compaction in the green state and a consequent gain in densification.

The results of mechanical properties are more complicated, particularly for the Ti-Ni alloys, as the shape and amount of the α phase changed with the sintering temperature and the Ni content. Moreover, while the increasing amount of hard Ti_2Ni precipitates increased the hardness, it came at the expense of elongation. Additionally, residual porosity in the samples significantly affected the mechanical properties (particularly tensile

elongation), as seen from the morphological change in the fractural surfaces of both Ti-Ni and Ti-Sn alloys. The porosity analysis (size distribution) indicated that Ostwald ripening of the pores occurred more obviously for the Ti-Ni alloys (>1300°C or 7.5 wt-% Ni), suggesting the sintering process had entered the final 'over-sintering' stage. No clear indication of Ostwald ripening appeared for the Ti-Sn alloys, and they also behaved more closely to the CP-Ti in terms of the mechanical testing results.

In this work, despite the use of a thermodynamic simulation software (FactSage^{TM}), a method to monitor the liquid formation in real-time, such as using a differential scanning calorimetry (DSC), is recommended and important for further understanding of the LPS process. The tensile properties in the current study, particularly for the Ti-Ni samples, showed significant scatter, such that no firm conclusions could be made. Consequently, further tensile testing or other mechanical tests should be carried out to acquire a more statistical sense of the effects of alloying.

In the second part of the thesis (Chapter 4 to Chapter 7), the processing of titanium aluminide has been investigated. To begin with, the Ti-Al alloy was produced using the elemental Ti and Al powders, and pressureless sintered in a simple tube furnace (Chapter 4). In spite of the relatively high green density (~94% of theoretical, when pressed at 400MPa), the elemental compacts quickly encountered the inevitable swelling during sintering (sintered density decreased down to ~55%). The formation of such porous structure can be explained through assessing the structural evolution as the Al powder melted. Initially, a porous skeleton structure of $TiAl_3$ is formed in the early sintering stage, and this structure remains after sintering (as outlined in Böhm and Kieback's model, see Appendix Figure I-6). Reducing the Al particle size was expected to minimise a sudden amount of melt forming and thus volume expansion caused by $TiAl_3$. However, sintering finer powder (coarse 43 µm vs. fine 6.4 µm Al) only slightly improved the sintered density (by ~3%). Other processing variables, such as two-step sintering, low temperature annealing (4h) did not overcome the swelling issue sufficiently enough to warrant further study.

As an alternative, a pre-alloyed TiAl powder was anticipated to avoid the Al melting and consequent $TiAl_3$ formation stages during heating. In Chapter 5, a cost-

effective pre-alloyed TiAl powder was consequently produced 'in-house'. The procedures for powder manufacture that were established were also applied to the subsequent experiments on TiAl PM. The synthesised powder consisted of compositional layers in the order (from the outer layer to the core) of TiAl, Ti_3Al and possibly limited residual Ti. Based on prior literature, and results from the present XRD and EDS analysis, a formation model for the synthesised powder was proposed to explain the phase evolution, particularly the formation and disappearing of the intermediate phases ($TiAl_3$ and $TiAl_2$). The sequence of phases that were generated during sintering is: $TiAl_3$, TiAl, $TiAl_2$ and Ti_3Al. However, it should be kept in mind that the formation and disappearance of phases sometimes occurred concurrently.

As part of the powder production process, several powder grinding treatments (wet and dry methods) were also evaluated, particularly in terms of their ability to reduce the particle size. Dry shatterbox (with a 250 ml bowl) milling achieved the best efficiency, in comparison to the wet methods (i.e. ball and attrition processes). Addition of a process control agent (Licowax®) was shown to improve the milling effectively. However, concerns regarding the temperature (i.e. wax burning) and contamination from the agent need to be considered.

It was shown that the sintered density (~83%) was considerably improved compared to results from elemental blend sintering (~55%). A smaller starting powder size generally contributed to a higher sintered density. However, the improvement was limited at the sintering conditions of 1300°C for 2 hours. Instead, raising the sintering temperature or prolonging the heating time increased the sintered density to ~89% of theoretical. Despite the poor densification results (79%) from sintering using a larger powder size (47 µm), it allowed a detailed observation (due to slower diffusion) of the phase transformation(s) occurring. Lamellae nucleated from the Ti-concentrated areas (i.e. the residual Ti powder core) or the grain boundaries. When the lamellae growing from different directions encountered each other, they merged to form a larger lamellar structure, and each of the original lamellae was effectively a domain in this structure.

In Chapter 6, SPS technology was explored using the 'in-house' produced, pre-alloyed TiAl powder. Sintering temperatures up to 1300°C were examined, and near fully

dense samples (greater than 95% of theoretical density, at 1200°C) were achieved successfully in a fairly short period of sintering time (3 minutes of peak temperature hold). Longer sintering time (>5 minutes) contributed no noticeable improvement in densification, but deterioration in the hardness properties was observed, indicating grain coarsening. Meanwhile, longer sintering times (10 minutes) also caused carbon contamination (and the formation of TiC) from the die sets to the TiAl material. As a solid-state sintering process, a smaller powder size promoted better diffusion between particles. The sintered density was improved from 96% to 99% when the powder size was reduced in size from 56.7 to 28.5 μm (D_{50}). The hardness increased accordingly, with the better densification observed in the materials.

Building on the observations of phase transformation in the work relating to tube furnace sintering (Chapter 5), a simple microstructural transformation model was proposed in this thesis under rapid sintering conditions. Two types of lamellar structures were identified (fine and coarse). At lower sintering temperatures (i.e. <1300°C), fine lamellae grew within the α_2-Ti_3Al grains, which was difficult to observe without careful etching. Conversely, at 1300°C, a considerable amount of coarse lamellae developed out of the α_2-Ti_3Al grains and a more apparent 'duplex' structure was formed (i.e. rounded γ grains in combination with the α_2/γ lamellar structure). It should be pointed out that the phase with lower Ti content (γ) was very easily etched, while the areas with high Ti (α_2 or residual Ti) sometimes remained effectively undamaged from the etch treatment. The directions of the crystalline orientations in the lamellae grains also responded to the etching process differently, which may cause confusion when analysing the microstructures. At 1300°C, a more hexagonal structure formed in the cores, confirming the $D0_{19}$ structure of the α_2-Ti_3Al phase, and also that the sintering process had entered the final stage (i.e. grains minimising their interfacial free energy). With more complete sintering, the Ti in the γ grains or γ lamellae gradually segregated to the α_2 phase, until the compositions reached a more uniformly defined Ti:Al=60:40 ratio in the SPS samples.

Analysing the pore configuration changes under either temperature or time variation revealed the general trends of the Ostwald ripening stage. Again, this information suggested a preferred temperature range for SPS processing, before the sintered properties

are degraded. Alternatively, the 'non-thermal' powder size effects did not govern the pore coarsening phenomenon, instead the pore size decreased because of tighter powder packing and smaller voids between the smaller starting particles. With careful analysis of the spatial locations of pores and the phases, it was found that the larger pores were encompassed in the α_2 grains, whereas the smaller pores were dispersed in the two-phase region. Supported also by the XRD results, the α_2 grains grew more slowly or later in the process. Consequently, they encountered relatively large residual pores. Once the pores were included in the α_2 grains, they migrated through sub-grain boundaries and merged together.

Using the pressureless sintering and SPS PM approaches to produce the TiAl-based alloy, this thesis has provided insights to identify phase characteristics and explain their transformation mechanisms. However, despite the promising results with the SPS work, full densification in the samples is yet to be achieved. Any attempt to improve the mechanical, wear or corrosion properties of the TiAl-based alloys would not be effective if there is residual porosity in the material. Therefore, before the PM-based TiAl alloy can be utilised in commercial applications, the residual porosity needs to be eliminated. Future studies to achieve better densification are recommended as follows.

As the first step, the SPS processing parameters could be further optimised. Higher temperature (>1300°C) is recommended for further densification. However, a careful investigation on the die setup, to prevent the powder-tool bonding is necessary. Other process variables such as the compaction pressure, and heating/cooling rates should be further investigated to achieve better densification, and to acquire a 'balanced densification' treatment with minimal grain growth. Secondly, the impurities in the pre-alloyed powder should be minimised, as it was shown in the earlier chapters that the synthesised pre-alloyed TiAl powder contained relatively high oxygen and nitrogen contamination, which could affect the atomic diffusion process during a sintering practice. Elemental Ti and Al powder with lower impurities are preferred, to begin with, for the 'in-house' manufacturing. Moreover, better vacuum during SPS is necessary to avoid contamination from the atmosphere; some adjustments are also needed to reduce the contamination from the atmosphere (e.g. milling bowl sealing) and the grinding media in the milling process.

Post-processing heat treatment, such as annealing at the temperatures in the α_2 plus γ, α plus γ or even the α phase region, could be another approach for not only density improvement, but also microstructural modification. However, as mentioned in the literature review, the phase configuration (i.e. full lamellar, dual-phased or duplex structure) is strongly associated with the subsequent tensile behaviour. As a consequence, when applying the heat treatments, microstructural analysis and the resultant mechanical properties should both be emphasised.

Lastly, additional alloying elements could be incorporated with the TiAl powder to facilitate the diffusion processes (i.e. activated sintering). Elements that can increase the atomic motion or lower the activation energy for sintering are the ideal candidates. In addition, the liquid phase sintering mechanism, as discussed for the Ti-binary alloys in Chapter 3, is another means to enhance sintering densification. However, ternary reactions between the additions and the pre-alloyed TiAl powder are complicated, and thus it is difficult to predict the sintering outcomes accurately. In this regard, initial experiments could target some elements (such as Fe, Co or Cu), with lower melting temperatures, or low solubility for the Ti-Al alloy (activation sintering criteria). The amount and the functions (i.e. phase stabilising ability, property modification) of the additions should also be considered along with the microstructural modification.

As for the B_4C-reinforced TiAl alloy, Chapter 7 has shown the preliminary benefits of SPS processing on improving densification and hardness. However, , the reaction of B and C with Ti and Al are complicated, as both Ti and Al can react with B_4C and the research on this subject is still lacking. More fundamental experiments in terms of processing (e.g. sintering temperature and time) and material (e.g. ceramic type, particle size, and concentration) are needed to understand the reactions between the elements and the microstructural transformation. Moreover, in the early trials, the remained B_4C and the formed TiB_x were found to be less prone to etching, while the matrix (i.e. Ti-48Al) was removed completely. Hence, a proper etching procedure (different etchant choice or multiple etching steps) for the TiAl-B_4C composite are needed to reveal the phase (γ grain or $\alpha_2+\gamma$ lamellae) interaction between the reinforcement and the matrix. Eventually, wear and creep tests should be conducted to examine the effects of B_4C reinforcement.

Appendix I. Prealloyed powder production

Due to the limit availability of the commercial TiAl powder, the prealloyed powder was produced in the lab from the elemental Ti and Al powders. During the progress of the research, two Ti and Al powder blends were used for powder synthesis due to supply switch and are detailed in Table I-1. The finer Ti and Al were grouped together for the prealloyed Ti-48%Al sintering study in Chapter 5, and the coarser size combination was used for the spark plasm sintering in Chapter 6. In this section, extra information in terms of characterisation of the materials and processing is provided.

The individual particle size distributions are exhibited in Figure I-1. The morphology of each powder is considerably different due to their manufacturing process as seen in Figure I-2.

Table I-1. Raw elemental powders for the prealloyed powder production.

Powder	Source	Type
Ti-Reading	Reading Alloys	Mg-reduced, -100+325mesh
Al-MEP107	Ecka Granules	
Ti-ADMA	ADMA	Sponge, -100+325mesh
Al-DG20	Ecka Granules	

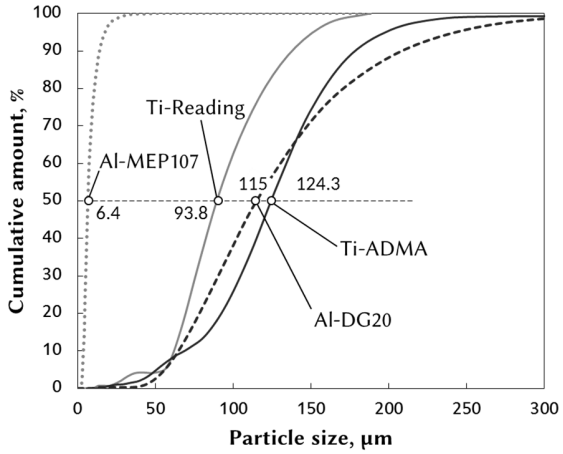

Figure I-1. Particle size distribution (with D_{50}) of the raw elemental powders.

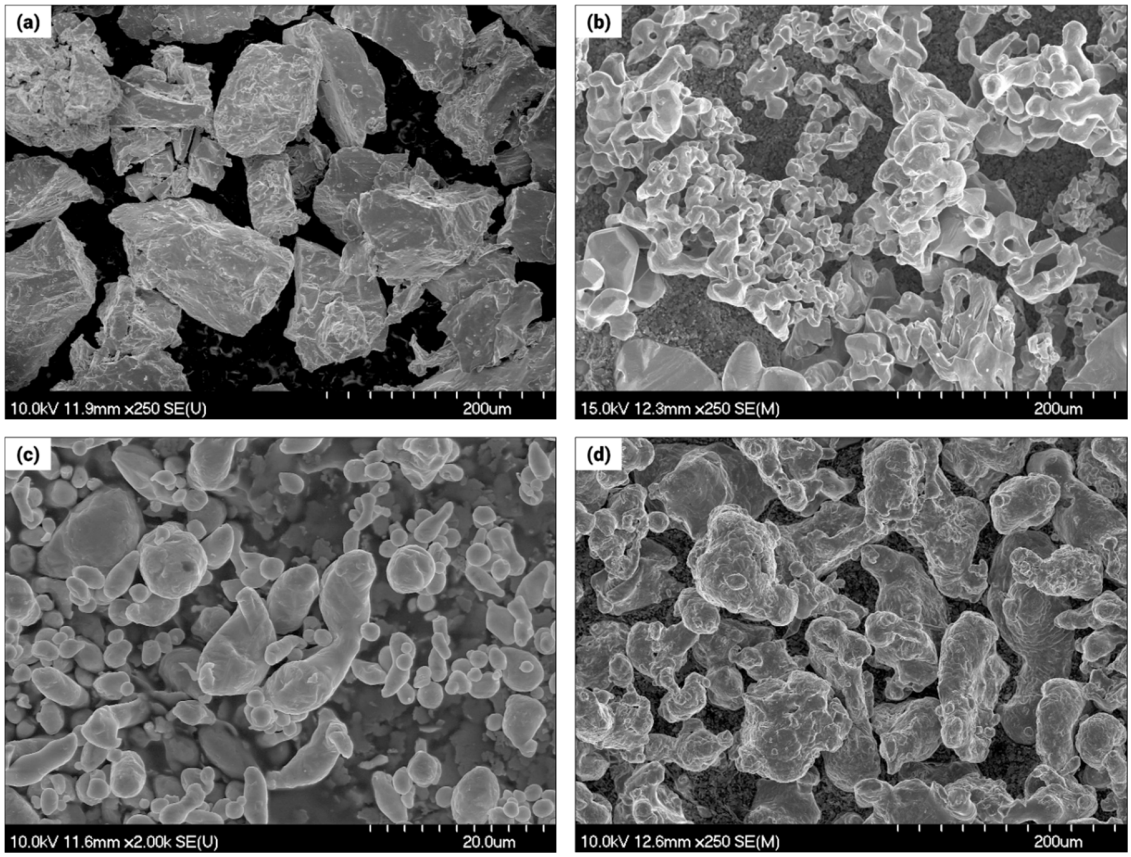

Figure I-2. SEM micrograph showing the morphology of the elemental powders (a) Ti-Reading, (b) Ti-ADMA, (c) Al-MEP107, (d) Al-DG20.

Each of the two elemental powder blends was mixed thoroughly in a mixer for 30 minutes. The powder blend was consequently pressed by either cold isostatic pressing or manual pressing (hydraulic press) into green compacts for sintering. Figure I-3 highlights the production procedures. Figure I-4 shows the micrographs of the green compact of both fine and coarse elemental blend.

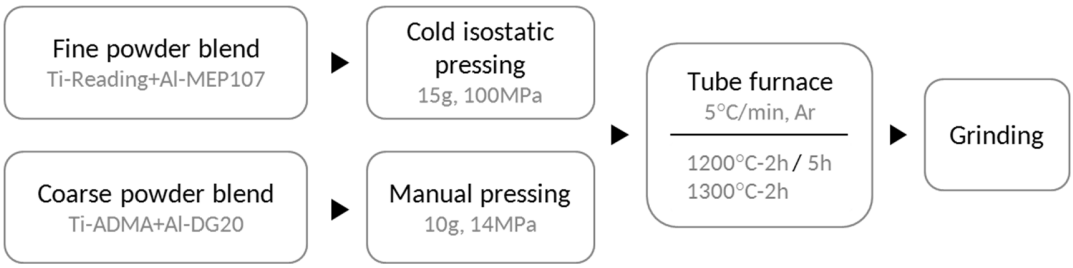

Figure I-3. Powder production process flowchart.

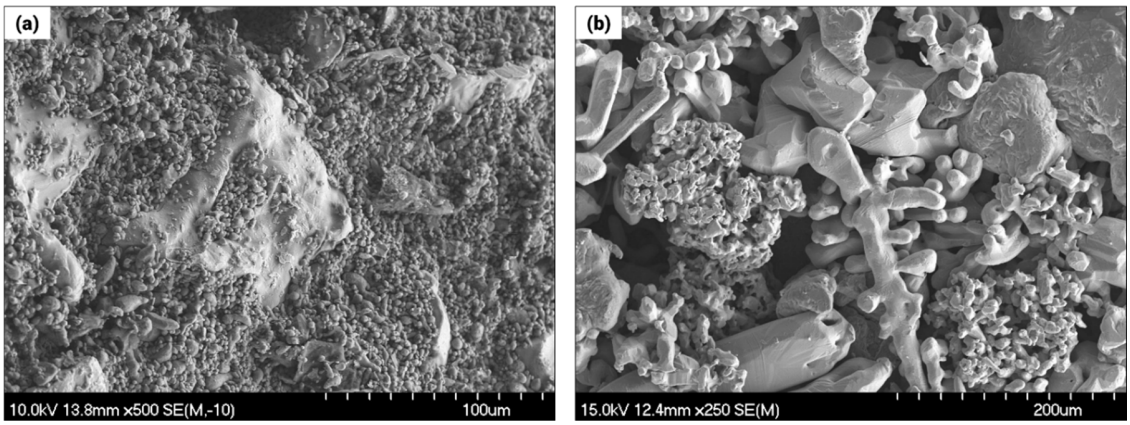

Figure I-4. Green compact of (a) fine and (b) coarse powder blend.

The prealloyed Ti-48Al powder was synthesised in a conventional tube furnace. The process was a simple one step heating stage to the peak sintering temperature (1200°C or 1300°C) for a duration of 2 or 5 hours (only for reference), and then cooled down to room temperature. The heating and cooling rate were controlled at 5°C/min, and the whole process was performed under argon atmosphere. Detailed process procedures can be found

in Chapter 5 and 6. Despite the difference in size and shape, the two blends displayed generally similar XRD results (slightly more Ti_3Al phase in the coarse blend) after sintered.

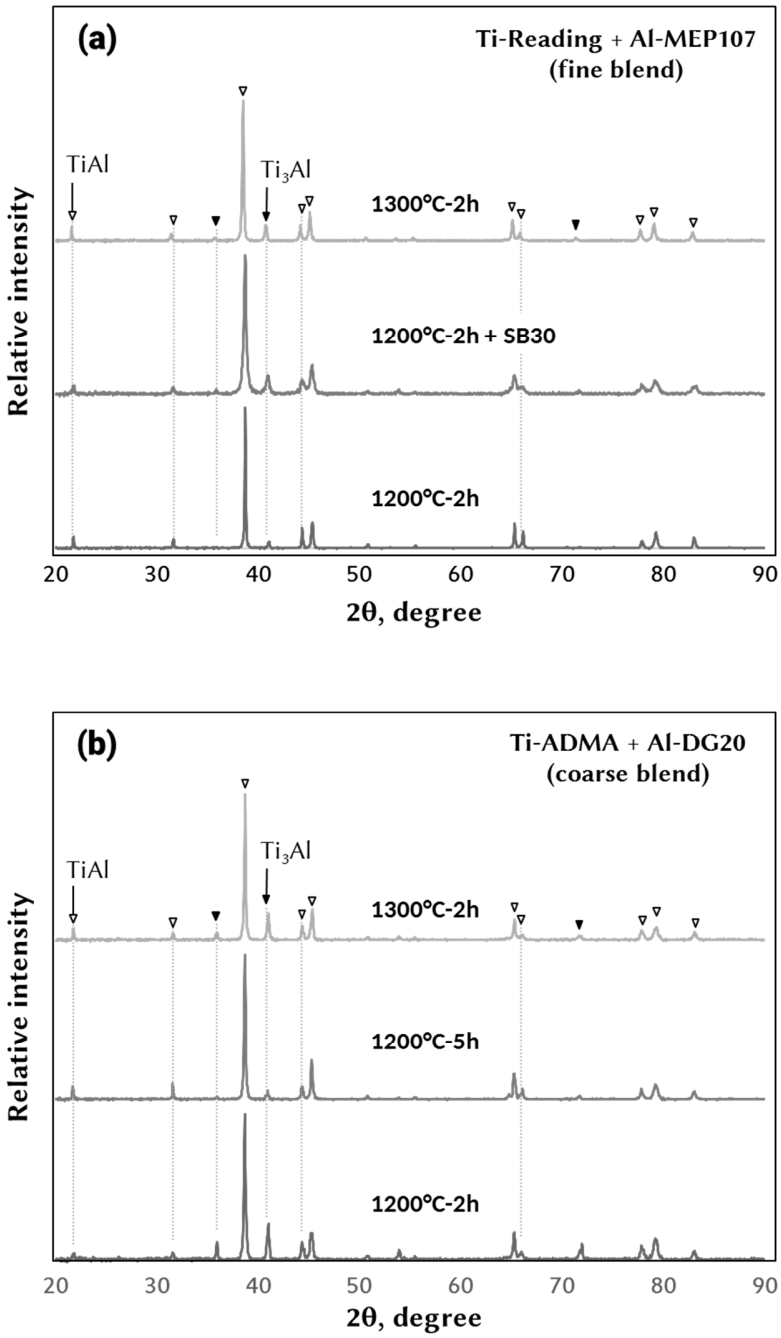

Figure I-5. Effects of sintering temperature and time on phase evolution to the (a) fine (b) coarse blend.

The formation mechanism of the layered structure inside the powder has been discussed in Chapter 5. For the early sintering stage, Figure I-6 presents Böhm and Kieback's model describing the reactions between the elemental Ti and Al and the forming of the lose skeleton Al_3Ti structure. In this model, a considerably amount of Al liquid is formed due to the large Al powder. The melt wets the powder compact, creating a little expansion (a_1>a). The large voids left by Al melting away will be a major source of larger pores in the material. Al_3Ti forms at this stage until all the Al melt has reacted (stage 4). In this stage, most of the Al_3Ti fused together and a loose structure forms. Further densification is difficult as considerable amount of mass transport is required to fill the voids.

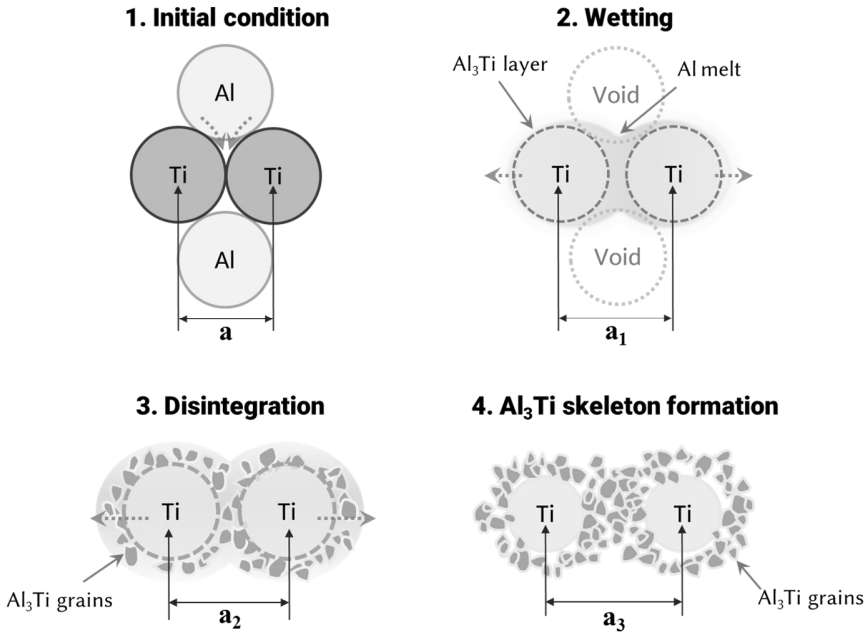

Figure I-6. Elemental Ti and Al powder sintering mechanism, where in each stage the volume expansion is expressed in terms of Ti particle distance ($a<a_1<a_2<a_3$). (redrawn from [85]).

Appendix II. Grinding methods efficiency and contamination

In Chapter 5, the efficiency of each grinding method has been evaluated based on their ability in reducing the medium (D_{50}) powder size. Here, more detailed results are expressed in particle size distribution (PSD) as a function of grinding time and solvent type (Figure II-1). For 30 minutes of milling, using isopropyl alcohol (IPA) solvent results considerably better milling results than the hexane (HX). As discussed in Chapter 5, a possible explanation is that due to the evaporation rate difference of the two solutions in this semi-open equipment setup. According to ASTM D3539-87, hexane evaporates faster than IPA (evaporation rate is 7.8 and 2.9, respectively (n-butyl acetate=1)) [140]. As a result, the use of IPA solution resulted in less loss and is more suitable for the attrition milling. Furthermore, it is clear that milling for 2 hours does not provide noticeable improvement in PSD reduction than for 1 hour.

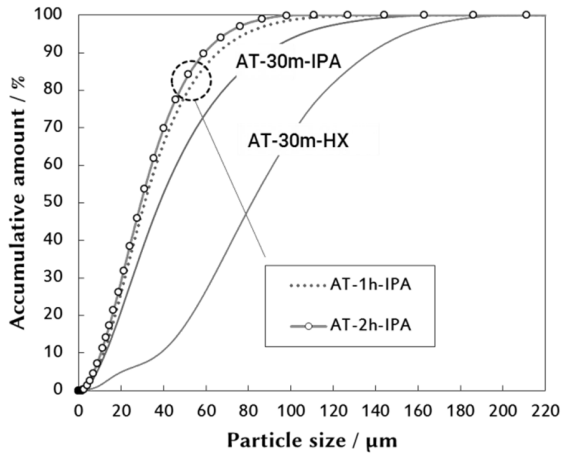

Figure II-1. Powder particle size distributions after attrition milled for 1 to 2 hours with IPA or hexane solution.

As for the shatterbox milling process, Figure II-2 clearly shows the progressive reduction of PSD of the large shatterbox milling (10~60 minutes). In addition, the SBL provided greater milling capability (30 minutes) than the small shatterbox, even at much

lesser milling time of 10 minute. The use of Licowax also improved the grinding efficiency significantly: finer PSD was achieved at less than 30 minutes compared to milling without the LC. Grinding time was still an important factor in reducing the PSD, and further grinding may produce even finer PSD (>10 µm). However, the optimal amount of LC was found to be at 1 wt.%. For comparison, Figure II-3 highlights the best PSD results of individual grinding methods.

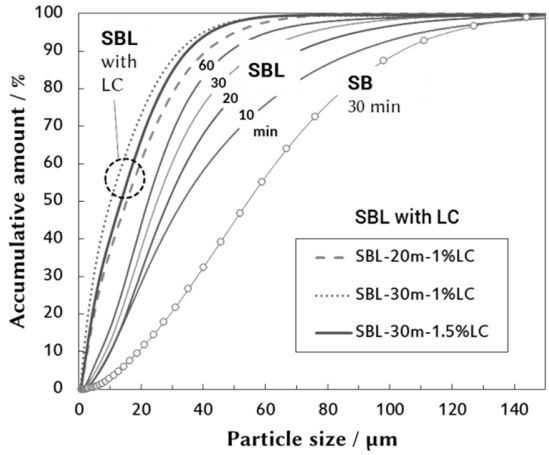

Figure II-2. Powder particle size distribution of shatterbox (large) milled powders for various grinding time up to one hour and the effects of the Licowax® addition.

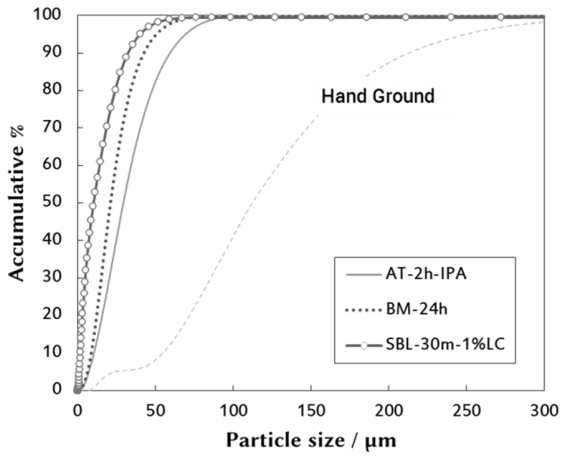

Figure II-3. Comparison in grinding efficiency between the shatterbox (large), attrition, and ball milling.

In Chapter 5, the contaminations associated with the process were also investigated and reported in normalised results. Here, a visual presentation of the tested contamination levels is presented in Figure II-4, showing the contaminations of the representative processes and procedures. Generally, the more vigorous milling (better efficiency) the process, the higher impurity concentrations are (SB-30m vs. SBL-30m). The milling time and the use of solution and Licowax® were also crucial contributors to the impurity absorption (i.e. H, C, O). However, it was also found the wax seemingly prohibited the absorption of nitrogen. As discussed in Chapter 5, the wax coating on the powder somehow prevented the nitrogen contamination. Compared the sintered results of the BM-24h powder, carbon and hydrogen was burnt off while oxygen and nitrogen increased likely due to the vacuum condition. More detailed explanation can be found in Chapter 5.

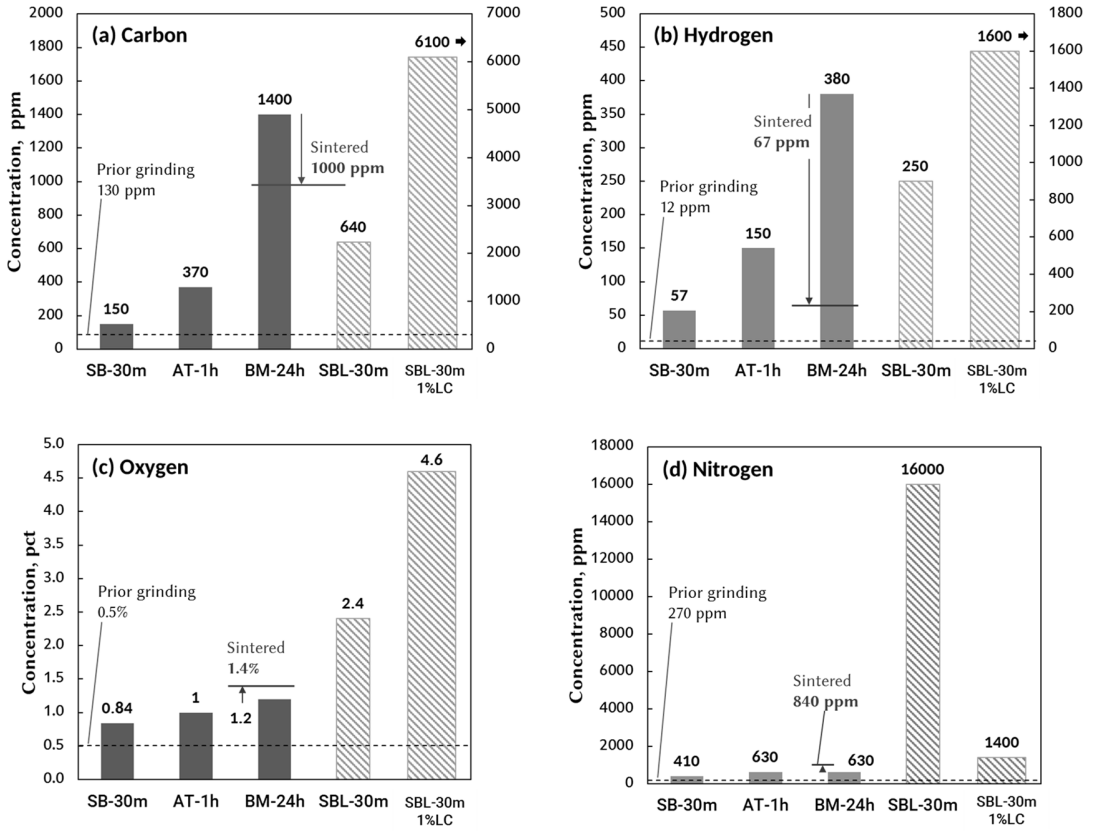

Figure II-4. Impurity levels of (a) carbon (b) hydrogen (c) oxygen and (d) nitrogen in various milled powders.

Appendix III. Copyright agreement letter

ELSEVIER LICENSE
TERMS AND CONDITIONS
Jul 05, 2016

This Agreement between Hung ("You") and Elsevier ("Elsevier") consists of your license details and the terms and conditions provided by Elsevier and Copyright Clearance Center.

License Number	3902550086724
License date	Jul 05, 2016
Licensed Content Publisher	Elsevier
Licensed Content Publication	Materials Science and Engineering: A
Licensed Content Title	A comparison of Ti–Ni and Ti-Sn binary alloys processed using powder metallurgy
Licensed Content Author	Hung-Wei Liu,D. Paul Bishop,Kevin P. Plucknett
Licensed Content Date	17 September 2015
Licensed Content Volume Number	644
Licensed Content Issue Number	n/a
Licensed Content Pages	13
Start Page	392
End Page	404
Type of Use	reuse in a thesis/dissertation
Portion	full article
Format	both print and electronic
Are you the author of this Elsevier article?	Yes
Will you be translating?	No
Order reference number	
Title of your thesis/dissertation	Powder Metallurgical Processing of Titanium Alloys and Aluminides
Expected completion date	Aug 2016
Estimated size (number of pages)	190
Elsevier VAT number	GB 494 6272 12
Requestor Location	Hung-Wei Liu 6172 Pepperell st.

	Halifax, NS B3H 2N9 Canada Attn: Hung-Wei Liu
Total	0.00 USD

INTRODUCTION

1. The publisher for this copyrighted material is Elsevier. By clicking "accept" in connection with completing this licensing transaction, you agree that the following terms and conditions apply to this transaction (along with the Billing and Payment terms and conditions established by Copyright Clearance Center, Inc. ("CCC"), at the time that you opened your Rightslink account and that are available at any time at http://myaccount.copyright.com).

GENERAL TERMS

2. Elsevier hereby grants you permission to reproduce the aforementioned material subject to the terms and conditions indicated.

3. Acknowledgement: If any part of the material to be used (for example, figures) has appeared in our publication with credit or acknowledgement to another source, permission must also be sought from that source. If such permission is not obtained then that material may not be included in your publication/copies. Suitable acknowledgement to the source must be made, either as a footnote or in a reference list at the end of your publication, as follows:

"Reprinted from Publication title, Vol /edition number, Author(s), Title of article / title of chapter, Pages No., Copyright (Year), with permission from Elsevier [OR APPLICABLE SOCIETY COPYRIGHT OWNER]." Also Lancet special credit - "Reprinted from The

Lancet, Vol. number, Author(s), Title of article, Pages No., Copyright (Year), with permission from Elsevier."

4. Reproduction of this material is confined to the purpose and/or media for which permission is hereby given.

5. Altering/Modifying Material: Not Permitted. However figures and illustrations may be altered/adapted minimally to serve your work. Any other abbreviations, additions, deletions and/or any other alterations shall be made only with prior written authorization of Elsevier Ltd. (Please contact Elsevier at permissions@elsevier.com)

6. If the permission fee for the requested use of our material is waived in this instance, please be advised that your future requests for Elsevier materials may attract a fee.

7. Reservation of Rights: Publisher reserves all rights not specifically granted in the combination of (i) the license details provided by you and accepted in the course of this licensing transaction, (ii) these terms and conditions and (iii) CCC's Billing and Payment terms and conditions.

8. License Contingent Upon Payment: While you may exercise the rights licensed immediately upon issuance of the license at the end of the licensing process for the transaction, provided that you have disclosed complete and accurate details of your proposed use, no license is finally effective unless and until full payment is received from you (either by publisher or by CCC) as provided in CCC's Billing and Payment terms and conditions. If full payment is not received on a timely basis, then any license preliminarily granted shall be deemed automatically revoked and shall be void as if never granted. Further, in the event that you breach any of these terms and conditions or any of CCC's Billing and Payment terms and conditions, the license is automatically revoked and shall be void as if never granted. Use of materials as described in a revoked license, as well as any use of the materials beyond the scope of an unrevoked license, may constitute copyright infringement and publisher reserves the right to take any and all action to protect its copyright in the materials.

9. Warranties: Publisher makes no representations or warranties with respect to the licensed material.

10. Indemnity: You hereby indemnify and agree to hold harmless publisher and CCC, and their respective officers, directors, employees and agents, from and against any and all claims arising out of your use of the licensed material other than as specifically authorized pursuant to this license.

11. No Transfer of License: This license is personal to you and may not be sublicensed, assigned, or transferred by you to any other person without publisher's written permission.

12. No Amendment Except in Writing: This license may not be amended except in a writing signed by both parties (or, in the case of publisher, by CCC on publisher's behalf).

13. Objection to Contrary Terms: Publisher hereby objects to any terms contained in any purchase order, acknowledgment, check endorsement or other writing prepared by you, which terms are inconsistent with these terms and conditions or CCC's Billing and Payment terms and conditions. These terms and conditions, together with CCC's Billing and Payment terms and conditions (which are incorporated herein), comprise the entire agreement between you and publisher (and CCC) concerning this licensing transaction. In the event of any conflict between your obligations established by these terms and conditions and those established by CCC's Billing and Payment terms and conditions, these terms and conditions shall control.

14. Revocation: Elsevier or Copyright Clearance Center may deny the permissions described in this License at their sole discretion, for any reason or no reason, with a full refund payable to you. Notice of such denial will be made using the contact information provided by you. Failure to receive such notice will not alter or invalidate the denial. In no event will Elsevier or Copyright Clearance Center be responsible or liable for any costs, expenses or damage incurred by you as a result of a denial of your permission request, other than a refund of the amount(s) paid by you to Elsevier and/or Copyright Clearance Center for denied permissions.

LIMITED LICENSE

The following terms and conditions apply only to specific license types:

15. **Translation**: This permission is granted for non-exclusive world English rights only unless your license was granted for translation rights. If you licensed translation rights you may only translate this content into the languages you requested. A professional translator must perform all translations and reproduce the content word for word preserving the integrity of the article.

16. **Posting licensed content on any Website**: The following terms and conditions apply as follows: Licensing material from an Elsevier journal: All content posted to the web site must maintain the copyright information line on the bottom of each image; A hyper-text must be included to the Homepage of the journal from which you are licensing at http://www.sciencedirect.com/science/journal/xxxxx or the Elsevier homepage for books at http://www.elsevier.com; Central Storage: This license does not include permission for a scanned version of the material to be stored in a central repository such as that provided by Heron/XanEdu.

Licensing material from an Elsevier book: A hyper-text link must be included to the Elsevier homepage at http://www.elsevier.com . All content posted to the web site must maintain the copyright information line on the bottom of each image.

Posting licensed content on Electronic reserve: In addition to the above the following clauses are applicable: The web site must be password-protected and made available only to bona fide students registered on a relevant course. This permission is granted for 1 year only. You may obtain a new license for future website posting.

17. **For journal authors:** the following clauses are applicable in addition to the above:

Preprints:

A preprint is an author's own write-up of research results and analysis, it has not been peer-reviewed, nor has it had any other value added to it by a publisher (such as formatting, copyright, technical enhancement etc.).

Authors can share their preprints anywhere at any time. Preprints should not be added to or enhanced in any way in order to appear more like, or to substitute for, the final versions of articles however authors can update their preprints on arXiv or RePEc with their Accepted Author Manuscript (see below).

If accepted for publication, we encourage authors to link from the preprint to their formal publication via its DOI. Millions of researchers have access to the formal publications on ScienceDirect, and so links will help users to find, access, cite and use the best available version. Please note that Cell Press, The Lancet and some society-owned have different preprint policies. Information on these policies is available on the journal homepage.

Accepted Author Manuscripts: An accepted author manuscript is the manuscript of an article that has been accepted for publication and which typically includes author-incorporated changes suggested during submission, peer review and editor-author communications.

Authors can share their accepted author manuscript:

- – immediately
    - via their non-commercial person homepage or blog
    - by updating a preprint in arXiv or RePEc with the accepted manuscript
    - via their research institute or institutional repository for internal institutional uses or as part of an invitation-only research collaboration work-group
    - directly by providing copies to their students or to research collaborators for their personal use
    - for private scholarly sharing as part of an invitation-only work group on commercial sites with which Elsevier has an agreement
- – after the embargo period
    - via non-commercial hosting platforms such as their institutional repository
    - via commercial sites with which Elsevier has an agreement

In all cases accepted manuscripts should:

- – link to the formal publication via its DOI
- – bear a CC-BY-NC-ND license - this is easy to do
- – if aggregated with other manuscripts, for example in a repository or other site, be shared in alignment with our hosting policy not be added to or enhanced in any way to appear more like, or to substitute for, the published journal article.

Published journal article (JPA): A published journal article (PJA) is the definitive final record of published research that appears or will appear in the journal and embodies all value-adding publishing activities including peer review co-ordination, copy-editing, formatting, (if relevant) pagination and online enrichment.

Policies for sharing publishing journal articles differ for subscription and gold open access articles:

Subscription Articles: If you are an author, please share a link to your article rather than the full-text. Millions of researchers have access to the formal publications on ScienceDirect, and so links will help your users to find, access, cite, and use the best available version.

Theses and dissertations which contain embedded PJAs as part of the formal submission can be posted publicly by the awarding institution with DOI links back to the formal publications on ScienceDirect.

If you are affiliated with a library that subscribes to ScienceDirect you have additional private sharing rights for others' research accessed under that agreement. This includes use for classroom teaching and internal training at the institution (including use in course packs and courseware programs), and inclusion of the article for grant funding purposes.

Gold Open Access Articles: May be shared according to the author-selected end-user license and should contain a CrossMark logo, the end user license, and a DOI link to the formal publication on ScienceDirect.

Please refer to Elsevier's posting policy for further information.

18. **For book authors** the following clauses are applicable in addition to the above: Authors are permitted to place a brief summary of their work online only. You are not allowed to download and post the published electronic version of your chapter, nor may

you scan the printed edition to create an electronic version. Posting to a repository: Authors are permitted to post a summary of their chapter only in their institution's repository.

19. **Thesis/Dissertation:** If your license is for use in a thesis/dissertation your thesis may be submitted to your institution in either print or electronic form. Should your thesis be published commercially, please reapply for permission. These requirements include permission for the Library and Archives of Canada to supply single copies, on demand, of the complete thesis and include permission for Proquest/UMI to supply single copies, on demand, of the complete thesis. Should your thesis be published commercially, please reapply for permission. Theses and dissertations which contain embedded PJAs as part of the formal submission can be posted publicly by the awarding institution with DOI links back to the formal publications on ScienceDirect.

Elsevier Open Access Terms and Conditions

You can publish open access with Elsevier in hundreds of open access journals or in nearly 2000 established subscription journals that support open access publishing. Permitted third party re-use of these open access articles is defined by the author's choice of Creative Commons user license. See our open access license policy for more information.

Terms & Conditions applicable to all Open Access articles published with Elsevier:

Any reuse of the article must not represent the author as endorsing the adaptation of the article nor should the article be modified in such a way as to damage the author's honour or reputation. If any changes have been made, such changes must be clearly indicated.

The author(s) must be appropriately credited and we ask that you include the end user license and a DOI link to the formal publication on ScienceDirect.

Commercial reuse includes:

- Associating advertising with the full text of the Article
- Charging fees for document delivery or access
- Article aggregation
- Systematic distribution via e-mail lists or share buttons

Posting or linking by commercial companies for use by customers of those companies.

20. **Other Conditions:**

v1.8

Questions? customercare@copyright.com or +1-855-239-3415 (toll free in the US) or +1-978-646-2777.

Reference

[1] F. Cardarelli, Materials Handbook — a concise desktop reference, Mater. Des. 22 (2001) 237. doi:10.1016/S0261-3069(00)00075-3.

[2] C. Leyens, M. Peters, Titanium and titanium alloys: fundamentals and applications, Wiley-VCH, 2003.

[3] A.K. Sachdev, K. Kulkarni, Z.Z. Fang, R. Yang, V. Girshov, Titanium for automotive applications: Challenges and opportunities in materials and processing, Jom. 64 (2012) 553–565. doi:10.1007/s11837-012-0310-8.

[4] B. Hurless, F.H. Fores, Lowering the cost of titanium, AMPTIAC. 6 (2002) 3–9.

[5] G. Lütjering, J.C. Williams, Titanium, Springer, 2007.

[6] I. Polmear, D. St. John, Light Alloys: From Traditional Alloys to Nanocrystals, Butterworth-Heinemann, 2005.

[7] M.J. Donachie, Titanium: A Technical Guide, 2000. doi:10.1361/tatg2000p00.

[8] R. Kainuma, M. Palm, G. Inden, Solid-phase equilibria in the Ti-rich part of the Ti-Al system, Intermetallics. 2 (1994) 321–332. doi:10.1016/0966-9795(94)90018-3.

[9] M. Peters, Titanium and Titanium Alloys, 2003. doi:10.1002/3527602119.

[10] C. Leyens, M. Peters, Titanium and Titanium Alloys, Wiley, 2006.

[11] P. Bartolotta, D. Krause, Titanium aluminide applications in the high speed civil transport, Symp. Gamma Titan. Alum. (1999).

[12] Euprean Space Agency, IMPRESS Project Publishable Executive Summary, (2004) 1–9.

[13] M. Blum, G. Jarczyk, H. Scholz, S. Pleier, P. Busse, H. Laudenberg, K. Segtrop, R. Simon, Prototype plant for the economical mass production of TiAl-valves, Mater. Sci. Eng. A. 329–331 (2002) 616–620. doi:10.1016/S0921-5093(01)01513-1.

[14] E.A. Loria, Gamma titanium aluminides as prospective structural materials, Intermetallics. 8 (2000) 1339–1345. doi:10.1016/S0966-9795(00)00073-X.

[15] T. Tetsui, Gamma Ti aluminides for non-aerospace applications, Curr. Opin. Solid State Mater. Sci. 4 (1999) 243–248. doi:10.1016/S1359-0286(99)00023-6.

[16] T. Noda, Application of cast gamma TiAl for automobiles, Intermetallics. 6 (1998)

709–713. doi:10.1016/S0966-9795(98)00060-0.

[17] T. Tetsui, Development of a TiAl turbocharger for passenger vehicles, Mater. Sci. Eng. A. 329–331 (2002) 582–588. doi:10.1016/S0921-5093(01)01584-2.

[18] H. Huang, P. Virtanen, T. Tiainen, Y. Ji, Synthesis of-TiAl Based Alloy by Mechanical Alloying and Reactive Hot Isostatic Pressing, J. Mater. Eng. Perform. 7 (1998) 784–788. doi:10.1361/105994998770347369.

[19] G.A. Salishchev, O.N. Senkov, A. Processes, R.M. Imayev, V.M. Imayev, M.R. Shagiev, A. V Kuznetsov, F. Appel, M. Oehring, O.A. Kaibyshev, Processing and Deformation Behavior of Gamma TiAl Alloys with Fine-Grained Equiaxed Microstructures, Adv. Perform. Mater. 116 (2000) 107–116.

[20] M.T.T. Jovanović, B. Dimčić, I. Bobić, S. Zec, V. Maksimović, Microstructure and mechanical properties of precision cast TiAl turbocharger wheel, J. Mater. Process. Technol. 167 (2005) 14–21. doi:10.1016/j.jmatprotec.2005.03.019.

[21] S. Abkowitz, Cost savings in the application of PM titanium and PM aluminum alloys, Prog. Powder Metall. 3 (1974) 85–101.

[22] R.M. German, Sintering: from Empirical Observations to Scientific Principles, 2014. doi:10.1016/B978-0-12-401682-8.00010-0.

[23] R.M. German, Powder Metallurgy & Particulate Materials Processing, (2005). https://www.amazon.ca/Powder-Metallurgy-Particulate-Materials-Processing/dp/0976205718 (accessed June 6, 2016).

[24] P.W. Voorhees, M.E. Glicksman, Ostwald ripening during liquid phase sintering--- Effect of volume fraction on coarsening kinetics, Metall. Trans. A. 15 (1984) 1081–1088. doi:10.1007/BF02644701.

[25] D.J. MILLER, J.A. PASK, Liquid-Phase Sintering of TiC-Ni Composites, J. Am. Ceram. Soc. 66 (1983) 841–846. doi:10.1111/j.1151-2916.1983.tb10998.x.

[26] A.P. Savitskii, M.A. Emel'yanova, N.N. Burtsev, Volume changes experienced by Cu-Sn compacts during liquid-phase sintering, Sov. Powder Metall. Met. Ceram. 22 (1983) 989–992. doi:10.1007/BF00802426.

[27] R.M. German, J.W. Dunlap, Processing of Iron-Titanium Powder Mixtures by Transient Liquid Phase Sintering, 17 (1986) 205–213.

[28] I. Robertson, G. Schaffer, Swelling during liquid phase sintering of Ti–Ni alloys, Powder Metall. (2009).

[29] G. Weintraub, H. Rush, Process and apparatus for sintering refractory material, (1913).

[30] G.F. Taylor, Apparatus for making hard metal compositions, 1933.

[31] M. Tokita, Recent and future progress on advanced ceramics sintering by Spark Plasma Sintering, Nanotechnologies Russ. 10 (2015) 261–267. doi:10.1134/S1995078015020202.

[32] L. Gao, J.. Hong, H. Miyamoto, S.D.D.. Torre, Bending strength and microstructure of Al2O3 ceramics densified by spark plasma sintering, J. Eur. Ceram. Soc. 20 (2000) 2149–2152. doi:10.1016/S0955-2219(00)00086-8.

[33] G. Maizza, S. Grasso, Y. Sakka, T. Noda, O. Ohashi, Relation between microstructure, properties and spark plasma sintering (SPS) parameters of pure ultrafine WC powder, Sci. Technol. Adv. Mater. 8 (2016) 644–654. doi:10.1016/j.stam.2007.09.002.

[34] A. Zavaliangos, J. Zhang, M. Krammer, J.R. Groza, Temperature evolution during field activated sintering, Mater. Sci. Eng. A. 379 (2004) 218–228. doi:10.1016/j.msea.2004.01.052.

[35] S. Hayun, V. Paris, R. Mitrani, S. Kalabukhov, M.P. Dariel, E. Zaretsky, N. Frage, Microstructure and mechanical properties of silicon carbide processed by Spark Plasma Sintering (SPS), Ceram. Int. 38 (2012) 6335–6340. doi:10.1016/j.ceramint.2012.05.003.

[36] M. Tokia, Trends in advanced SPS spark plasma sintering systems and technology. Functionally gradient materials and unique synthetic processing methods from next generation of powder technology., J. Soc. Powder Technol. Japan. 30 (1993) 790–804. doi:10.4164/sptj.30.11_790.

[37] M. Suárez, A. Fernández, J. Menéndez, Challenges and Opportunities for Spark Plasma Sintering: A Key Technology for a New Generation of Materials, Sinter. Appl. (2013) 319. doi:http://dx.doi.org/10.5772/53706.

[38] O. Guillon, J. Gonzalez-Julian, B. Dargatz, T. Kessel, G. Schierning, J. R??thel, M. Herrmann, Field-assisted sintering technology/spark plasma sintering: Mechanisms, materials, and technology developments, Adv. Eng. Mater. 16 (2014) 830–849. doi:10.1002/adem.201300409.

[39] M. Nygren, Z. Shen, On the preparation of bio-, nano- and structural ceramics and composites by spark plasma sintering, Solid State Sci. 5 (2003) 125–131. doi:10.1016/S1293-2558(02)00086-9.

[40] T. Mizuguchi, S. Guo, Y. Kagawa, Transmission electron microscopy characterization of spark plasma sintered ZrB2 ceramic, Ceram. Int. 36 (2010) 943–946. doi:10.1016/j.ceramint.2009.10.025.

[41] D.M. Hulbert, A. Anders, J. Andersson, E.J. Lavernia, A.K. Mukherjee, A discussion on the absence of plasma in spark plasma sintering, Scr. Mater. 60

(2009) 835–838. doi:10.1016/j.scriptamat.2008.12.059.

[42] R. Collet, S. le Gallet, F. Charlot, S. Lay, J.M. Chaix, F. Bernard, Oxide reduction effects in SPS processing of Cu atomized powder containing oxide inclusions, Mater. Chem. Phys. 173 (2016) 498–507. doi:10.1016/j.matchemphys.2016.02.044.

[43] Z.A. Munir, U. Anselmi-Tamburini, M. Ohyanagi, The effect of electric field and pressure on the synthesis and consolidation of materials: A review of the spark plasma sintering method, J. Mater. Sci. 41 (2006) 763–777. doi:10.1007/s10853-006-6555-2.

[44] J.E. Garay, Current-Activated, Pressure-Assisted Densification of Materials, Annu. Rev. Mater. Res. 40 (2010) 445–468. doi:10.1146/annurev-matsci-070909-104433.

[45] E.A. Olevsky, S. Kandukuri, L. Froyen, Consolidation enhancement in spark-plasma sintering: Impact of high heating rates, J. Appl. Phys. 102 (2007) 114913. doi:10.1063/1.2822189.

[46] Y. Zhou, K. Hirao, Y. Yamauchi, S. Kanzaki, Densification and grain growth in pulse electric current sintering of alumina, J. Eur. Ceram. Soc. 24 (2004) 3465–3470. doi:10.1016/j.jeurceramsoc.2003.10.013.

[47] E.A. Olevsky, L. Froyen, Impact of Thermal Diffusion on Densification During SPS, J. Am. Ceram. Soc. 92 (2009) S122–S132. doi:10.1111/j.1551-2916.2008.02705.x.

[48] G. Xie, O. Ohashi, T. Yoshioka, M. Song, K. Mitsuishi, H. Yasuda, K. Furuya, T. Noda, Effect of Interface Behavior between Particles on Properties of Pure Al Powder Compacts by Spark Plasma Sintering., Mater. Trans. 42 (2001) 1846–1849. doi:10.2320/matertrans.42.1846.

[49] H. Mehrer, Diffusion in Solids, Springer Berlin Heidelberg, Berlin, Heidelberg, 2007. doi:10.1007/978-3-540-71488-0.

[50] P. Asoka-Kumar, M. Alatalo, V. Ghosh, A. Kruseman, B. Nielsen, K. Lynn, Increased Elemental Specificity of Positron Annihilation Spectra., Phys. Rev. Lett. 77 (1996) 2097–2100. doi:10.1103/PhysRevLett.77.2097.

[51] J.E. Garay, S.C. Glade, U. Anselmi-Tamburini, P. Asoka-Kumar, Z.A. Munir, Electric current enhanced defect mobility in Ni3Ti intermetallics, Appl. Phys. Lett. 85 (2004).

[52] J.R. Pickens, Low-cost titanium for ships and tanks, Adv. Mater. Process. 162 (2004) 37–39.

[53] Y. Kosaka, K. Faller, S.P. Fox, Newly developed titanium alloy sheets for the exhaust systems of motorcycles and automobiles, JOM. 56 (2004) 32–34.

doi:10.1007/s11837-004-0249-5.

[54] M. Powder, C. Ward-Close, A. Godfrey, S. Thompson, Titanium made the EDO way should see prices drop, Met. Powder Rep. 60 (2005) 20–25. doi:10.1016/S0026-0657(05)70451-3.

[55] S. Huo, B. Heath, Applications of powder metallurgy aluminums for automotive valve-trains, SAE Int. J. Mater. Manuf. 1 (2008) 511–515.

[56] T.E. Norgate, G. Wellwood, The potential applications for titanium metal powder and their life cycle impacts, JOM. 58 (2006) 58–63. doi:10.1007/s11837-006-0084-y.

[57] H.-W. Liu, D.P. Bishop, K.P. Plucknett, Effect of processing variables on production of powder metallurgical titanium, Can. Metall. Q. 52 (2013) 39–50. doi:10.1179/1879139512Y.0000000040.

[58] R. German, P. Suri, S. Park, Review: liquid phase sintering, J. Mater. Sci. 44 (2009) 1–39. doi:10.1007/s10853-008-3008-0.

[59] R.M. German, Sintering theory and practice, 1st ed., Wiley-Interscience Publication, New York, 1996.

[60] H. Kadiri, L. Wang, H. Ozkan Gulsoy, P. Suri, S.J. Park, Y. Hammi, R.M. German, Development of a Ti-based alloy: design and experiment, Jom. 61 (2009) 60–66. doi:10.1007/s11837-009-0073-z.

[61] I.M. Robertson, G.B. Schaffer, Design of titanium alloy for efficient sintering to low porosity, Powder Metall. 52 (2009) 311–315. doi:10.1179/003258909X12502872942499.

[62] H. Baker, H. Okamoto, ASM handbook, volume 3 - Alloy Phase Diagrams, ASM International, 2004.

[63] B.B. Panigrahi, Sintering behaviour of Ti–2Ni and Ti–5Ni elemental powders, Mater. Lett. 61 (2007) 152–155. doi:10.1016/j.matlet.2006.04.025.

[64] R. Smart, E. Ellwood, The powder metallurgy of titanium-tin alloys containing up to 15% tin, Powder Metall. 4 (1959) 108–119.

[65] H.C. Hsu, S.C. Wu, Y.S. Hong, W.F. Ho, Mechanical properties and deformation behavior of as-cast Ti-Sn alloys, J. Alloys Compd. 479 (2009) 390–394. doi:10.1016/j.jallcom.2008.12.064.

[66] Y.L. Hao, S.J. Li, S.Y. Sun, R. Yang, Effect of Zr and Sn on Young's modulus and superelasticity of Ti-Nb-based alloys, Mater. Sci. Eng. A. 441 (2006) 112–118. doi:10.1016/j.msea.2006.09.051.

[67] E. Takahashi, T. Sakurai, S. Watanabe, N. Masahashi, S. Hanada, Effect of Heat Treatment and Sn Content on Superelasticity in Biocompatible TiNbSn Alloys., Mater. Trans. 43 (2002) 2978–2983. doi:10.2320/matertrans.43.2978.

[68] L.C. Tsao, Effect of Sn addition on the corrosion behavior of Ti – 7Cu – Sn cast alloys for biomedical applications, Mater. Sci. Eng. C. 46 (2015) 246–252. doi:10.1016/j.msec.2014.10.037.

[69] H.J. Rack, J.I. Qazi, Titanium alloys for biomedical applications, Mater. Sci. Eng. C. 26 (2006) 1269–1277. doi:10.1016/j.msec.2005.08.032.

[70] M. Whitney, S.F. Corbin, R.B. Gorbet, Investigation of the mechanisms of reactive sintering and combustion synthesis of NiTi using differential scanning calorimetry and microstructural analysis, Acta Mater. 56 (2008) 559–570. doi:10.1016/j.actamat.2007.10.012.

[71] I.M. Robertson, G.B. Schaffer, On sintering of Ti–Ni (–TiB2) alloys to near full density, Powder Metall. 54 (2011) 412–419. doi:10.1179/003258910X12740974839422.

[72] R.J. Low, I.M. Robertson, G.B. Schaffer, Excessive porosity after liquid-phase sintering of elemental titanium powder blends, Scr. Mater. 56 (2007) 895–898. doi:10.1016/j.scriptamat.2007.01.040.

[73] I.M. Robertson, G.B. Schaffer, Suitability of nickel as alloying element in titanium sintered in solid state, Powder Metall. 52 (2009) 225–232. doi:10.1179/003258908X336391.

[74] M. Whitney, S.F. Corbin, R.B. Gorbet, Investigation of the influence of Ni powder size on microstructural evolution and the thermal explosion combustion synthesis of NiTi, Intermetallics. 17 (2009) 894–906. doi:10.1016/j.intermet.2009.03.018.

[75] S.F. Corbin, D. Cluff, Determining the rate of (β-Ti) decay and its influence on the sintering behavior of NiTi, J. Alloys Compd. 487 (2009) 179–186. doi:10.1016/j.jallcom.2009.08.044.

[76] R. Nagarajan, K. Chattopadhyay, Intermetallic Ti2Ni/TiNi nanocomposite by rapid solidification, Acta Metall. Mater. 42 (1994) 947–958. doi:10.1016/0956-7151(94)90289-5.

[77] M.L. Wasz, F.R. Brotzen, R.B. McLellan, A.J. Griffin Jr, Effect of oxygen and hydrogen on mechanical properties of commercial purity titanium, Int. Mater. Rev. 41 (1996) 1–12.

[78] C.L. Briant, Z.F. Wang, N. Chollocoop, Hydrogen embrittlement of commercial purity titanium, Corros. Sci. 44 (2002) 1875–1888. doi:10.1016/S0010-938X(01)00159-7.

[79] T. Tetsui, Development of a TiAl turbocharger for passenger vehicles, Mater. Sci. Eng. A. 329–331 (2002) 582–588. doi:10.1016/S0921-5093(01)01584-2.

[80] L. Xu, Y.Y. Cui, Y.L. Hao, R. Yang, Growth of intermetallic layer in multi-laminated Ti/Al diffusion couples, Mater. Sci. Eng. A. 435–436 (2006) 638–647. doi:10.1016/j.msea.2006.07.077.

[81] J.B. Yang, W.S. Hwang, The preparation of TiAl-based intermetallics from elemental powders through a two-step pressureless sintering process, J. Mater. Eng. Perform. 7 (1998) 385–392.

[82] J.B. Yang, K.W. Teoh, W.S. Hwang, Preparation of (γ + α2) type TiAI intermetallics from elemental powders by solid state hot pressing, Mater. Sci. Technol. (1997). doi:10.1179/026708397790285908.

[83] J.B. Yang, K.W. Teoh, W.S. Hwang, Solid-State Hot Pressing of Elemental Aluminum and Titanium Powders to Form TiAI + (alpha2) Intermetallic Microstructure, J. Mater. Eng. Perform. 5 (1996) 583–588.

[84] Y. Mishin, C. Herzig, Diffusion in the Ti-Al system, Acta Mater. 48 (2000) 589–623.

[85] A. Bohm, B. Kieback, Investigation of swelling behaviour of Ti-Al elemental powder mixtures during reaction sintering, Z. Met. 89 (1998) 90–95.

[86] J. Luo, V. Acoff, Interfacial reactions of titanium and aluminum during diffusion welding, Weld. JOURNAL-NEW YORK-. (2000) 239–243.

[87] F.J.. van Loo, G.. Rieck, Diffusion in the titanium-aluminium system—I. Interdiffusion between solid Al and Ti or Ti-Al alloys, Acta Metall. 21 (1973) 61–71. doi:10.1016/0001-6160(73)90220-4.

[88] K.N. Kulkarni, Y. Sun, A.K. Sachdev, E. Lavernia, Field-activated sintering of blended elemental γ-TiAl powder compacts: Porosity analysis and growth kinetics of Al3Ti, Scr. Mater. 68 (2013) 841–844. doi:10.1016/j.scriptamat.2013.02.004.

[89] B.D. Cullity, S.R. Stock, Elements of X-ray Diffraction, in: Prentice Hall, 2001: p. 348.

[90] J.L. Murray, Al-Ti phase diagram, in: ASM Handbook, Vol. 3 - Alloy Phase Diagrams, 2004: p. 327.

[91] T. Takasugi, Titanium aluminide-based ntermetallic alloys, Automot. Eng. Light. Funct. Nov. Mater. (2008) 197.

[92] P. Bartolotta, J. Barrett, T. Kelly, R. Smashey, The use of cast Ti–48Al–2Cr–2Nb in jet engines, Jom. 49 (1997) 48–50. doi:10.1007/BF02914685.

[93] K.S. Kumar, J.A.S. Green, J.D.E. Larsen, L.D. Kramer, XD^{TM} Titanium aluminide composites, Adv. Eng. Mater. 147 (1995) 35–38.

[94] A. Duarte, F. Viana, H.M.C.M. Santos, As-cast titanium aluminides microstructure modification, Mater. Res. 2 (1999) 191–195. doi:10.1590/S1516-14391999000300013.

[95] E.K.Y. Fu, R.D. Rawlings, H.B. McShane, Reaction synthesis of titanium aluminides, J. Mater. Sci. 36 (2001) 5537–5542.

[96] L.M. Hsiung, T.G. Nieh, Microstructures and properties of powder metallurgy TiAl alloys, Mater. Sci. Eng. A. 364 (2004) 1–10. doi:10.1016/S0921-5093(02)00639-1.

[97] J.C. Rawers, W.R. Wrzesinski, Reaction-sintered hot-pressed TiAl, J. Mater. Sci. 27 (1992) 2877–2886.

[98] M. Mirjalili, M. Soltanieh, K. Matsuura, M. Ohno, On the kinetics of TiAl 3 intermetallic layer formation in the titanium and aluminum diffusion couple, Intermetallics. 32 (2013) 297–302. doi:10.1016/j.intermet.2012.08.017.

[99] L. Xu, Y.Y.Y. Cui, Y.L.L. Hao, R. Yang, Growth of intermetallic layer in multi-laminated Ti/Al diffusion couples, Mater. Sci. Eng. A. 435–436 (2006) 638–647. doi:10.1016/j.msea.2006.07.077.

[100] J.B. Yang, K.W. Teoh, W.S. Hwang, Solid-state hot pressing of elemental aluminum and titanium powders to form TiAl ($\gamma + \alpha 2$) intermetallic microstructure, J. Mater. Eng. Perform. 5 (1996) 583–588. doi:10.1007/BF02646085.

[101] C. Suryanarayana, Mechanical alloying and milling, Prog. Mater. Sci. 46 (2001) 1–184. doi:10.1016/S0079-6425(99)00010-9.

[102] S. Djanarthany, J. Viala, J. Bouix, An overview of monolithic titanium aluminides based on Ti3Al and TiAl, 72 (2001) 301–319.

[103] J.F. Sun, M.Z. Wang, Y.C. Zhao, X.P. Li, B.Y. Liang, Synthesis of titanium nitride powders by reactive ball milling of titanium and urea, J. Alloys Compd. 482 (2009) 29–31. doi:10.1016/j.jallcom.2009.04.043.

[104] U.R. Kattner, J.C. Lin, Y.A. Chang, Thermodynamic assessment and calculation of the Ti-Al system, Metall. Trans. A. 23 (1992) 2081–2090. doi:10.1007/BF02646001.

[105] A. Raman, K. Schubert, On the constitution of some alloy series related to TiAl3. II. Investigations in some Ti-Al-Si-and Ti-4-6 in systems, Z. Met. Vol: 56 (1965).

[106] E.A. Holm, S.M. Foiles, How Grain Growth Stops: A Mechanism for Grain-

Growth Stagnation in Pure Materials, Science (80-.). 328 (2010) 1138–1141. doi:10.1126/science.1187833.

[107] M.A. Lagos, I. Agote, SPS synthesis and consolidation of TiAl alloys from elemental powders: Microstructure evolution, Intermetallics. 36 (2013) 51–56. doi:10.1016/j.intermet.2013.01.006.

[108] Y.H. Wang, J.P. Lin, Y.H. He, Y.L. Wang, Z. Lin, G.L. Chen, Reaction mechanism in high Nb containing TiAl alloy by elemental powder metallurgy, Trans. Nonferrous Met. Soc. China (English Ed. 16 (2006) 853–857. doi:10.1016/S1003-6326(06)60339-7.

[109] M. Schloffer, F. Iqbal, H. Gabrisch, E. Schwaighofer, F.-P. Schimansky, S. Mayer, A. Stark, T. Lippmann, M. Göken, F. Pyczak, H. Clemens, Microstructure development and hardness of a powder metallurgical multi phase γ-TiAl based alloy, Intermetallics. 22 (2012) 231–240. doi:10.1016/j.intermet.2011.11.015.

[110] T. Lee, J. Kim, S. Hwang, Direct consolidation of γ-TiAl-Mn-Mo from elemental powder mixtures and control of porosity through a basic study of powder reactions, Metall. Mater. Trans. A. (1997).

[111] Y.H. Wang, J.P. Lin, Y.H. He, Y.L. Wang, G.L. Chen, Microstructural characteristics of Ti-45Al-8.5Nb/TiB2 composites by powder metallurgy, J. Alloys Compd. 468 (2009) 505–511. doi:10.1016/j.jallcom.2008.01.057.

[112] K. Liu, Y.C. Ma, M. Gao, G.B. Rao, Y.Y. Li, K. Wei, X. Wu, M.H. Loretto, Single step centrifugal casting TiAl automotive valves, Intermetallics. 13 (2005) 925–928. doi:10.1016/j.intermet.2004.12.004.

[113] D. Chandley, P. Metal, C. Technology, Use of gamma titanium aluminide for automotive engine valves, Metall. Sci. Technol. Teksid. (2000) 8–11.

[114] D. Daloz, U. Hecht, J. Zollinger, H. Combeau, A. Hazotte, M. Založnik, Microsegregation, macrosegregation and related phase transformations in TiAl alloys, Intermetallics. 19 (2011) 749–756. doi:10.1016/j.intermet.2010.11.013.

[115] S. Xiao, J. Tian, L. Xu, Y. Chen, H. Yu, J. Han, Microstructures and mechanical properties of TiAl alloy prepared by spark plasma sintering, Trans. Nonferrous Met. Soc. China. 19 (2009) 1423–1427. doi:10.1016/S1003-6326(09)60044-3.

[116] A. Couret, G. Molénat, J. Galy, M. Thomas, Microstructures and mechanical properties of TiAl alloys consolidated by spark plasma sintering, Intermetallics. 16 (2008) 1134–1141. doi:10.1016/j.intermet.2008.06.015.

[117] J. Guyon, a. Hazotte, J.P. Monchoux, E. Bouzy, Effect of powder state on spark plasma sintering of TiAl alloys, Intermetallics. 34 (2013) 94–100. doi:10.1016/j.intermet.2012.11.005.

[118] H. Jabbar, J.-P. Monchoux, M. Thomas, a. Couret, Microstructures and deformation mechanisms of a G4 TiAl alloy produced by spark plasma sintering, Acta Mater. 59 (2011) 7574–7585. doi:10.1016/j.actamat.2011.09.001.

[119] N. Saheb, Z. Iqbal, A. Khalil, A.S. Hakeem, N. Al Aqeeli, T. Laoui, A. Al-Qutub, R. Kirchner, Spark plasma sintering of metals and metal matrix nanocomposites: A review, J. Nanomater. 2012 (2012). doi:10.1155/2012/983470.

[120] H.A. Calderon, V. Garibay-febles, M. Umemoto, M. Yamaguchi, Mechanical properties of nanocrystalline Ti – Al – X alloys, Mater. Sci. Eng. A. 331 (2002) 196–205.

[121] Y. Liu, B.Y. Huang, Y.H. He, K.C. Zhou, Processing TiAl-based alloy by elemental powder metallurgy, J. Mater. Sci. Technol. 16 (2000) 605–610.

[122] Z.M. Sun, Q. Wang, H. Hashimoto, S. Tada, T. Abe, Synthesis and consolidation of TiAl by MA-PDS process from sponge-Ti and chip-Al, Intermetallics. 11 (2003) 63–69. doi:10.1016/S0966-9795(02)00183-8.

[123] Y.Y. Chen, H.B. Yu, D.L. Zhang, L.H. Chai, Effect of spark plasma sintering temperature on microstructure and mechanical properties of an ultrafine grained TiAl intermetallic alloy, Mater. Sci. Eng. A. 525 (2009) 166–173. doi:10.1016/j.msea.2009.06.056.

[124] N.S. Weston, F. Derguti, A. Tudball, M. Jackson, Spark plasma sintering of commercial and development titanium alloy powders, J. Mater. Sci. 50 (2015) 4860–4878. doi:10.1007/s10853-015-9029-6.

[125] C.E. Wen, K. Yasue, Y. Yamada, Fabrication of TiAl by blended elemental powder semisolid forming, J. Mater. Sci. 36 (2001) 1741–1745.

[126] Y.W.Y. Kim, Ordered intermetallic alloys, part III: Gamma titanium aluminides, Jom. 46 (1994) 30–39. doi:10.1007/BF03220745.

[127] D.A. Porter, K.E. Easterling, M. Sherif, Phase Transformations in Metals and Alloys, Third Edition (Revised Reprint), CRC Press, 2009.

[128] S.C. Tjong, Y.W. Mai, Processing-structure-property aspects of particulate- and whisker-reinforced titanium matrix composites, Compos. Sci. Technol. 68 (2008) 583–601. doi:10.1016/j.compscitech.2007.07.016.

[129] T. Saito, The Automotive Application of Discontinuously Reinforced TiB-Ti Composites, (1998) 33–36.

[130] C. Leyens, J. Hausmann, J. Kumpfert, Continuous Fiber Reinforced Titanium Matrix Composites: Fabrication, Properties, and Applications, Adv. Eng. Mater. 5 (2003) 399–410. doi:10.1002/adem.200310093.

[131] D.R. Ni, L. Geng, J. Zhang, Z.Z. Zheng, Effect of B4C particle size on microstructure of in situ titanium matrix composites prepared by reactive processing of Ti-B4C system, Scr. Mater. 55 (2006) 429–432. doi:10.1016/j.scriptamat.2006.05.024.

[132] D.R. Ni, L. Geng, J. Zhang, Z.Z. Zheng, Fabrication and tensile properties of in situ TiBw and TiCp hybrid-reinforced titanium matrix composites based on Ti–B4C–C, Mater. Sci. Eng. A. 478 (2008) 291–296. doi:10.1016/j.msea.2007.06.004.

[133] L. Geng, D.R. Ni, J. Zhang, Z.Z. Zheng, Hybrid effect of TiBw and TiCp on tensile properties of in situ titanium matrix composites, J. Alloys Compd. 463 (2008) 488–492. doi:10.1016/j.jallcom.2007.09.054.

[134] L. Jia, S.F. Li, H. Imai, B. Chen, K. Kondoh, Size effect of B4C powders on metallurgical reaction and resulting tensile properties of Ti matrix composites by in-situ reaction from Ti-B4C system under a relatively low temperature, Mater. Sci. Eng. A. 614 (2014) 129–135. doi:10.1016/j.msea.2014.07.020.

[135] W. Zhang, L. Gao, Y. Lei, B. Yang, J. Li, L. Xiao, Y. Yin, TiAl/B4C composite fabricated by high energy ball milling and hot press sintering processes and its mechanical properties, Mater. Sci. Eng. A. 527 (2010) 7436–7441. doi:10.1016/j.msea.2010.08.041.

[136] J. Berlin, Analysis of Boron with Energy Dispersive Spectrometry, Imaging Microsc. 13 (2011) 19–21.

[137] J.S. Luo, T. Voisin, J.P. Monchoux, a. Couret, Refinement of lamellar microstructures by boron incorporation in GE-TiAl alloys processed by Spark Plasma Sintering, Intermetallics. 36 (2013) 12–20. doi:10.1016/j.intermet.2012.12.006.

[138] T. Voisin, J.P. Monchoux, L. Durand, N. Karnatak, M. Thomas, A. Couret, An Innovative Way to Produce γ-TiAl Blades: Spark Plasma Sintering, Adv. Eng. Mater. 17 (2015) 1408–1413. doi:10.1002/adem.201500019.

[139] S. Gorsse, D.B. Miracle, Mechanical properties of Ti-6Al-4V/TiB composites with randomly oriented and aligned TiB reinforcements, Acta Mater. 51 (2003) 2427–2442. doi:10.1016/S1359-6454(02)00510-4.

[140] Standard Test Methods for Evaporation Rates of Volatile Liquids by Shell Thin-Film, ASTM Int. 87 (1996) 1–8. doi:10.1520/D3539-87R04.2.